Uncertainty Modeling for Nonlinear and Linear Heated Structures

by

Pengchao Song

A Dissertation Presented in Partial Fulfillment
of the Requirements for the Degree
Doctor of Philosophy

Approved April 2019 by the
Graduate Supervisory Committee:

Marc Mignolet, Chair
Spring Berman
Aditi Chattopadhyay
Hanqing Jiang
Yongming Liu
Benjamin Smarslok

ARIZONA STATE UNIVERSITY

May 2019

ABSTRACT

This investigation focuses on the development of uncertainty modeling methods applicable to both the structural and thermal models of heated structures as part of an effort to enable the design under uncertainty of hypersonic vehicles. The maximum entropy-based nonparametric stochastic modeling approach is used within the context of coupled structural-thermal Reduced Order Models (ROMs). Not only does this strategy allow for a computationally efficient generation of samples of the structural and thermal responses but the maximum entropy approach allows to introduce both aleatoric and some epistemic uncertainty into the system.

While the nonparametric approach has a long history of applications to structural models, the present investigation was the first one to consider it for the heat conduction problem. In this process, it was recognized that the nonparametric approach had to be modified to maintain the localization of the temperature near the heat source, which was successfully achieved.

The introduction of uncertainty in coupled structural-thermal ROMs of heated structures was addressed next. It was first recognized that the structural stiffness coefficients (linear, quadratic, and cubic) and the parameters quantifying the effects of the temperature distribution on the structural response can be regrouped into a matrix that is symmetric and positive definite. The nonparametric approach was then applied to this matrix allowing the assessment of the effects of uncertainty on the resulting temperature distributions and structural response.

The third part of this document focuses on introducing uncertainty using the Maximum Entropy Method at the level of finite element by randomizing elemental

matrices, for instance, elemental stiffness, mass and conductance matrices. This approach brings some epistemic uncertainty not present in the parametric approach (e.g., by randomizing the elasticity tensor) while retaining more local character than the operation in ROM level.

The last part of this document focuses on the development of "reduced ROMs" (RROMs) which are reduced order models with small bases constructed in a data-driven process from a "full" ROM with a much larger basis. The development of the RROM methodology is motivated by the desire to optimally reduce the computational cost especially in multi-physics situations where a lack of prior understanding/knowledge of the solution typically leads to the selection of ROM bases that are excessively broad to ensure the necessary accuracy in representing the response. It is additionally emphasized that the ROM reduction process can be carried out adaptively, i.e., differently over different ranges of loading conditions.

ACKNOWLEDGEMENTS

I would like to show my sincere gratitude to Dr. Marc Mignolet, this work could not have been done without his knowledge, guidance and encouragement. His diligence and optimism continually motivated me toward the completion of this dissertation.

I would also like to thank Dr. X.Q. Julian Wang and Dr. Raghavendra Murthy for all the technical support they gave to me. They have made the completion of this work much smoother. My thanks also go to Dr. Spring Berman, Dr. Aditi Chattopadhyay, Dr. Hanqing Jiang, Dr. Yongming Liu, and Dr. Benjamin Smarslok for serving on my committee.

The financial support of this work by the Air Force Multi University Research Initiative contract FA9550-15-1-0038 with Dr. Jean-Luc Cambier as Technical Monitor is gratefully acknowledged.

At last I would like to thank my family and everyone who supported me on the road.

TABLE OF CONTENTS

Page

CHAPTER Page

CHAPTER Page

LIST OF TABLES

Table Page

LIST OF FIGURES

Figure Page

Figure Page

Figure Page

Figure Page

Figure Page

Figure Page

Figure Page

1. INTRODUCTION

1.1. Motivation and Focus

The design of hypersonic vehicles has been a goal for the U.S. Air Force for decades but it still remains a dire challenge. The prediction of the behavior of hypersonic structures is a complex task because of the strong multi-physics interactions taking place between structural response, aerodynamic force and heating, and heat conduction and radiation. Under hypersonic conditions, the aerodynamic and thermal loading are severe and likely to result in large deformations and strong nonlinearities in structural response, whereas standard structural dynamic analyses and design procedures assume a linear behavior.

Moreover, uncertainties may be expected to be important to the structural response under such severe conditions. For example, strongly nonlinear events such as buckling and snap-through may be triggered by asymmetries in systems designed to be symmetric. The uncertainties considered here include those associated with vehicle-to-vehicle variability, i.e., aleatoric uncertainty, and those resulting from modeling assumptions/simplifications, i.e., epistemic uncertainty. While safety factors are traditionally used to address these uncertainties, they lead to structures that are too heavy and thus not able to fulfill the design requirements. The success of a design under uncertainty of hypersonic vehicles will require a specific modeling of the uncertainties and their propagation through the coupled structural-thermal-aerodynamic interactions to predict probability density functions, percentiles, standard deviations, etc. of the response quantities of interest. Such modeling and propagation is the main focus of this investigation.

There are two options in uncertainty modeling: parametric and non-parametric. In parametric methods, parameters of the model such as material properties (Young's modulus, thermal conductivity) are modeled as random variables or stochastic fields, typically at the finite element level. While easy at first glance, there are challenges associated with parametric uncertainty modeling. The first is the proper selection of the (typically joint) probability density functions of the random variables or stochastic fields used. Obtaining such information typically requires a very significant amount of data, which is typically not available, leaving the user to carry out a series of assumptions which may be difficult to assess. The approach, when carried out at a finite element level, can be quite expensive for Monte-Carlo simulations with a large number of realizations.

There is a vast body of work focusing on application of parametric methods; see (Schenk and Schuëller 2003) and (Schenk and Schuëller 2007) for examples in modeling parameter uncertainties in the post buckling of cylindrical shells and see (Sankar et al 1993) and (Sarrouy et al 2012) in the context of uncertainties in high speed rotors. When modeling random fields, the polynomial chaos representation – a parametric representation of the uncertainty – has often been used and is the basis for the stochastic finite element method, see (Ghanem and Spanos 1991).

An option to reduce the computational cost is to rely on reduced order models (ROMs) for the determination of the response/solution. Accordingly, one can introduce the uncertainty at the finite element level then create a ROM for each finite element realization, and then finally compute the response of the ROM. An even faster strategy would be to bypass the finite element level realizations and directly generate random realizations of the ROM, see (Soize 2017) for an accelerated introduction of uncertainty

quantification in computational engineering. This process is the essence of the maximum entropy nonparametric approach reviewed next.

1.2. Maximum Entropy Nonparametric Modeling

The maximum entropy-based nonparametric stochastic modeling approach initially proposed by Soize (2000), see (Soize 2012) for a recent comprehensive review, is an elegant approach to randomize ROMs directly. It proceeds directly from the mean model ROMs, assumed to be characterized by matrices, randomizing them so that they always satisfy physical requirements (positive definiteness, symmetry, etc.). This is clearly not sufficient information to define the joint probability density function of the elements of these matrices. To alleviate this situation, it will be assumed that this function achieves the maximum of the entropy given the physical requirements as constraints. Moreover, as discussed in (Soize 2000) and (Soize 2012), this approach not only permits the modeling of aleatoric but also some epistemic uncertainty.

In its original formulation, i.e., for a symmetric positive definite matrix $\boldsymbol{A}$ (such as the mass and linear stiffness matrices), the maximum entropy nonparametric approach proceeds as follows. First, the mean matrix $\overline{\boldsymbol{A}}$ is decomposed as

$$\overline{\boldsymbol{A}} = \overline{\boldsymbol{L}}\,\overline{\boldsymbol{L}}^T \tag{1.1}$$

e.g., by Cholesky factorization. Then, random matrices A are generated as

$$\boldsymbol{A} = \overline{\boldsymbol{L}}\,\boldsymbol{H}\,\boldsymbol{H}^T\,\overline{\boldsymbol{L}}^T \tag{1.2}$$

where $\boldsymbol{H}$ is a lower triangular matrix such that (see also Fig. 1.1)

(1) its off-diagonal elements H_{il}, $i \neq l$, are normally distributed (Gaussian) random variables with standard deviation $\sigma = 1/\sqrt{2\mu}$, and

(2) its diagonal elements H_{ii} are obtained as $H_{ii} = \sqrt{Y_{ii}/\mu}$ where Y_{ii} is Gamma distributed with parameter $(p(i)-1)/2$ where

$$p(i) = n - i + 2\lambda_0 - 1 \quad \text{and} \quad \mu = (n + 2\lambda_0 - 1)/2 \tag{1.3}$$

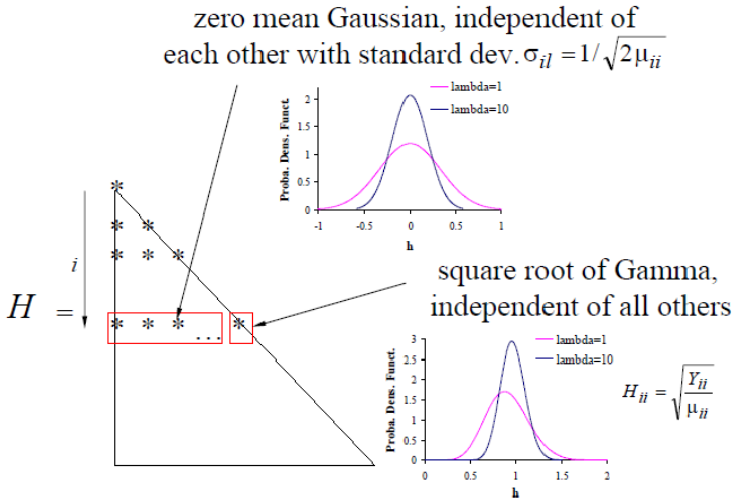

Figure 1.1. Structure of the Random H Matrices with n = 8, i =2, and λ_0 = 1 and 10.

In the above equations, *n* is the size of the matrices and the parameter $\lambda_0 > 0$ is the free parameter of the statistical distribution of the random matrices ***A***. An alternative parametrization is through the dispersion parameter δ defined as

$$\delta^2 = \frac{n+1}{n + 2\lambda_0 - 1} \tag{1.4}$$

1.3. Nonlinear Thermal-Structural Reduced Order Model

The non-intrusive construction of reduced order models to predict the nonlinear geometric response of structures has been well developed and demonstrated successful in many applications in at least the last 20 years. This approach represents the extension to the nonlinear geometric situation of the modal models used for the dynamic response of linear structures and also relies on expressing it as a combination of limited number of

basis functions. The difference with respect to the linear case is that the equations of motion for the generalized coordinates are no longer linear but rather involve cubic polynomials of the general coordinates.

A particular set of nonlinear ROM studies, initiated at least by (McEwan et al 2001), have focused on developing the entire reduced order model from commercial FEA software and, accordingly, proceed non-intrusively relying on standard inputs and outputs from such software. Since 2001, many developments have been made and successfully applied, see (Mignolet et al 2013) for a review. Further, see (Hollkamp et al 2005), (Mignolet et al 2003), (Kim et al 2013), (Przekop and Rizzi 2007), (Przekop and Rizzi on AIAAJ 2006), (Prezkop et al 2012), (Rizze and Przekop 2008), (Przekop and Rizzi on Int Conf Adv Struct Dyna 2006) and (Perez et al 2014) for the selection of the modal basis; and see (Muravyov and Rizzi 2003), (Kim et al 2009), (Perez et al 2014), (Wang et al 2019) and (Spottswood and Allemang 2007) for algorithms to identify the coefficients of the cubic polynomials appearing in the equations of motion. The current state of the art in this nonlinear ROM approach is well beyond simple beam and plates, see the following references (Y. Wang et al 2018), (Gogulapati et al 2017), (Gogulapati et al 2014), (Perez et al 2010), (Perez et al 2014), (X.Q. Wang et al 2018) and (Matney et al 2012) for the validation of the nonlinear ROM methodology to fairly complex structures.

The coupled structural-thermal ROMs employed here are based on the representation of the temperature and displacements of the finite element nodes, stacked in the time varying vectors $\boldsymbol{T}(t)$ and $\boldsymbol{u}(t)$, in expansion forms, i.e.

$$\boldsymbol{T}(t) = \sum_{n=1}^{\mu} \tau_n(t)\, \boldsymbol{T}^{(n)} \tag{1.5}$$

$$\boldsymbol{u}(t) = \sum_{n=1}^{M} q_n(t)\, \boldsymbol{\psi}^{(n)} \tag{1.6}$$

In these equations, $\boldsymbol{T}^{(n)}$ and $\boldsymbol{\psi}^{(n)}$ are the thermal and structural basis functions, or modes, while $\tau_n(t)$ and $q_n(t)$ are the time-dependent thermal and structural generalized coordinates.

Assuming that the material properties (elasticity tensor, coefficient of thermal expansion) do not vary with temperature, it is found, e.g. (Perez et al 2011), for the structural generalized coordinates that (summation over repeated indices assumed)

$$M_{ij}\ddot{q}_j + D_{ij}\dot{q}_j + \left[K_{ij}^{(1)} - K_{ijl}^{(th)}\,\tau_l\right] q_j + K_{ijl}^{(2)} q_j q_l + K_{ijlp}^{(3)} q_j q_l q_p = F_i + F_{il}^{(th)}\,\tau_l \tag{1.7}$$

In this equation, M_{ij} denotes the elements of the mass matrix, $K_{ij}^{(1)}$, $K_{ijl}^{(2)}$, $K_{ijlp}^{(3)}$ are linear, quadratic, and cubic stiffness coefficients and F_i are the modal mechanical forces. The parameters $K_{ijl}^{(th)}$ and $F_{il}^{(th)}$ represent the sole coupling terms with the temperature field which is described by the governing equations (Perez et al 2011, Matney et al 2011)

$$B_{ij}\,\dot{\tau}_j + \tilde{K}_{ij}\tau_j = P_i \tag{1.8}$$

where B_{ij} and $\tilde{K}_{ij}$ are the capacitance and conductance matrices of the finite element model, which are assumed here not to depend on temperature. The source term P_i represents the combined effects of an applied flux, nonzero homogenous boundary conditions, radiation, latency, etc. as applicable.

Having established the forms of the governing equations, i.e., Eqs (1.7) and (1.8), it remains to address (i) the selection of the basis functions $\boldsymbol{T}^{(n)}$ and $\boldsymbol{\psi}^{(n)}$ and (ii) the identification of all stiffness, mass, conductance, and capacitance parameters from commercial finite element software. The latter effort is detailed in (Perez et al 2011, Kim et al 2013, Mignolet et al 2013, Perez et al 2014) for temperature independent structural properties and has been extended in (Matney et al 2011) when they vary linearly with the local temperature. The former issue has also been addressed, in (Mignolet et al 2013) for the structural problem, see also (Kim et al 2013, Mignolet et al 2013, Perez et al 2014) for the linear + dual modes basis selected here. The construction of the thermal basis has been investigated in a series of papers (Perez et al 2011, Falkiewicz and Cesnik 2011, Matney et al 2014, Matney et al 2015, Murthy et al 2016) and can be achieved from a series of snapshots of the temperature distribution, e.g., (Falkiewicz and Cesnik 2011), a priori from the conductance and capacitance matrices (Perez et al 2011), or using a combination of a priori information and a few snapshots (Matney et al 2014, Matney et al 2015, Murthy et al 2016).

The above discussion demonstrates that coupled nonlinear structural-thermal reduced order models can be constructed from well characterized finite element models. Given this state of the art, it is then timely to consider the introduction of uncertainty in these models to bridge the gap between designed and realized structures and assess the effects of the differences between them.

1.4. Research Topics

The maximum entropy method has been applied to a broad range of structural problems, in these problems the response exhibits mostly global features. However, when

applied to a problem that exhibits local response, e.g., a class of heat conduction problems, this method tends to lead to a globalized response as will be shown in Chapter 2. This undesirable effect is an unexpected consequence of the epistemic uncertainty introduced by this method, the uncertain changes to the model's structure are more likely to promote a global response at the contrary of localizing it. Then, introduced in Chapter 2 is an extension to the maximum entropy method resolving this issue and maintaining the local behavior of the uncertain response if the mean model response is localized. This work was published in (Song and Mignolet, 2018).

In Chapter 3, uncertainty modeling in structural-thermal coupled system is addressed in the framework of reduced order model. Since the effects of uncertainty on structural properties have been well studied, the investigation is focused primarily on introducing uncertainty in the thermal properties (capacitance, conductance) and in thermal structural coupling effect (coefficient of thermal expansion).

The globalization of the uncertain response observed in Chapter 2 demonstrated for the first time a negative associated with introducing epistemic uncertainty modeling at the ROM level, i.e., at a global level. Besides proceeding with the new formulation of Chapter 2, one could imagine introducing the epistemic uncertainty at a lower level where its effects will remain more local. This perspective motivated the work of Chapter 4 in where the nonparametric methodology is applied at the finite element level by randomizing the elemental stiffness matrices of each element. This new strategy brings epistemic uncertainty not present in the parametric modeling while retaining more local character of this uncertainty than achieved with the ROM level nonparametric approach. While this approach is technically possible for nonlinear geometric problems, it is

demonstrated and studied here for linear structural problems without and then with heating effects.

The last focus of this dissertation is on the formulation and first assessment of a methodology to adapt/reduce the basis of ROMs. In complex multiphysics problems, the construction of a single "full" ROM for the entire mission/range of loadings is very likely to lead to large bases to ensure that the set of responses is well captured, especially since these responses are generally not well predictable a priori. The clear drawback of these large bases is a large computational cost undercutting the benefits of using ROMs. To address this situation, a methodology is developed in Chapter 5 to use short segment of response data generated from such large ROMs to construct smaller bases of "Reduced ROMs". Such RROMs would then have the desired computational advantage but may not be valid over the broad range of loading conditions desired thereby leading to the need to adapt the RROMs. The key questions of how large the RROM basis should be to optimize the RROM computational benefit and of the determination of the time/loading condition at which to adapt are addressed in Chapter 5. Moreover, a validation of this RROM strategy to a coupled structural-thermal-aerodynamic response of a representative hypersonic panel is successfully carried out.

2. REDUCED ORDER MODEL-BASED UNCERTAINTY MODELING OF STRUCTURES WITH LOCALIZED RESPONSE

2.1. Introduction

Since its initial formulation in (Soize 2000), the maximum entropy-based nonparametric approach has been extended multiple times to cover new classes of problems, e.g., vibro-acoustics (Durand et al 2008, Ohayon and Soize 2014), rotordynamics (Murthy et al 2010 Part I, Murthy et al 2010 Part II, Murthy et al 2014), nonlinear structural dynamics (Mignolet and Soize 2008, Capiez-Lernout et al 2014), nonlinear thermoelastic problems (Song et al 2017), linear viscoelastic structures (Soize 2012), etc., but also in rigid body dynamics (Batou and Soize 2012, Richter and Mignolet 2017) and micromechanics and multiscale modeling, see (Soize 2012). The focus of the present effort is on yet another extension of this approach, more specifically to problems in which the response of the uncertain structure is expected to be localized with the mean model response either localized as well (the first case considered below) or global (the second case). The present effort focuses on structural applications only but there are non-structural ones in which these conditions are encountered, e.g., in some heat conduction problems (Song et al 2017), and to which the present discussion may also apply.

2.2. Representative Examples

2.2.1. Class A Structures

To illustrate one class of structures investigated here, consider the annulus shown in Fig. 2.1(a) of inner radius 0.8m, outer radius 1m, thickness 0.002m clamped on its inner radius and free on the outer one. The material, aluminum, is assumed to be homogenous

and isotropic with Young's modulus E = 7.3 10^{10} Pa and Poisson's ratio ν= 0.316. The annulus is subjected to a static uniform unit pressure in the quadrant θ∈[180,270] degrees highlighted in yellow in Fig. 2.1(a). To evaluate the displacement field of the annulus, it was modeled by 4-node shell finite elements within Nastran (CQUAD4 elements) with a mesh of 144 nodes around the periphery and 6 in the radial direction. Then, shown in Fig. 1(b) is the transverse displacement of the periphery which is clearly localized near the excitation, i.e., in the band θ∈[150,300] degrees.

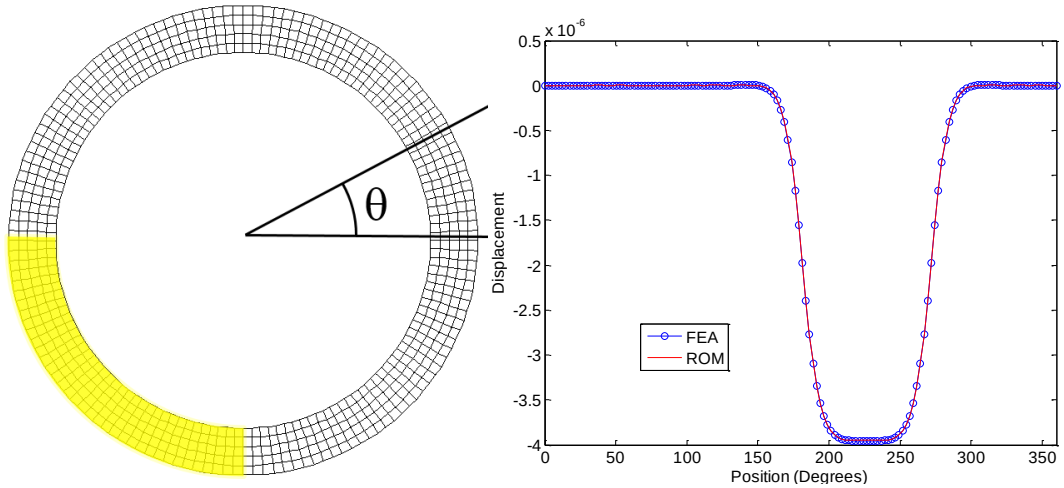

(a)¶ (b)

Figure 2.1. (a) the Annulus and Its Finite Element Model with the Loading Domain Highlighted in Yellow. (b) Static Transverse Displacement at the Periphery, Full Finite Element (FEA) and Reduced Order Models (ROM).

A reduced order model of the finite element one can be constructed by representing the nodal responses stacked in the vector $\underline{u}$ as a linear combination of basis functions $\underline{\Psi}_i$, i.e. as

$$\underline{u} = \sum_{i=1}^{M} q_i \, \underline{\Psi}_i \tag{2.1}$$

where the variables q_i are referred to as generalized coordinates. The adoption of the representation of Eq. (2.1) transforms the equations for the nodal displacements

$$\overline{K}_{FE}\,\underline{u} = \underline{\overline{F}}_{FE} \tag{2.2}$$

where $\overline{K}_{FE}$ and $\underline{\overline{F}}_{FE}$ are the finite element stiffness matrix and loading, into

$$\overline{K}\,\underline{q} = \underline{\overline{F}} \tag{2.3}$$

where

$$\overline{K} = \Psi^T \overline{K}_{FE}\,\Psi \qquad \text{and} \qquad \underline{\overline{F}} = \Psi^T \underline{\overline{F}}_{FE} \tag{2.4}$$

with ^{T} denoting the operation of matrix transposition and $\Psi = \left[\underline{\psi}_1\, \underline{\psi}_2\, \underline{\psi}_3 \cdots \underline{\psi}_M\right]$.

The above reduced order model construction was exemplified by selecting the basis functions $\underline{\psi}_i$ as the linear modes of the annulus. Then, shown in Fig. 2.1(b) is the transverse displacement of the periphery obtained with 55 such modes which, as expected, closely approximates the finite element solution.

2.2.2. Class B Structures

A second type of structures that exhibit a localization of the static response are those that are composed to sub-structures weakly coupled to each other. A very simple example of this situation is the chain of oscillators showed in Fig. 2.2(a). To demonstrate the localization, the chain was selected to have 12 masses connected to their neighbors by a spring of common stiffness k_C = 0.15 N/m and to ground by different springs, of respective stiffnesses (from mass 1 to 12): 1.45; 1.69; 2.20; 2.86; 3.71; 4.83; 5.07; 5.32; 5.59; 5.87; 6.16; 6.62 N/m. Moreover, the chain was assumed to be open at its two ends. Then, shown in Fig. 2.2(b) is the static response of the chain under uniform forces acting

on the masses 3, 4, and 5. It is clearly observed that the static response is localized to the three masses on which the loading is applied.

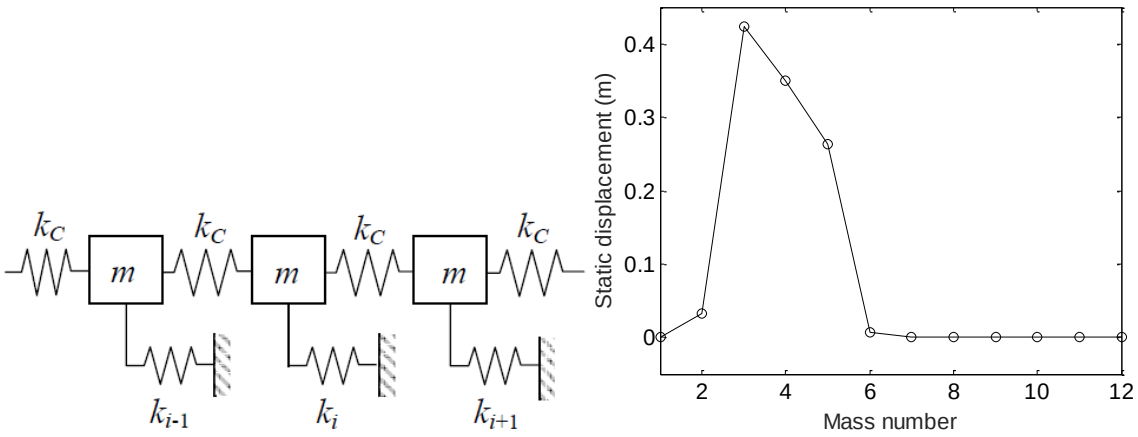

(a) (b)

Figure 2.2. (a) The chain discrete model. (b) Static response of the chain due to unit loads on masses 3, 4, and 5.

2.2.1. Class C Structures

Bladed disks are a class of structures with peculiar properties and with geometric features that are in between those of the class A and B structures described above. They are continuous structures, such as the annulus of Fig. 2.1, but with discrete features (the blades) that are often weakly coupled to each other (especially in the lowest frequency modes), as the chain model of Fig. 2.2. Shown in Fig. 2.3(a), (b) is a representative 12-blade bladed disk (it is a reduction of the number of blades to 12 of the 24-blade one considered in (Bladh et al 2001)) and shown in Fig. 2.3(c) is the static response at the tip of the 12 blades induced by a unit force applied at the tip of blade 1. Clearly, this response is very localized (note the logarithmic scale of the ordinates).

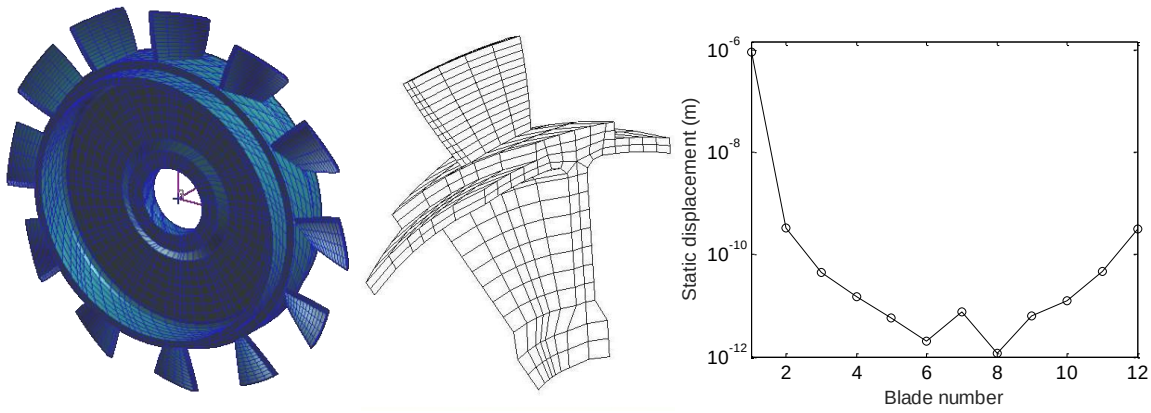

(a) (b) (c)

Figure 2.3. Bladed Disk Example: (a) Overall View, (b) Blade Sector Finite Element Mesh, and (c) Static Response at Blade Tip Due to Unit Load at the Tip of Blade 1.

2.3. "Standard" Maximum Entropy Nonparametric Approach

The maximum entropy nonparametric approach introduced in Chapter 1 was applied as is to the 55x55 stiffness matrix of the reduced order model of the annulus and 300 random matrices K were determined. From each one of those, a set of generalized coordinates $\underline{q}$ was determined that satisfies

$$K\,\underline{q} = \underline{\overline{F}} \tag{2.5}$$

and the resulting set of nodal displacements $\underline{u}$ were obtained from Eq. (2.1). Shown in yellow in Fig. 2.4(a) is the uncertainty band corresponding to the 5th and 95th percentile of the transverse displacement of the periphery as determined from the 300 samples of the response. Comparing Figs 2.1(b) and 2.4(a), it is observed that the above uncertainty modeling approach has induced some *globalization* of the response, i.e., the response outside of the region $\theta \in [150,300]$ degrees is not nearly zero for all samples as could have been construed from Fig. 2.1(b). Note that this effect likely leads to a higher entropy *of the response* as compared to the localized case given its increased spread of the joint

probability density function of this response. This finding seems quite consistent with, although separate from, the maximization of entropy *of the matrix K* which is guaranteed by the construction of Eqs (2.2)-(2.4).

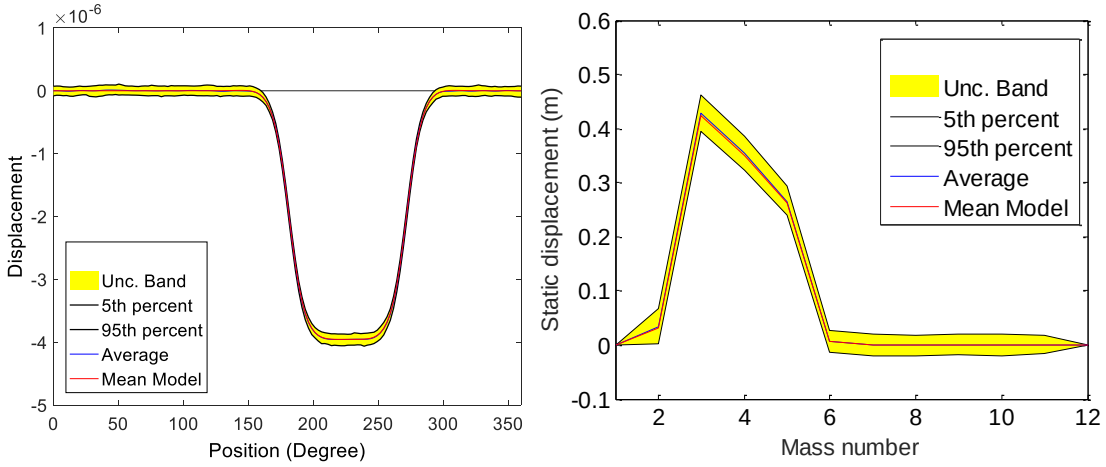

(a) (b)

Figure 2.4. (a) Static Transverse Displacement at the Periphery of the Annulus and (B) Static Displacement of the 12 Masses of the Chain Model. Mean Model (in Red) and 5th-95th Percentile Uncertainty Band (in Yellow) of the Displacement, Standard Stochastic Reduced Order Model with (a) $\delta = 0.05$, (b) $\delta = 0.1$.

As an additional example, shown in Fig. 2.4(b) is the 5th and 95th percentile of the static response of the 12 masses of the chain example of Fig. 2.3 which is seen to exhibit an uncertainty-induced globalization of the response.

It is important to recognize that the above globalization effects are certainly *physically possible*. For the annulus, they could for example take place if the disk on which the annulus is clamped is not rigid as specified in the mean model but rather exhibits some flexibility which induces a long range interaction between nodal responses.

If, however, there is *additional knowledge* about the uncertainty that indicates that such a globalization does not take place, then the above methodology must be modified

to reflect it, e.g., by adding constraints in the optimization of the entropy or modeling differently the random stiffness matrix. One such modification is formulated below.

In concluding this section, it should be recognized that the localization of the response observed in Figs 2.1(b), 2.2(b), 2.3(c), and 4 is *in the neighborhood of the excitation* and thus this localization zone would move if the part of the structure loaded was to change. If the loading, and thus the zone of localization, is well defined and invariant, a substructuring approach could be developed in which this zone is a substructure with the rest of the structure another. Then, uncertainty could be introduced nonparametrically in the two substructures as discussed in (Soize and Chebli 2003). If the loading zone varies or is unknown when the model is constructed, this approach could still likely be used by substructuring the entire structure finely enough to capture the localization at the expense of an increase in the number of degrees of freedom in the model. The methods developed below are in contrast with this situation, keeping the modeling of the structure whole.

2.4. Maximum Entropy Nonparametric Modeling for Static Localized Responses

2.4.1. Local and Global Stiffness Matrices

Before revising the above standard nonparametric approach, it is necessary to identify the property of the stiffness matrices $\overline{K}$ and $\overline{K}_{FE}$ that induces the existence of a localized response. To this end, recall that the solution $\underline{u}$ of Eq. (2.1) can be expanded in terms of the eigenvectors $\underline{\phi}_j$ and corresponding eigenvalues λ_j of $\overline{K}_{FE}$ as

$$\underline{u} = \sum_j \frac{\left(\underline{\phi}_j^T \underline{\overline{F}}_{FE}\right)}{\lambda_j} \underline{\phi}_j \tag{2.6}$$

owing to the orthogonality of the eigenvectors implied by the symmetry of $\overline{K}_{FE}$. Note in Eq. (2.6) and in the ensuing ones in this section that the summation is extended over all eigenvectors.

To proceed further in the discussion, assume first that the eigenvectors $\underline{\phi}_j$ are extended to the entire structure; this is true of the annulus of Fig. 2.1(a) (as well as the bladed disk of Fig. 2.3 but not the chain of Fig. 2.2) for which $\underline{\phi}_j$ are harmonic functions of the angle θ (as discretized by the finite element modeling). Then:

(i) a localized response as shown in Fig. 2.1(b) is possible only if the dominant coefficients $\left(\underline{\phi}_j^T \underline{\overline{F}}\right)/\lambda_j$ have somewhat similar values as to create an appropriate mix of the extended functions $\underline{\phi}_j$ to produce localization,

(ii) the "modal forces" $\underline{\phi}_j^T \underline{\overline{F}}$ decrease slowly as the index *j* is increased given the localization of the excitation or equivalently the values $\underline{\phi}_j^T \underline{\overline{F}}$ for the dominant modes tend to be quite similar.

Combining these two arguments, it is thus concluded that *localization must require that the lowest eigenvalues* λ_j *of* $\overline{K}_{FE}$ *be close together* if the eigenvectors of this stiffness matrix are extended. This result is confirmed by the plot of eigenvalues of the annulus' stiffness matrix shown in Fig. 2.5: the first few of its eigenvalues are indeed closely spaced.

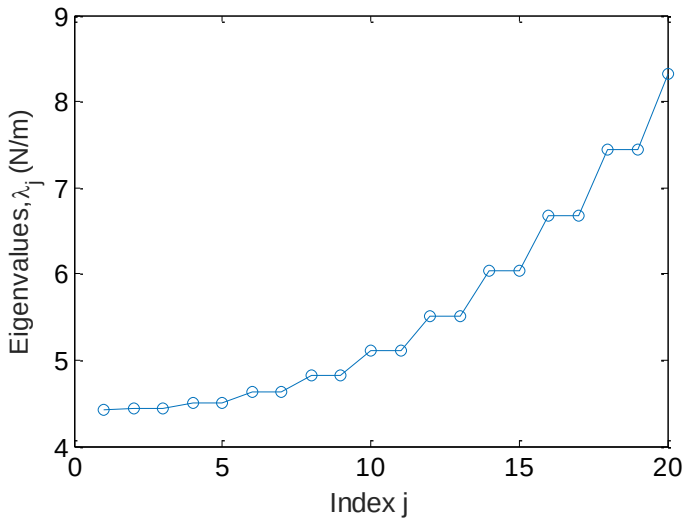

Figure 2.5. Eigenvalues of the Stiffness Matrix of the Annulus Finite Element in Increasing Order.

For structures with localized response and well separated eigenvalues of their stiffness matrix, e.g., the chain model, the change in stiffness matrix induced by the random matrix *H* (Eq. (1.2)) produces changes in the eigenvectors, most specifically populating the zeros or very small components with non-zero ones that produce the globalization effect.

The above comments suggest that what is important for localization is:

(i) the *relative separation* of the first few eigenvalues which must be small when the eigenvectors are extended (class A structures), or

(ii) the localized nature of the eigenvectors when the eigenvalues are not close together (class B structures).

To confirm the statement (i), rewrite Eq. (2.6) in the form

$$\underline{u} = \frac{1}{\lambda_1}\sum_j \left(\underline{\phi}_j^T \overline{\overline{F}}_{FE}\right)\underline{\phi}_j + \frac{1}{\lambda_1}\sum_j \frac{\left(\lambda_1 - \lambda_j\right)}{\lambda_j}\left(\underline{\phi}_j^T \overline{\overline{F}}_{FE}\right)\underline{\phi}_j \,. \qquad (2.7)$$

or

$$\underline{u} = \left[\frac{1}{\lambda_1} \sum_j \underline{\phi}_j \underline{\phi}_j^T \right] \underline{\overline{F}}_{FE} + \left[\frac{1}{\lambda_1} \sum_j \frac{\left(\lambda_1 - \lambda_j\right)}{\lambda_j} \underline{\phi}_j \underline{\phi}_j^T \right] \underline{\overline{F}}_{FE} = \overline{P}_1 \underline{\overline{F}}_{FE} + \overline{P}_2 \underline{\overline{F}}_{FE} . \quad (2.8)$$

where $\overline{P}_1$ is proportional to the identity matrix and thus $\overline{P}_1 \underline{\overline{F}}_{FE}$ is a purely local term, i.e., the corresponding displacement at each node only depends on the force acting at that node. This term will dominate when the terms $\left(\underline{\phi}_j^T \underline{\overline{F}}_{FE}\right)\left(\lambda_1 - \lambda_j\right)/\lambda_j$ are all small, i.e., when the dominant eigenvectors (those with significant values of $\underline{\phi}_j^T \underline{\overline{F}}_{FE}$) have a small relative difference of eigenvalue with eigenvector 1.

A similar discussion to the above one applies for the mean reduced order stiffness matrix $\overline{K}$ of eigenvectors $\underline{\varphi}_j$ and eigenvalues μ_j so that

$$\underline{q} = \overline{Q}\,\underline{\overline{F}} = \left[\frac{1}{\mu_1} \sum_j \underline{\varphi}_j \underline{\varphi}_j^T \right] \underline{\overline{F}} + \left[\frac{1}{\mu_1} \sum_j \frac{\left(\mu_1 - \mu_j\right)}{\mu_j} \underline{\varphi}_j \underline{\varphi}_j^T \right] \underline{\overline{F}} = \overline{Q}_1 \underline{\overline{F}} + \overline{Q}_2 \underline{\overline{F}} . \quad (2.9)$$

Associated to this decomposition of the flexibility matrix $\overline{Q}$ into a component inducing local effects ($\overline{Q}_1$) and a more global one ($\overline{Q}_2$) is a similar split of the stiffness matrix $\overline{K}$ into a local component, $\overline{K}_L$, and a more global one, $\overline{K}_G$, defined as

$$\overline{K}_L = \left[\overline{Q}_1\right]^{-1} = \mu_1 \sum_j \underline{\varphi}_j \underline{\varphi}_j^T \qquad \text{and} \qquad \overline{K}_G = \overline{K} - \overline{K}_L \qquad (2.10a),(2.10b)$$

where the summation in Eq. (2.10a) is extended over all eigenvectors/eigenvalues leading to the localization of the response.

2.4.2. Local/Global Maximum Entropy Nonparametric Modeling

The above discussion has demonstrated that a localization of the response will only occur in class A structures when the relative spread of the dominant eigenvalues of the

stiffness matrix is small. However, this spread is often increased, sometimes very significantly for the first few eigenvalues, when using the standard nonparametric approach as shown in Fig. 2.6.

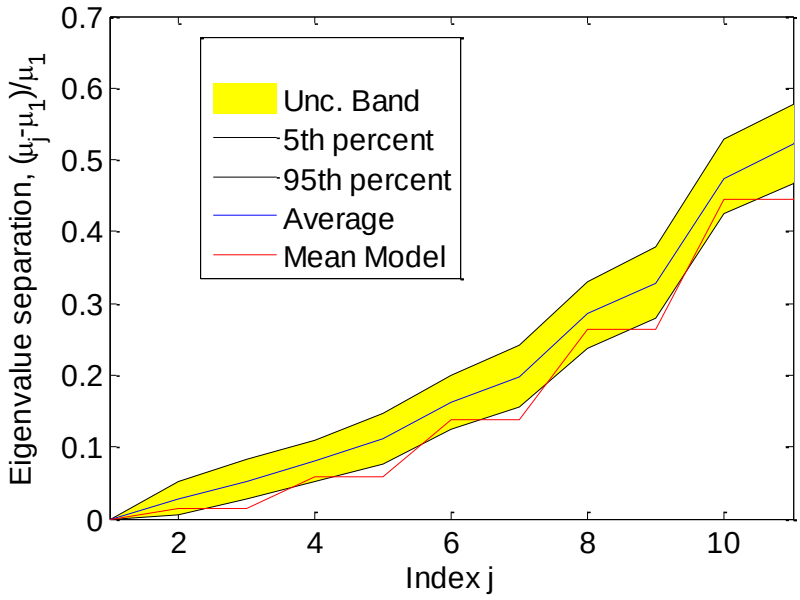

Figure 2.6. Relative Eigenvalue Separation of the Reduced order Model Stiffness Matrix. Mean Model (in Red) and 5th-95th Percentile Uncertainty Band (in Yellow), Standard Nonparametric Stochastic Model.

Thus, imposing a localization constraint on the stochastic modeling will require controlling the eigenvalues of the dominant modes (those with eigenvalues close to λ_1) separately from the rest of them. In this regard, note that the dominant eigenvectors are mostly present in $\overline{K}_L$ while those with eigenvalues far from λ_1 are dominant in $\overline{K}_G$.

On the basis of the above observations, it is proposed here to model the uncertainty in $\overline{K}_L$ and $\overline{K}_G$ separately. Since there is no particular requirement on the latter matrix (which is nevertheless symmetric and positive definite) and its randomization, the standard nonparametric approach will be applied leading to an uncertain matrix K_G defined as

$$K_G = \bar{L}_G \, H_G \, H_G^T \, \bar{L}_G^T \qquad \text{where} \qquad \bar{K}_G = \bar{L}_G \, \bar{L}_G^T \qquad (2.11a),(2.11b)$$

with H_G a lower triangular random matrix as defined by Eqs (1.3)-(1.4) and Fig. 1.1 for a particular dispersion value δ_G.

Maintaining small the relative separation between the eigenvalues of the dominant eigenvectors can be achieved by scaling uniformly all eigenvalues. This observation suggests that a first approach to introduce uncertainty in $\bar{K}_L$ is to simply multiply it by a random variable Λ which consistently with the maximum entropy concepts can be selected as H_1^2 where H_1 is a 1x1 matrix defined as in Eqs (1.3)-(1.4) and Fig. 1.1 with a specified dispersion δ_1.

A small change in the relative separation between eigenvalues can also be induced by splitting $\bar{K}_L$ as $\bar{K}_G$ in Eq. (2.11) and introducing a random lower triangular matrix H_L of dispersion δ_L. Combining the above two operations leads to the proposed model

$$K_L = H_1^2 \, \bar{L}_L \, H_L \, H_L^T \, \bar{L}_L^T \qquad \text{where} \qquad \bar{K}_L = \bar{L}_L \, \bar{L}_L^T . \qquad (2.12a),(2.12b)$$

Note finally that since $\bar{K}_L$ is defined by Eq. (2.10a), its decomposition in Eq. (2.12b) is readily achieved by selecting

$$\bar{L}_L = \sqrt{\mu_1} \left[\underline{\varphi}_1 \, \underline{\varphi}_2 \, \underline{\varphi}_3 \ldots \right] . \qquad (2.13)$$

The uncertain reduced order stiffness matrix is then obtained as

$$K = K_L + K_G . \qquad (2.14)$$

The above derivations have been carried out assuming that all eigenvectors were retained in Eq. (2.10a). From a practical perspective, it is sufficient to restrict it to the

eigenvectors corresponding to the set of close eigenvalues (class A structures) or to the localized eigenvectors excited by the loading (class B structures).

2.4.3. Algorithm

The application of the above approach can be decomposed into the following steps:

(a) selection of the basis functions $\underline{\psi}_i$ and computation of the mean ROM stiffness matrix $\overline{K}$ from its finite element counterpart $\overline{K}_{FE}$ using Eq. (2.4),

(b) determination of the eigenvectors $\underline{\varphi}_j$ and eigenvalues μ_j of the matrix $\overline{K}$,

(c) selection of the set (values of *j*) of these eigenvectors and eigenvalues that lead to localization, i.e., closely spaced eigenvalues (for class A structures) or localized eigenvectors (for class B structures),

(d) construction of the mean model matrices $\overline{K}_L$ and $\overline{K}_G$ according to Eqs (2.10a) and (2.10b),

(e) selection of the dispersion parameters δ_G, δ_1, and δ_L,

(f) computation of the decomposition matrices $\overline{L}_G$ and $\overline{L}_L$ satisfying Eqs (2.11b) and (2.12b),

(g) simulation of the random matrices K_G and K_L according to Eqs (2.11a) and (16a),

(h) assembly of the random stiffness matrices as in Eq. (2.14).

2.4.4. Applications

The three-parameter ($\delta_G, \delta_1, \delta_L$) stochastic model formulated above was first applied to the reduced order model of the annulus with the first 8 eigenvectors $\underline{\varphi}_j$

retained in the summation of Eq. (2.10a) and μ_1 selected as 0.99 times the lowest eigenvalue. To highlight the effects of each random component on the response, shown in Figs 2.7 (a),(c),(e) are the uncertainty bands obtained with each of the parameters set to a nonzero value in turn. Also shown, on Figs 2.7 (b),(d),(f) are 3 samples of the corresponding responses.

From Figs 2.7 (a),(b), corresponding to $\delta_G \neq 0$, it is observed that the randomization of $\overline{K}_G$ only leads to a small, rather constant, global uncertainty band consistently with the above discussions. Next, consider Figs 2.7 (c),(d) corresponding to $\delta_1 \neq 0$ and which leads to a very localized large variability of the response confirming that K_L does indeed control the localized behavior. Finally, shown in Figs 2.7 (e),(f) are the results corresponding to $\delta_L \neq 0$ which are very similar to those shown in Figs 2.7 (a),(b) suggesting, for the present application, that it is sufficient to only consider the two parameter model defined by δ_G and δ_1, i.e., with

$$K_L = H_1^2 \, \overline{K}_L \, . \tag{2.15}$$

Shown in Fig. 2.8 are the uncertainty band (Fig. 2.8(a)) and 3 samples of the response (Fig. 2.8(b)) corresponding to the combined case of all three parameters nonzero. It is seen that their effects approximately superpose, creating a thin uncertainty band away from the localization region but a much more significant one within it and samples that exhibit the localization as was desired.

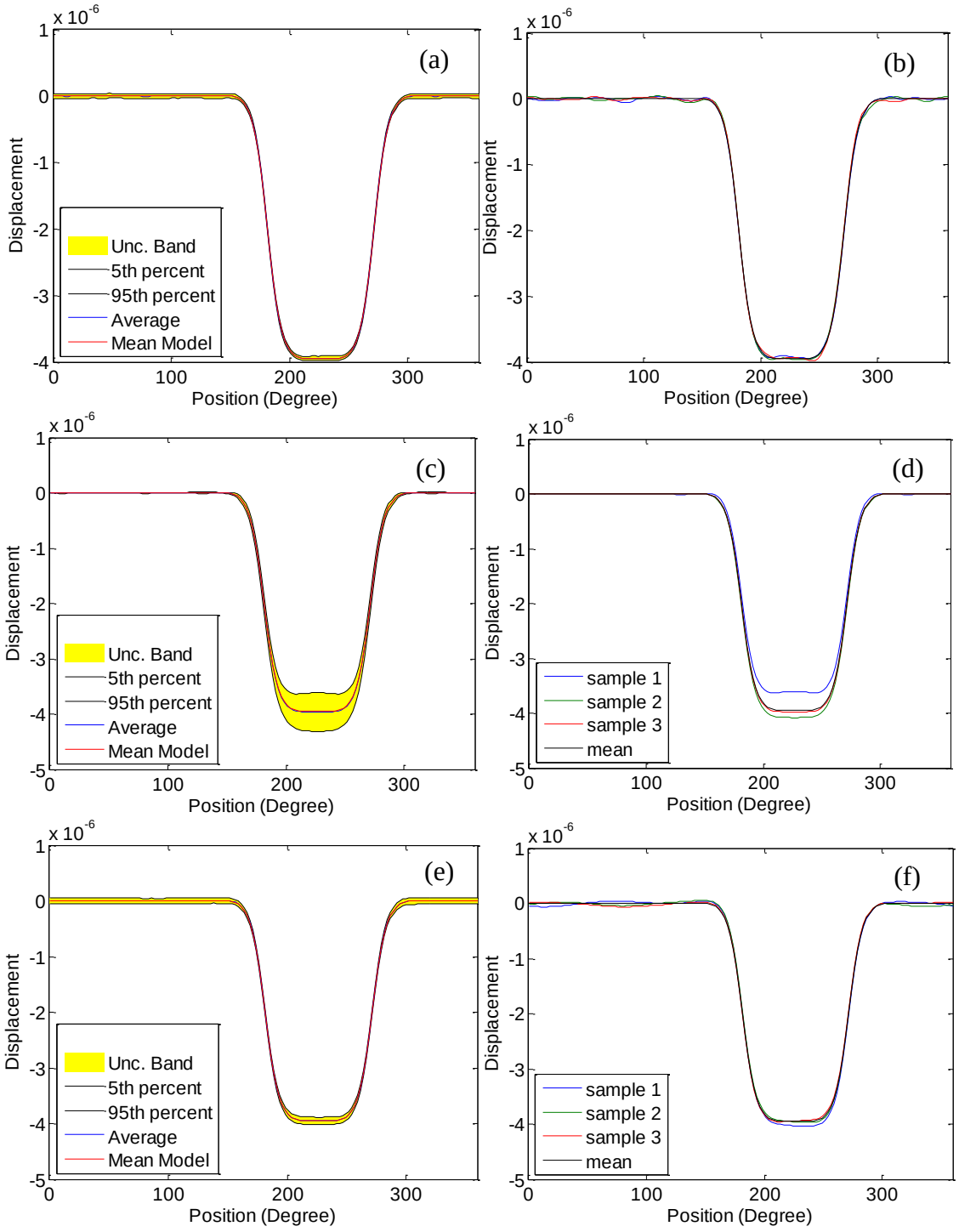

Figure 2.7. Static Transverse Displacement at the Periphery of the Mean Annulus (in Red) and Results from the Stochastic Reduced Order Model: (a),(c),(e) 5th-95th Percentile Uncertainty Band (in Yellow), (b),(d),(f) 3 Samples.(δ_G , δ_1 , δ_L) = (a),(b) (0.1,0,0); (c),(d) (0,0.05,0); (e),(f) (0,0,0.02)

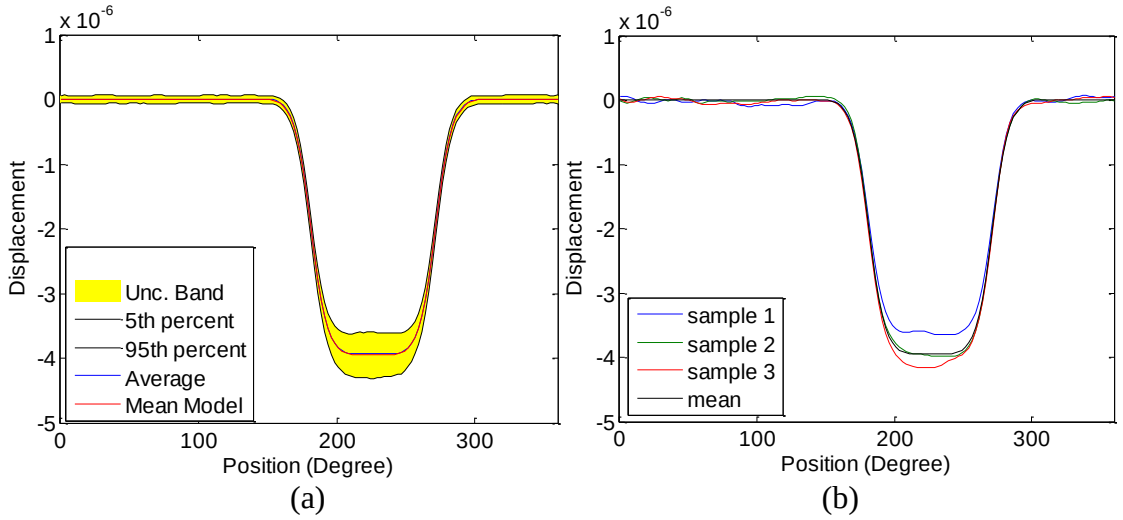

Figure 2.8. Static Transverse Displacement at the Periphery of the Mean Annulus (in Red) and Results from the Stochastic Reduced Order Model: (a) 5th-95th Percentile Uncertainty Band (in Yellow), (b) 3 Samples. ($\delta_G, \delta_1, \delta_L$)=(0.1,0.05,0.02).

Not only does the uniform shift of the close eigenvalues of the stiffness matrix induced by Eq. (2.15) produce localization of the uncertain response but it also appears to be the main mechanism to induce this localization. To clarify this issue, consider a parametric stochastic model of the annulus in which only the Young's modulus is uncertain, more specifically represented according to the model of (Soize 2006) as a 1x1 matrix. Selecting the dispersion parameter δ (equal to the coefficient of variation here) equal to 0.1 and the correlation length to 0.43 (corresponding to an arc of approximately 30 degrees of the inner radius) led to the uncertain bands shown in Fig. 2.9(a). As expected, the response is localized to the neighborhood of the excitation.

Next, the random finite element matrix K_{FE} was projected on the 55 linear modes of the mean model selected to construct the corresponding random ROM stiffness matrix $\hat{K}$. It was itself projected on the first 8 eigenvectors of the mean model ROM stiffness matrix, generating

$$K_p = \left[\underline{\varphi}_1 \underline{\varphi}_2 \ldots \underline{\varphi}_8\right]^T \hat{K} \left[\underline{\varphi}_1 \underline{\varphi}_2 \ldots \underline{\varphi}_8\right] \quad \text{and} \quad \hat{K} = \Psi^T K_{FE} \Psi . \qquad (2.16a),(2.16b)$$

This step is straightforward here as the mean ROM stiffness matrix $\overline{K}$ is diagonal and thus the eigenvectors $\underline{\varphi}_i$ are entirely zero except for the component *i* equal to 1. Thus, K_p is the top left 8x8 block of $\hat{K}$.

The random matrix K_p plays a role very similar to K_L as it captures the variability associated with the first 8 eigenvectors of the mean model ROM stiffness matrix. Then, according to Eq. (2.15), this matrix was tentatively approximated by

$$K_p = \overline{K}_p + d\ I_8 \qquad (2.17)$$

where $\overline{K}_p$ denotes the mean of K_p which is a diagonal matrix with elements μ_1, μ_2, ..., μ_8, *d* is a centered random variable, and I_8 denotes the 8x8 identity matrix. To assess the quality of this approximation, each sample of the matrix K_p was first considered and the corresponding value of *d* minimizing the error

$$\varepsilon = \left\| K_p - \overline{K}_p - d\ I_8 \right\|_F \qquad (2.18)$$

was obtained. In this equation, the symbol $\| \ \|_F$ denotes the Frobenius norm of a matrix. Proceeding with a straightforward differentiation led to

$$d = \frac{1}{8} tr\left[K_p - \overline{K}_p\right] \qquad (2.19)$$

where $tr[U]$ denotes the trace of an arbitrary matrix *U*. Introducing, this expression in the error ε yields its minimum value denoted as $\varepsilon_{\min}$. An overall approximation error of K_p in the form of Eq. (2.17) can then be defined as

$$\varepsilon_A = \frac{E[\varepsilon_{\min}]}{E[\|K_p\|_F]}. \tag{2.20}$$

The above computations were carried out for the samples of Fig. 2.9(a) and it was found that $\varepsilon_A = 0.26$. This small value demonstrates that most of the variability in K_p can indeed be modeled by a uniform shift of eigenvalues.

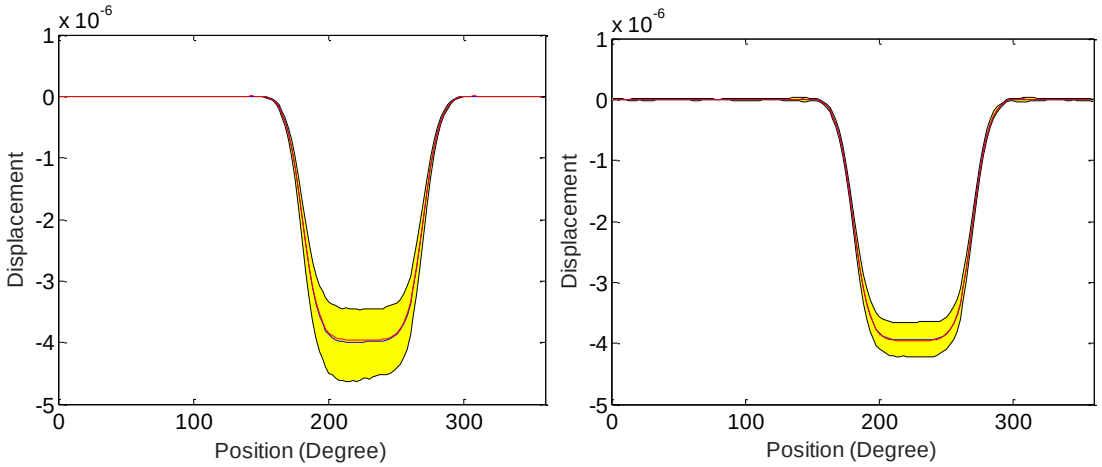

Figure 2.9. Static Transverse Displacement at the Periphery of the Mean Annulus (in Red) and Results from the Parametric Stochastic Model with Uncertain Young's Modulus Only. 5th-95th Percentile Uncertainty Band (in Yellow) Corresponding to (a) Full Finite Element Simulation, (b) ROM with the Matrix $\hat{K}$ Approximated.

To provide a final confirmation of the appropriateness of the stochastic model of Eqs (2.10)-(2.14), the computation of the static response of the annulus was carried out by

(i) replacing K_p by $\overline{K}_p + d\, I_8$ as the 8x8 top left block of the matrix $\hat{K}$

(ii) zeroing out the remaining elements of the first 8 rows and columns of $\hat{K}$ to approximately parallel the structure of *K*, Eq. (2.14), since these elements are small, of the order of $\mu_i - \mu_1$.

Then, shown in Fig. 2.9(b) is the uncertainty band on the response obtained by utilizing the above modified $\hat{K}$ matrix as ROM stiffness matrix. Comparing this figure with its original counterpart, Fig. 2.9(a), it is observed that the results are very similar with only a difference in the width of the band. This finding is fully expected as the projection process of Eqs (2.17)-(2.19) has effectively decreased the overall level of uncertainty and thus a thinner uncertainty band is expected. A rescaling of the variability of the random parameter *d* would boost back the band to its width in Fig. 2.9(a). This scaling could be seen as a calibration of the model to the data of Fig. 2.9(a).

The three-parameter ($\delta_G, \delta_1, \delta_L$) stochastic model was also applied to the chain model with the eigenvectors $\underline{\varphi}_3$, $\underline{\varphi}_4$, and $\underline{\varphi}_5$, i.e., the eigenvectors significantly excited by the loading, retained in the summation of Eq. (2.10a). Moreover, the parameter μ_1 was selected equal to 0.99 times the third eigenvalue (the lowest eigenvalue corresponding to the retained eigenvectors). Then, shown in Fig. 2.10 is the uncertainty band corresponding to the case δ_G=0.1, δ_1=0.1, and δ_L=0. It is again observed that the uncertain response is localized to the masses 3, 4, and 5 as is the mean model.

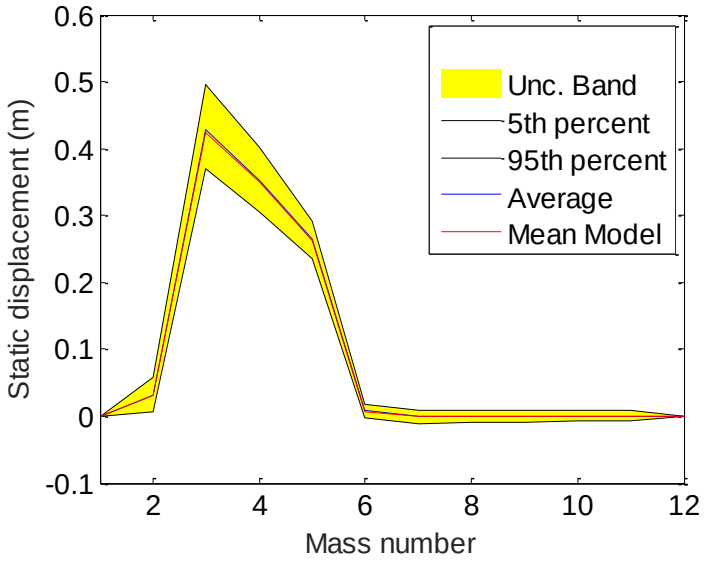

Figure 2.10. Static Displacement of the Chain Model. Mean Model (in Red) and 5th-95th Percentile Uncertainty Band (in Yellow) for (δ_G, δ_1, δ_L)=(0.1,0.1,0).

2.5. Maximum Entropy Nonparametric Modeling for Mode Shapes Localization

The discussion of the above section focused on maintaining the localized character of the response of the mean model when introducing uncertainty. In contrast to this situation, there exists a class of structures in which the mean model response is global but the introduction of uncertainty induces localization. Bladed disks, i.e., the structures of class C, are notorious examples of this situation when analyzing the free response properties, i.e., mode shapes. Rather typically, consider the finite element model of the bladed disk of Fig. 2.3 in which all blades have identical properties (i.e., the *tuned* disk) and shown in Fig. 2.11 are 2 of its low frequency modes more specifically those corresponding to 2 and 6 nodal diameters of the first family. Clearly, these mode shapes are extended to the entire structure, i.e., global. Next, blade-to-blade variations in their Young's modulus are introduced to create *mistuning*. Given the quality of the manufacturing process, these differences can be expected to be small and thus the

Young's moduli of the 12 blades were selected as 0.995, 0.996, 0.997, 0.998, 0.999, 1.000, 1.001, 1.002, 1.003, 1.004, 1.005, 1006 of the tuned model value. Then, shown in Fig. 2.12 are two typical low frequency modes and note that they are very strongly localized to only 1 blade out of the 12, on different blades for different modes. An additional observation that has been made in relation to mistuning is that variations of properties of the disk (the support of the blades) does not lead in itself to localization. The dominant sensitivity of the modes is thus with respect to blade-to-blade variations of their properties.

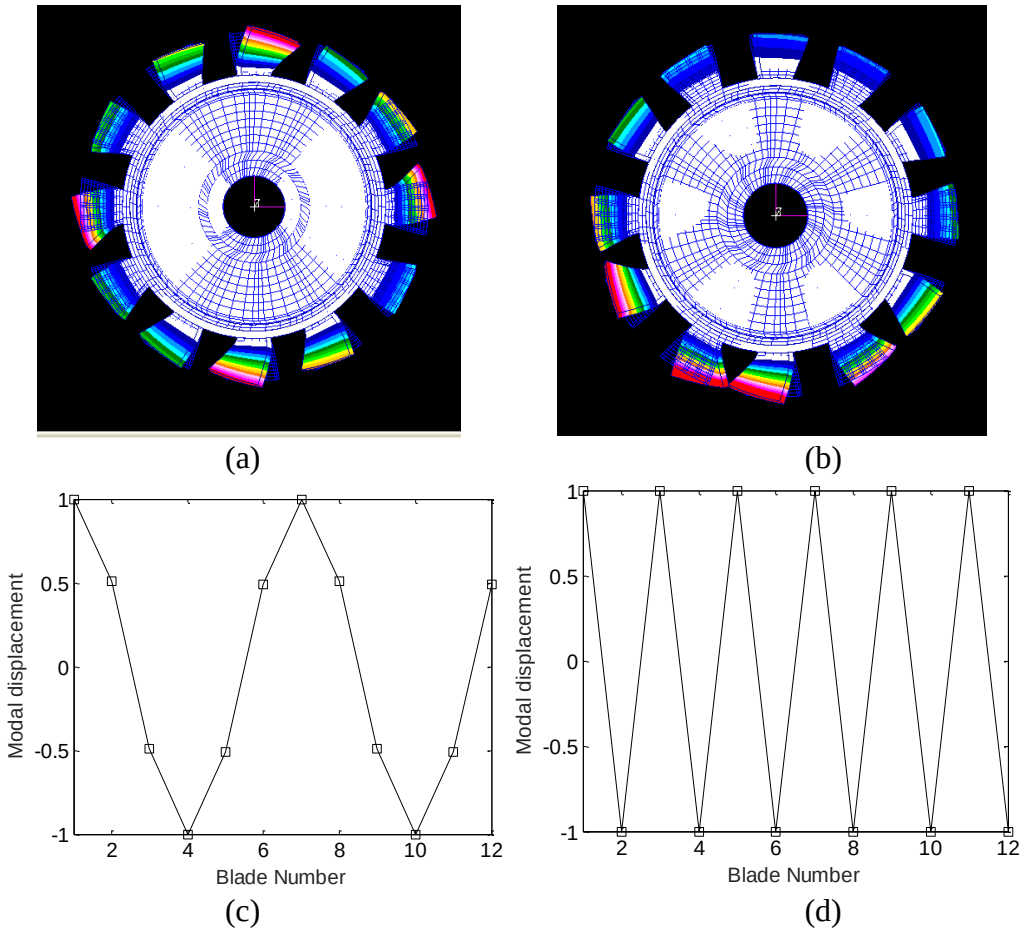

Figure 2.11. Some Mode Shapes of the First Family, Tuned Bladed Disk Model. (a), (b) Overall View, (c), (d) Tip Displacements. (a), (c) 2 Nodal Diameter Modes, (b), (d) 6 Nodal Diameter Modes

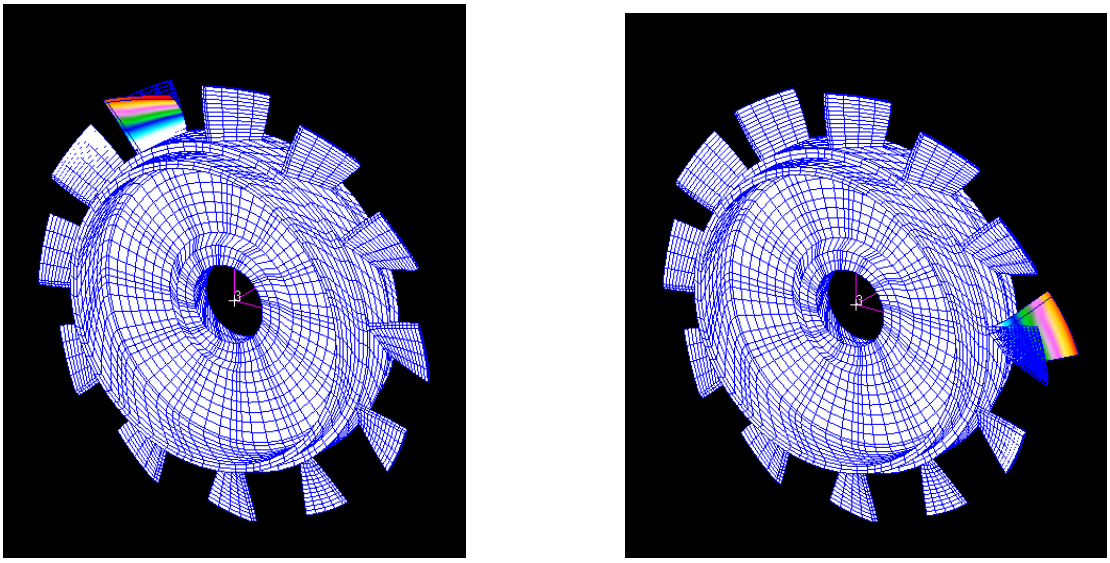

Figure 2.12. Overall View of Some Mode Shapes of the First Family, Mistuned Bladed Disk.

It is desired here to duplicate these phenomenological effects by introducing uncertainty on a reduced order model of the bladed disk. In this regard, it ought to be recognized that there are reduced order modeling methods which are more apt than others at mistuning the *blades* vs. mistuning all components (disk and blades). For example, sub-structuring based reduced order models (e.g., following a Craig-Bampton approach) in which each blade is a particular sub-structure are particularly convenient for the introduction of blade mistuning as the response of each blade is associated with specific ROM degrees of freedom. The intent here is to consider a "worst case" scenario, more specifically a reduced order model based on a series of tuned modes of the bladed disk in which the blades specific degrees of freedom are lost. This was achieved for the bladed disk of Fig. 2.3 by selecting the first 200 modes of the tuned model.

It was first questioned whether the standard nonparametric method of Eqs (1.1)-(1.4) and/or the revised approach of Eqs (2.10)-(2.12) could generate strongly localized modes

as seen in Fig. 2.12. To this end, shown in Fig. 2.13 are the first two modes obtained for a particular mistuned disk realization and with each of these methods. It is clearly seen that most of these modes are *distorted* but are not *localized*. In fact, the results corresponding to $(\delta_G, \delta_1, \delta_L)$=(0,0.1,0) are neither distorted nor localized as they correspond to a tuned disk with properties different than the baseline one. These observations are not surprising: the transformation from physical coordinates to modal ones spreads the uncertainty well defined on blades to the ensemble of modal elements in the ROM mass and/or stiffness elements. This process induces specific correlations between the elements of these matrices that are not, and cannot be expected to be, duplicated by the nonparametric approaches. Accordingly, a revised of the approach of Eqs (2.10)-(2.12) is proposed below for this class of applications.

More specifically, it is suggested that the randomization of the local component of the ROM stiffness matrix of Eq. (2.10a), denoted here as $\overline{K}_{L,ROM}$, be done in the finite element domain, then mapped back to the ROM by pre and post multiplication by Ψ^T and Ψ. Moreover, this randomization should affect only diagonal elements in the finite element domain to not modify the connectivity of various degrees of freedom, i.e., not to create a coupling (for example between blades) that does not exist in the mean model. That is, the uncertainty on $\overline{K}_{L,ROM}$ should originate from the diagonal component of a finite element space matrix $\overline{K}_{L,FEM}$ satisfying

$$\overline{K}_{L,ROM} = \Psi^T \overline{K}_{L,FEM} \Psi . \tag{2.21}$$

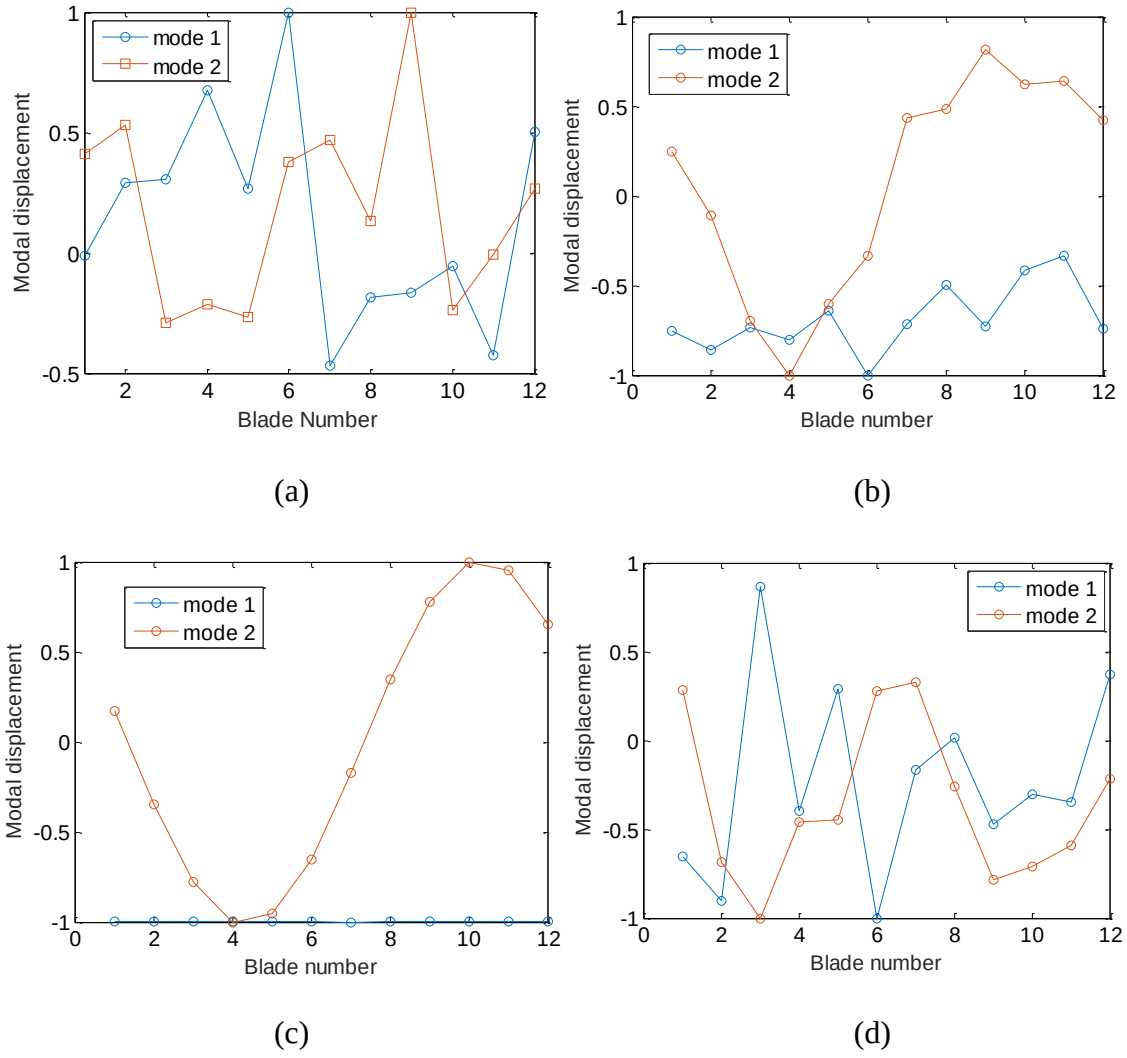

Figure 2.13. Tip Displacements of the First Two Modes for a Particular Mistuned Disk Realization Obtained with (a) Standard Nonparametric Method, δ =0.1, the Revised Approach of Eq. (2.10) with (b) $(\delta_G, \delta_1, \delta_L)$=(0.1,0,0), (c) $(\delta_G, \delta_1, \delta_L)$=(0,0.1,0), and (d) $(\delta_G, \delta_1, \delta_L)$=(0,0,0.1).

This matrix will be expressed similarly to $\overline{K}_{L,ROM}$, i.e., as

$$\overline{K}_{L,FEM} = \mu_1 \sum_j \underline{z}_j \underline{z}_j^T = \mu_1 Z Z^T \tag{2.22}$$

where μ_1 is an appropriately selected parameter (see below) and Z is the matrix of columns $\underline{z}_j$ with these vectors satisfying the underdetermined system of equations

$$\Psi^T \underline{z}_j = \underline{\varphi}_j . \tag{2.23}$$

Proceeding with a least squares solution of the equations yields

$$\underline{z}_j = \Psi\left[\Psi^T \Psi\right]^{-1} \underline{\varphi}_j \tag{2.24}$$

which then completely defines $\overline{K}_{L,FEM}$. Note in the above equations that the indices *j* range over all eigenvectors/eigenvalues leading to the localization of the response.

As stated above, the plan is to induce localization of the mode shapes by randomizing the diagonal component of $\overline{K}_{L,FEM}$, denoted as $\overline{K}_{L,FEMD}$ or

$$\overline{K}_{L,FEMD} = diag\left[\overline{K}_{L,FEM}\right] = \mu_1 \, diag\left[Z \; Z^T\right]. \tag{2.25}$$

Then, the off-diagonal component of $\overline{K}_{L,FEM}$ can be regrouped with the previous global part of the ROM stiffness matrix to form the new $\overline{K}_G$

$$\overline{K}_G = \overline{K} - \overline{K}_{L,ROM} + \Psi^T \left[\overline{K}_{L,FEM} - \overline{K}_{L,FEMD}\right]\Psi = \overline{K} - \Psi^T \overline{K}_{L,FEMD}\Psi . \tag{2.26}$$

Given this split of the mean model stiffness matrix into local and global components, it is proposed to introduce uncertainty on $\overline{K}_G$ as in Eq. (2.11) but the randomization of $\overline{K}_{L,FEMD}$ will require that this matrix remains diagonal (see discussion above). To this end, it is proposed to proceed in parallel with Eq. (2.12a) with a "scaling" (scalar H_1^2) and a "distortion" (matrix H_Z), that is

$$K_{L,FEMD} = \mu_1 H_1^2 \; diag\left[Z \; H_Z \; H_Z^T Z^T\right] \tag{2.27}$$

where the matrix H_Z is a lower triangular random matrix defined by Eqs (1.3)-(1.4) and Fig. 1.1 for a particular dispersion δ_Z. Regrouping terms, the random ROM stiffness matrix is then

$$K = K_G + \Psi^T K_{L,FEMD} \Psi . \tag{2.28}$$

2.5.1. Algorithm

The application of the above approach can be decomposed into the following steps:

(a) selection of the basis functions $\underline{\psi}_i$ and computation of the mean ROM stiffness matrix $\overline{K}$ from its finite element counterpart $\overline{K}_{FE}$ using Eq. (2.4),

(b) determination of the eigenvectors $\underline{\varphi}_j$ and eigenvalues μ_j of the matrix $\overline{K}$,

(c) selection of the set (values of *j*) of these eigenvectors and eigenvalues that will lead to localization of the uncertain response, i.e., closely spaced eigenvalues for the bladed disk example,

(d) determination of the corresponding columns $\underline{z}_j$ according to Eq. (2.24),

(e) construction of the mean model matrix $\overline{K}_{L,FEMD}$ according to Eq. (2.25),

(f) determination of the mean stiffness matrix $\overline{K}_G$ from Eq. (2.26),

(g) selection of the parameter μ_1 which is as large as possible while maintaining the positive definiteness of the matrix $\overline{K}_G$,

(h) selection of the dispersion parameters δ_G, δ_1, and δ_L,

(i) simulation of the random matrices $K_{L,FEMD}$ according to Eq. (2.27),

(j) computation of the decomposition matrix $\overline{L}_G$ satisfying Eq. (2.11b),

(k) simulation of the random K_G according to Eq. (2.11a),

(l) assembly of the random stiffness matrices as in Eq. (2.28).

2.5.2. Application

The above modeling procedure was applied to the 200 modes ROM of the disk of Fig. 2.3 with the summation in Eq. (2.22) extending over the first 12 modes. Moreover, the parameter μ_1 was selected as the largest value for which the matrix $\overline{K}_G$ is positive definite. Then, shown in Fig. 2.14 are the four typical modes for a particular mistuned disk realization obtained with (δ_G, δ_1, δ_L) = (0.1, 0.1, 0.02). It is seen that these modes are indeed strongly localized to 1 or 2 blades as desired.

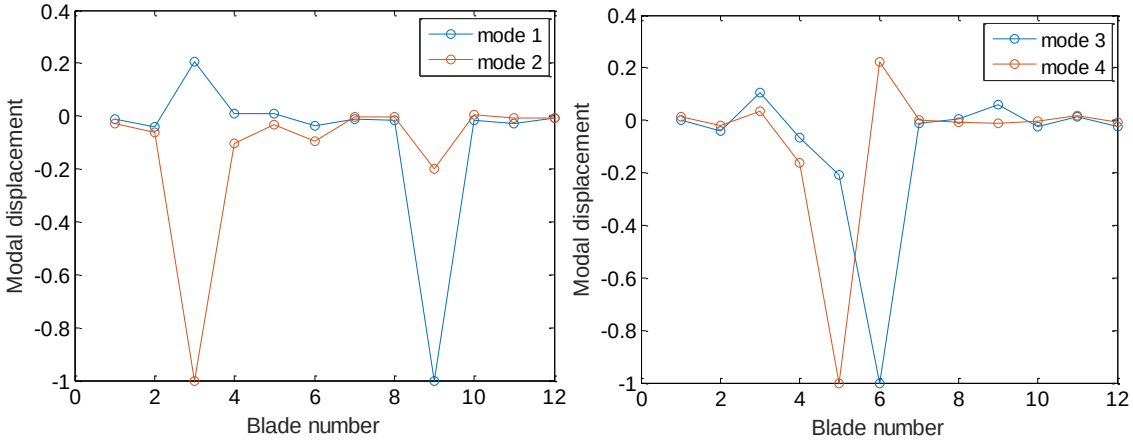

Figure 2.14. Tip Displacements of Four Typical Modes for a Particular Mistuned Disk Realization Obtained with the Approach of Eqs. (2.21)-(2.28) for (δ_G, δ_1, δ_L) = (0.1, 0.1, 0.02).

To better understand the role of each uncertainty mechanism on the occurrence of localization, the three cases (δ_G, δ_1, δ_L) = (0.1, 0, 0), (0, 0.1, 0), and (0, 0, 0.02) were also investigated and shown in Fig. 2.15 are some typical mode shapes of a particular realization of the bladed disk.

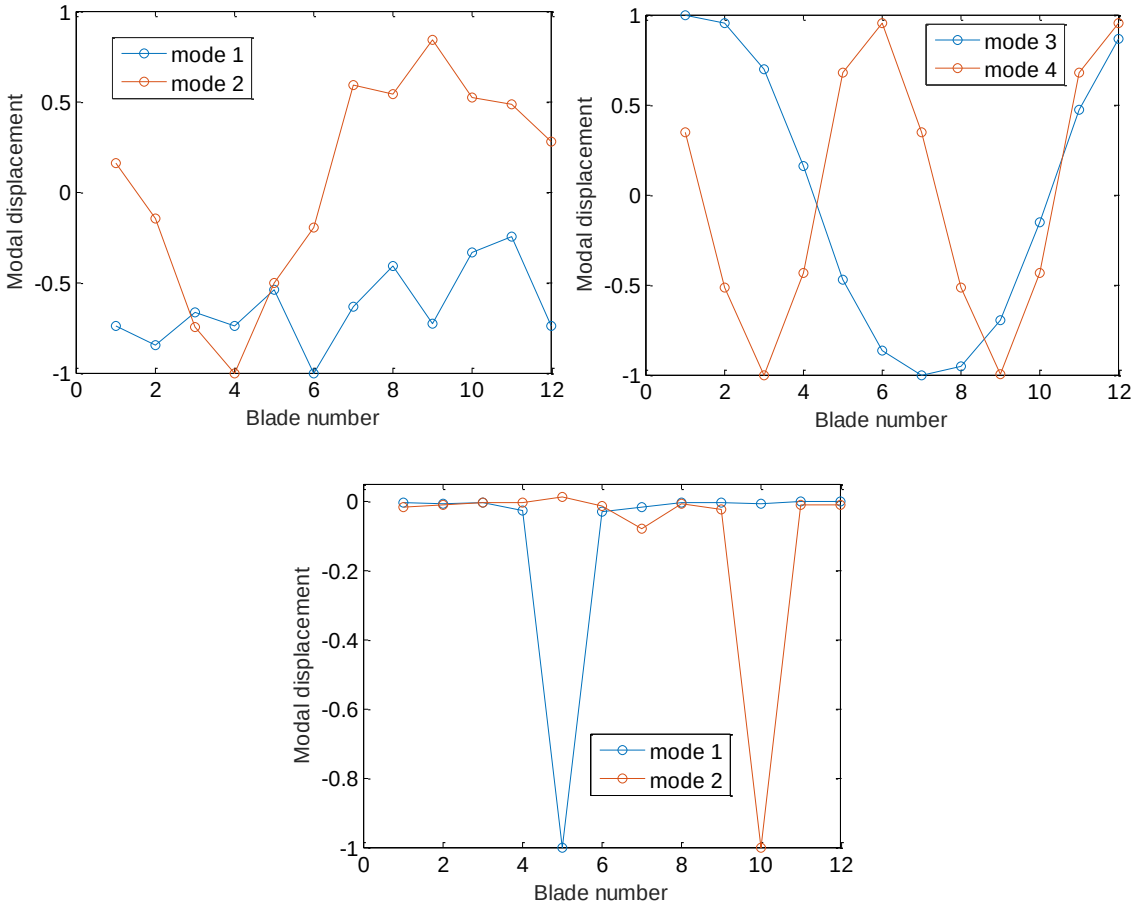

Figure 2.15. Tip Displacements of Some Typical Modes for a Particular Mistuned Disk Realization Obtained with the Approach of Eqs. (2.21)-(2.28) for (a) (δ_G, δ_1, δ_L) = (0.1, 0, 0), (b) (δ_G, δ_1, δ_L) = (0, 0.1, 0), and (c) (δ_G, δ_1, δ_L) = (0, 0, 0.02).

These figures demonstrate that:

(i) the effect of the uncertainty on K_G (controlled by δ_G) does induce distortion but not localization,

(ii) the uniform shift of eigenvalues (controlled by δ_1) creates neither distortion nor localization as it produces a tuned model different from the mean one,

(iii) that the mixing of eigenvalues induced by H_Z (controlled by δ_L) is the source of the localization of the modes.

This situation is in contrast with class A and B structures for which the mean model response is localized and where the uniform shift of eigenvalues, quantified by δ_1, is the dominant mechanism to be modeled.

While the above methodology has been described in the context of the stiffness matrix, it can be used in the same format to introduce uncertainty in the mass matrix. Specifically, one can decompose the mean ROM mass matrix $\overline{M}$ into local and global components with

$$\overline{M}_{L,FEMD} = diag\left[\overline{M}_{L,FEM}\right] = \eta_1 \; diag\left[Z \; Z^T\right] \tag{2.29}$$

and

$$\overline{M}_G = \overline{M} - \Psi^T \overline{M}_{L,FEMD} \Psi \quad . \tag{2.30}$$

Then, uncertain matrices $M_{L,FEMD}$ and M_G can be generated as

$$M_{L,FEMD} = \eta_1 H_1^2 \; diag\left[Z \; H_Z \; H_Z^T Z^T\right] \tag{2.31}$$

and

$$M_G = \overline{P}_G \; H_G \; H_G^T \; \overline{P}_G^T \qquad \text{where} \qquad \overline{M}_G = \overline{P}_G \; \overline{P}_G^T . \tag{2.32}$$

The uncertain ROM mass matrix is then obtained as

$$M = M_G + \Psi^T M_{L,FEMD} \Psi \quad . \tag{2.33}$$

For the selection of the matrix *Z*, it is desired through the local mass matrix to affect the natural frequencies which are closely spaced. Since the mean ROM mass matrix is identity here, the mean mode shapes are the corresponding eigenvectors of the mean

ROM stiffness matrix $\underline{\underline{\varphi}}_j$ and thus the selection of the vector $\underline{z}_j$ in Eq. (2.23) is still appropriate.

The above formulation was applied to the 200 modes ROM of the disk of Fig. 2.3 with the columns $\underline{z}_j$ determined from the first 12 modes. Moreover, the parameter η_1 was selected as the largest value for which the matrix $\overline{M}_G$ is positive definite. Given the above discussion on the role of the three different uncertainty mechanisms, the dispersion parameters ($\delta_G, \delta_1, \delta_L$) were first selected as (0, 0, 0.02). Then, shown in Fig. 2.16(a) are the first two modes for a particular mistuned disk realization; they are seen to be localized consistently with Fig. 2.15(c). Adding a random shift of the eigenvalues, i.e., with $\delta_1 \neq 0$, does not affect noticeably the modes, see Fig. 2.16(b), as may be expected since this shift only induces a tuned change to the system. Finally, the uncertainty on the global mass matrix M_G induces distortion of the modes, see Fig. 2.16(c) but not localization, again consistently with the stiffness based uncertainty results of Fig. 2.15.

Having successfully achieved localization producing mistuning, it was of interest to assess how to add further uncertainty to a bladed disk already mistuned. Since such a disk exhibits the properties of class A and B structures, i.e., its eigenvalues are closely spaced and the modes are localized, it was construed that the randomization approach of Eq. (2.10)-(2.12) would conserve the localization of the mode shapes. These properties were indeed confirmed for the mistuned disk of Fig. 2.12 for ($\delta_G, \delta_1, \delta_L$) = (0.1, 0.1, 0.0), the results not shown here for brevity.

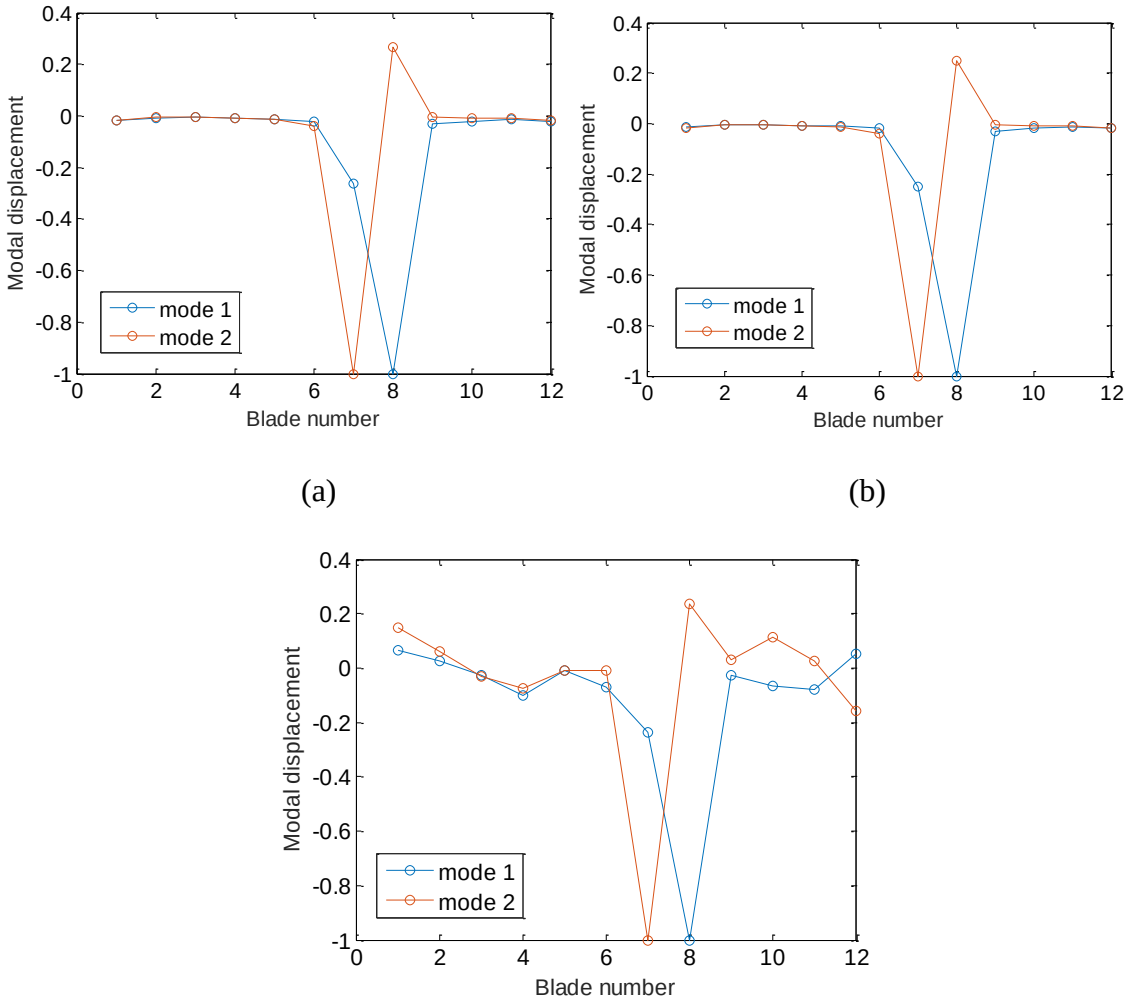

Figure 2.16. Tip Displacements of Some Typical Modes for a Particular Mistuned Disk Realization Obtained with the Approach of Eqs. (2.29)-(2.33) for (a) (δ_G , δ_1 , δ_L) = (0, 0, 0.02), (b) (δ_G , δ_1 , δ_L) = (0, 0.1, 0.02), and (c) (δ_G , δ_1 , δ_L) = (0.01, 0.1, 0.02).

3. NONLINEAR GEOMETRIC THERMOELASTIC RESPONSE OF STRUCTURES WITH UNCERTAIN THERMAL AND STRUCTURAL PROPERTIES

3.1. Introduction

The present Chapter focuses on the effects of uncertainty on the response of heated structures undergoing large deformations. In such multidisciplinary problems, the uncertainty may be associated with each discipline and/or with their coupling. Since the consideration of uncertainty on the structural properties alone has been discussed extensively before, this investigation will focus more specifically on the novel aspects of the uncertainty on the thermal properties (capacitance, conductance) and the thermal-structural coupling induced by the coefficient of thermal expansion. The propagation of these uncertainties to both temperature distribution and structural response will be determined. In this regard, note that thermal-structural coupling is effectively a one-way interaction. Indeed, the temperature distribution induces stresses in the structure that result in thermal loads and changes in its natural frequencies and mode shapes. In reverse however, the structural deformations directly affect the temperature distribution only through the very weak latency term which is ignored. A stronger coupling between the structural deformations and the temperature distribution may however exist in aero-structural-thermal problems since the structural motion will affect the aerodynamics and especially the aeroheating which drives the temperature distribution. This situation is not considered here. Moreover, it will be assumed that all properties are independent of temperature with the extension of the present formulations left as future work.

Owing to the potential or actual occurrence of thermal buckling, it is highly desirable to carry out the structural analysis in a nonlinear geometric format which, unfortunately,

leads to a significant increase in computational effort especially when considering dynamic situations. These conflicting requirements have led to the formulation and development of nonlinear thermal-structural reduced order modeling strategies for the temperature and displacements, see (Perez et al 2011) and (Matney et al 2011), which are based on similar developments for structural only models, see (Kim et al 2013, Mignolet et al 2013) and (Perez et al 2014).

3.2. Uncertainty Modeling

3.2.1. Modeling of Conductance and Capacitance Matrices

Uncertainty in the conductance and capacitance properties of the structure can be included in the reduced order model by modeling the corresponding ROM matrices (conductance and/or capacitance) using the above nonparametric approaches as these matrices are symmetric and positive definite.

3.2.2. Modeling of the Structural and Coupling Properties

The next task is the modeling of uncertainties in the material properties that affect the structural ROM, e.g., the tensor of elasticity, coefficient of thermal expansion. The intent here is on generating random values of the parameters $K_{ij}^{(1)}$, $K_{ijl}^{(2)}$, $K_{ijlp}^{(3)}$, $K_{ijl}^{(th)}$, and $F_{il}^{(th)}$ *directly*, as opposed to simulating the material properties in the finite element then mapping them to the ROM. To proceed in this manner, it is necessary to first establish the mathematical/physical properties that those parameters must satisfy, then construct simulation algorithms that maintain these properties for every sample.

Such an effort was carried out in (Mignolet and Soize 2008) for the structural alone problem, i.e., the simulation of the parameters $K_{ij}^{(1)}$, $K_{ijl}^{(2)}$, and $K_{ijlp}^{(3)}$. More

specifically, it was shown that a matrix $\boldsymbol{K}_B$ composed of these stiffnesses is positive definite. This property was derived from the following expressions (Kim et al 2013, Mignolet and Soize 2008)

$$K_{mn}^{(1)} = \int_{\Omega_0} \frac{\partial U_i^{(m)}}{\partial X_k} C_{iklp} \frac{\partial U_l^{(n)}}{\partial X_p} d\boldsymbol{X} \tag{3.1}$$

$$K_{mnp}^{(2)} = \frac{1}{2}\left[\hat{K}_{mnp}^{(2)} + \hat{K}_{pmn}^{(2)} + \hat{K}_{npm}^{(2)}\right] \tag{3.2}$$

where

$$\hat{K}_{mnp}^{(2)} = \int_{\Omega_0} \frac{\partial U_i^{(m)}}{\partial X_j} C_{ijkl} \frac{\partial U_r^{(n)}}{\partial X_k} \frac{\partial U_r^{(p)}}{\partial X_l} d\boldsymbol{X} \tag{3.3}$$

and

$$K_{msnp}^{(3)} = \frac{1}{2} \int_{\Omega_0} \frac{\partial U_i^{(m)}}{\partial X_j} \frac{\partial U_i^{(s)}}{\partial X_k} C_{jklw} \frac{\partial U_r^{(n)}}{\partial X_l} \frac{\partial U_r^{(p)}}{\partial X_w} d\boldsymbol{X} \,. \tag{3.4}$$

In these equations, Ω_0 denotes the domain of the structure in the undeformed configuration, $U_i^{(m)}(\boldsymbol{X})$ is the *m*th basis function for the representation of the *i*th component of the displacement vector over the continuous domain $\boldsymbol{X} \in \Omega_0$. Moreover, C_{iklp} is the elasticity tensor.

Next, a reshaping was first performed to transforms the *M*x*M*x*M* third order tensor $\hat{\boldsymbol{K}}^{(2)}$ into a *M*xM^2 rectangular array $\tilde{\hat{\boldsymbol{K}}}^{(2)}$ and the *M*x*M*x*M*x*M* fourth order tensor $\boldsymbol{K}^{(3)}$ into a M^2xM^2 square matrix $\tilde{\boldsymbol{K}}^{(3)}$. These operations are achieved as follows:

$$\tilde{K}_{mJ}^{(2)} = \hat{K}_{mnp}^{(2)} \qquad \text{with} \qquad J=(n\text{-}1)M+p \tag{3.5}$$

and

$$\tilde{K}^{(3)}_{IJ} = K^{(3)}_{msnp} \qquad \text{with} \qquad I=(m\text{-}1)M+s \quad \text{and} \quad J=(n\text{-}1)M+p. \tag{3.6}$$

Construct next the expression

$$E_S = K^{(1)}_{mn}\, w_m\, w_n + 2\tilde{K}^{(2)}_{mJ}\, w_m\, v_J + 2\tilde{K}^{(3)}_{IJ}\, v_I\, v_J \tag{3.7}$$

where w_m and v_I are the components m and I of arbitrary vectors $\boldsymbol{w}$ and v. Then, from Eqs (3.1)-(3.4) one finds

$$\begin{aligned} E_S &= \int_{\Omega_0} \left\{ \left(w_m \frac{\partial U^{(m)}_i}{\partial X_k} \right) C_{iklp} \left(w_n \frac{\partial U^{(n)}_l}{\partial X_p} \right) + 2 \left(w_m \frac{\partial U^{(m)}_i}{\partial X_j} \right) C_{ijkl} \left(v_J Z^{(J)}_{kl} \right) + \left(v_I Z^{(I)}_{jk} \right) C_{jklw} \left(v_J Z^{(J)}_{lw} \right) \right\} d\boldsymbol{X} \\ &= \int_{\Omega_0} \left(w_m \frac{\partial U^{(m)}_i}{\partial X_j} + v_I Z^{(I)}_{ij} \right) C_{ijkl} \left(w_n \frac{\partial U^{(n)}_k}{\partial X_l} + v_J Z^{(J)}_{kl} \right) d\boldsymbol{X} = \int_{\Omega_0} B_{ij}\, C_{ijkl}\, B_{kl}\, d\boldsymbol{X} \end{aligned} \tag{3.8}$$

where for notational convenience

$$Z^{(J)}_{kl} = \frac{\partial U^{(n)}_r}{\partial X_k} \frac{\partial U^{(p)}_r}{\partial X_l} \qquad \text{and} \qquad B_{ij} = w_m \frac{\partial U^{(m)}_i}{\partial X_j} + v_I Z^{(I)}_{ij} \tag{3.9}$$

Since the elasticity tensor C_{iklp} is positive definite, it is seen from the last equality of Eq. (3.8) that E_S is positive for any vectors $\boldsymbol{w}$ and v. Rewriting this quantity as

$$E_S = \begin{bmatrix} \boldsymbol{w}^T & \boldsymbol{v}^T \end{bmatrix} \begin{bmatrix} \boldsymbol{K}^{(1)} & \tilde{\boldsymbol{K}}^{(2)} \\ \tilde{\boldsymbol{K}}^{(2)T} & 2\tilde{\boldsymbol{K}}^{(3)} \end{bmatrix} \begin{bmatrix} \boldsymbol{w} \\ \boldsymbol{v} \end{bmatrix} \tag{3.10}$$

it is seen that the PxP ($P = M + M^2$) symmetric matrix $\boldsymbol{K}_B$ defined as

$$\boldsymbol{K}_B = \begin{bmatrix} \boldsymbol{K}^{(1)} & \tilde{\boldsymbol{K}}^{(2)} \\ \tilde{\boldsymbol{K}}^{(2)T} & 2\tilde{\boldsymbol{K}}^{(3)} \end{bmatrix} \tag{3.11}$$

is positive definite.

To extend this discussion to include the structural-thermal coupling terms $K_{ijl}^{(th)}$, and $F_{il}^{(th)}$, note first that these parameters can be expressed as (Perez et al 2011).

$$K_{mnp}^{(th)} = \int_{\Omega_0} \frac{\partial U_i^{(m)}}{\partial X_k} \frac{\partial U_i^{(n)}}{\partial X_j} C_{jklr}\, \alpha_{lr}\, T^{(p)}\, d\boldsymbol{X} \tag{3.12}$$

and

$$F_{mn}^{(th)} = \int_{\Omega_0} \frac{\partial U_i^{(m)}}{\partial X_k} C_{iklr}\, \alpha_{lr}\, T^{(n)}\, d\boldsymbol{X} \,. \tag{3.13}$$

which are of the same form as Eqs (3.1)-(3.4) but involve the strain term $\alpha_{lr}\, T^{(n)}$ where $\boldsymbol{\alpha}$ is the coefficient of thermal expansion tensor and $T^{(n)}(\boldsymbol{X})$ is the *n*th basis function for the temperature in the continuous domain $\boldsymbol{X} \in \Omega_0$.

Next, proceed in reverse of Eqs (3.7)-(3.8) and define

$$E_C = \int_{\Omega_0} \left(w_m \frac{\partial U_i^{(m)}}{\partial X_j} + v_I\, Z_{ij}^{(I)} + z_m\, \alpha_{ij}\, T^{(m)} \right) C_{ijkl} \left(w_n \frac{\partial U_k^{(n)}}{\partial X_l} + v_J\, Z_{kl}^{(J)} + z_n\, \alpha_{kl}\, T^{(n)} \right) d\boldsymbol{X} \tag{3.14}$$

which is positive for all w_m, v_I, and z_m. Expanding the products in the integrand leads to

$$E_C = \begin{bmatrix} \boldsymbol{w}^T & \boldsymbol{v}^T & \boldsymbol{z}^T \end{bmatrix} \begin{bmatrix} \boldsymbol{K}^{(1)} & \tilde{\boldsymbol{K}}^{(2)} & \boldsymbol{F}^{(th)} \\ \tilde{\boldsymbol{K}}^{(2)T} & 2\tilde{\boldsymbol{K}}^{(3)} & \tilde{\boldsymbol{K}}^{(th)} \\ \boldsymbol{F}^{(th)T} & \tilde{\boldsymbol{K}}^{(th)T} & \boldsymbol{K}^{(tt)} \end{bmatrix} \begin{bmatrix} \boldsymbol{w} \\ \boldsymbol{v} \\ \boldsymbol{z} \end{bmatrix} \tag{3.15}$$

where $\tilde{\boldsymbol{K}}^{(th)}$ is the $M^2 \text{x} \mu$ rectangular array obtained by reshaping the third order tensor $\boldsymbol{K}^{(th)}$ according to

$$\tilde{K}_{Ip}^{(th)} = \hat{K}_{ijp}^{(th)} \qquad \text{with} \qquad I=(i\text{-}1)M+j \tag{3.16}$$

and $\boldsymbol{K}^{(tt)}$ is the μxμ symmetric, positive definite matrix of components

$$K_{mn}^{(tt)} = \int_{\Omega_0} \alpha_{jk}\, T^{(m)}\, C_{jklr}\, \alpha_{lr}\, T^{(n)}\, d\boldsymbol{X} \,. \tag{3.17}$$

Since the expression E_C of Eq. (3.14) is positive for all w_m, v_I, and z_m, it is concluded that the QxQ ($Q = M + \mu + M^2$) symmetric matrix $\boldsymbol{K}_C$

$$\boldsymbol{K}_C = \begin{bmatrix} \boldsymbol{K}^{(1)} & \tilde{\boldsymbol{K}}^{(2)} & \boldsymbol{F}^{(th)} \\ \tilde{\boldsymbol{K}}^{(2)T} & 2\tilde{\boldsymbol{K}}^{(3)} & \tilde{\boldsymbol{K}}^{(th)} \\ \boldsymbol{F}^{(th)T} & \tilde{\boldsymbol{K}}^{(th)T} & \boldsymbol{K}^{(tt)} \end{bmatrix} \tag{3.18}$$

is positive definite.

The above property provides a clear path for the simulation of parameters $K_{ij}^{(1)}$, $K_{ijl}^{(2)}$, $K_{ijlp}^{(3)}$, $K_{ijl}^{(th)}$, and $F_{il}^{(th)}$ within the maximum entropy nonparametric approach. Specifically, form first the matrix $\overline{\boldsymbol{K}}_C$ of the mean model from the parameters $K_{ij}^{(1)}$, $K_{ijl}^{(2)}$, $K_{ijlp}^{(3)}$, $K_{ijl}^{(th)}$, $F_{il}^{(th)}$, and $K_{mn}^{(tt)}$ of the finite element model of the mean structure. Then, proceed with the simulation of random matrices $\boldsymbol{K}_C$ according to Eqs (1.1)-(1.4) and Fig. 1.1, i.e.,

$$\overline{\boldsymbol{K}}_C = \overline{\boldsymbol{L}}_{\boldsymbol{K}}\, \overline{\boldsymbol{L}}_{\boldsymbol{K}}^T \qquad \text{and} \qquad \boldsymbol{K}_C = \overline{\boldsymbol{L}}_{\boldsymbol{K}}\, \boldsymbol{H}_{\boldsymbol{K}}\, \boldsymbol{H}_{\boldsymbol{K}}^T\, \overline{\boldsymbol{L}}_{\boldsymbol{K}}^T \tag{3.19), (3.20}$$

where (assuming a Cholesky decomposition of $\overline{\boldsymbol{K}}_C$)

$$\bar{\boldsymbol{L}}_{\boldsymbol{K}} = \begin{pmatrix} \bar{\boldsymbol{L}}_{SS}^{(1)} & \mathbf{0} & \mathbf{0} \\ \bar{\boldsymbol{L}}_{SS}^{(2)} & \bar{\boldsymbol{L}}_{SS}^{(3)} & \mathbf{0} \\ \bar{\boldsymbol{L}}_{TS}^{(1)} & \bar{\boldsymbol{L}}_{TS}^{(2)} & \bar{\boldsymbol{L}}_{TT} \end{pmatrix} \quad \text{and} \quad \boldsymbol{H}_{\boldsymbol{K}} = \begin{pmatrix} \boldsymbol{H}_{SS}^{(1)} & \mathbf{0} & \mathbf{0} \\ \boldsymbol{H}_{SS}^{(2)} & \boldsymbol{H}_{SS}^{(3)} & \mathbf{0} \\ \boldsymbol{H}_{TS}^{(1)} & \boldsymbol{H}_{TS}^{(2)} & \boldsymbol{H}_{TT} \end{pmatrix} \quad (3.21), (3.22)$$

where the subscripts *S* and *T* refer to the structural and thermal part of the model.

Finally, decompose the random matrices $\boldsymbol{K}_C$ of Eq. (3.20) according to the partition of Eq. (3.18) and identify the random parameters $K_{ij}^{(1)}$, $K_{ijl}^{(2)}$, $K_{ijlp}^{(3)}$, $K_{ijl}^{(th)}$, and $F_{il}^{(th)}$. It is interesting to note in the above format that the simulation of the thermal-structural coupling properties $K_{ijl}^{(th)}$ and $F_{il}^{(th)}$ is achieved in conjunction with the structural only model but independently of the thermal properties, e.g., capacitance, conductance.

While the above developments assumed that the elasticity tensor and thermal expansion were independent of temperatures, linear variations of these properties can also be considered in a deterministic ROM formulation, see (Matney et al 2011), and in an uncertain one, see Appendix A for the extension of Eqs (1.7), (3.11)-(3.18) to the case of the thermal expansion varying with temperature as an example of the process.

3.3. Implementation Challenges

The above process seems clear and well defined but after a closer inspection and trials, three key challenges were encountered. They are described below separately and their solutions briefly discussed, see Appendices B and C for details.

3.3.1. Identified Coefficients vs. Symmetric Coefficients

It should first be recognized that a series of terms in Eq. (1.7) involve the same monomials of the generalized coordinates, e.g. $K_{ijl}^{(2)}$ and $K_{ilj}^{(2)}$, and thus these terms may naturally be regrouped leading to the ROM governing equations

$$M_{ij}\ddot{q}_j + D_{ij}\dot{q}_j + \left[K_{ij}^{(1)} + K_{ijl}^{(th)}\,\tau_l \right] q_j + \bar{K}_{ijl}^{(2)} q_j q_l + \bar{K}_{ijlp}^{(3)} q_j q_l q_p = F_i + F_{il}^{(th)}\,\tau_l \,. \quad (3.23)$$

This equation is very similar to Eq. (1.7) except that there is no repetition in the monomials because $\bar{K}_{ijl}^{(2)}$ and $\bar{K}_{ijlp}^{(3)}$ are nonzero only for $j \le l$ and $j \le l \le p$. Note further that the identification methods discussed in (Perez et al 2011), (Matney et al 2011), (Kim et al 2013), (Mignolet et al 2013) and (Perez et al 2014) yield the coefficients $\bar{K}_{ijl}^{(2)}$ and $\bar{K}_{ijlp}^{(3)}$ not $K_{ijl}^{(2)}$ and $K_{ijlp}^{(3)}$ but it is these latter ones which are necessary in Eq. (3.18). Accordingly, an intermediate step in the simulation process is to transform one set of quadratic and cubic coefficients ($\bar{K}_{ijl}^{(2)}$ and $\bar{K}_{ijlp}^{(3)}$, referred to as "identified") into another ($K_{ijl}^{(2)}$ and $K_{ijlp}^{(3)}$, referred to as "symmetric"). To this end, comparing Eqs. (1.7) and (3.23) it is found that

$$\bar{K}_{mnl}^{(2)} = \begin{cases} 0 & \text{for } l < n \\ K_{mnn}^{(2)} & \text{for } l = n \\ K_{mnl}^{(2)} + K_{mln}^{(2)} & \text{for } l > n \end{cases} \quad (3.24a)$$

$$\bar{K}^{(3)}_{mnlp} = \begin{cases} 0 & \text{unless } p \geq l \geq n \\ K^{(3)}_{mnnn} & \text{for } p = l = n \\ K^{(3)}_{mnll} + K^{(3)}_{mlnl} + K^{(3)}_{mlln} & \text{for } p = l > n \\ K^{(3)}_{mpll} + K^{(3)}_{mlpl} + K^{(3)}_{mllp} & \text{for } p > l = n \\ 2K^{(3)}_{mnlp} + 2K^{(3)}_{mpln} + 2K^{(3)}_{mlpn} & \text{for } p > l > n \end{cases} \tag{3.24b}$$

Moreover, as discussed in (Mignolet and Soize 2008), the symmetry properties of the elasticity tensor and the form of Eqs (3.3) and (3.4) also imply that

$$\hat{K}^{(2)}_{ijl} = \hat{K}^{(2)}_{ilj} \tag{3.25}$$

and

$$K^{(3)}_{mnlp} = K^{(3)}_{nmlp} = K^{(3)}_{mnpl} = K^{(3)}_{lpmn} \tag{3.26}$$

Unfortunately, Eqs (3.24) and (3.25) are not sufficient to yield a unique set of values of $K^{(2)}_{ijl}$ and $K^{(3)}_{ijlp}$ from given values of $\bar{K}^{(2)}_{ijl}$ and $\bar{K}^{(3)}_{ijlp}$ except for the one mode situation, i.e., all indices equal. The problem is further compounded by a similar issue in the transformation of the quadratic parameters $K^{(2)}_{ijl}$ to their related coefficients $\hat{K}^{(2)}_{ijl}$ using Eq. (3.2). It is thus not possible to uniquely map the identified coefficients $\bar{K}^{(2)}_{ijl}$ and $\bar{K}^{(3)}_{ijlp}$ to the corresponding blocks of the matrix $\boldsymbol{K}_C$.

This problem is not specific to the matrix $\boldsymbol{K}_C$, it is also encountered in the purely structural situation, i.e., when constructing the matrix $\boldsymbol{K}_B$, and it has recently been addressed (Wang et al 2018) based on the following observations:

(a) the decomposition of the identified coefficients $\bar{K}^{(2)}_{ijl}$ and $\bar{K}^{(3)}_{ijlp}$ into the parameters $\hat{K}^{(2)}_{ijl}$ and $K^{(3)}_{ijlp}$ should only be a function of the modes *i, j, l* and *i, j, l, p*, respectively.

(b) the decomposition should ensure that the matrix $\boldsymbol{K}_B$ corresponding to the *n* selected modes or any subset of these modes, is positive definite, or as close as possible to it.

Accordingly, it was proposed in (Wang et al 2018) to proceed in steps, resolving the indeterminacy on all distinct two-mode coefficients, i.e., $\hat{K}^{(2)}_{ijj}$, $\hat{K}^{(2)}_{iij}$, $\hat{K}^{(2)}_{jij}$, $\hat{K}^{(2)}_{jii}$, $K^{(3)}_{iiij}$, $K^{(3)}_{iijj}$, $K^{(3)}_{ijij}$, and $K^{(3)}_{ijjj}$, by enforcing that they satisfy Eqs (3.2) and (3.24) and lead to a maximum of the lowest eigenvalue of the matrix $\boldsymbol{K}_B$ corresponding to the two modes *i* and $j > i$.

Next, the indeterminacy on all distinct three-mode coefficients, i.e., $\hat{K}^{(2)}_{ijl}$, $\hat{K}^{(2)}_{jil}$, $\hat{K}^{(2)}_{lij}$, $K^{(3)}_{iilp}$, and $K^{(3)}_{ilip}$, was similarly resolved by enforcing that they satisfy Eqs (3.2) and (3.24) and lead to a maximum of the lowest eigenvalue of the matrix $\boldsymbol{K}_B$ corresponding to the three modes $p > l > j > i$.

Finally, the indeterminacy on all distinct four-mode coefficients, i.e., $K^{(3)}_{ijlp}$, $K^{(3)}_{iljp}$, and $K^{(3)}_{ipjl}$, was again resolved by enforcing that they satisfy Eqs (3.2) and (3.24) and lead to a maximum of the lowest eigenvalue of the matrix $\boldsymbol{K}_B$ corresponding to the four modes *i* and $j > i$ and $l > j > i$.

3.3.2. Lack of Positive Definiteness of the Matrix $\boldsymbol{K}_B$

After the series of optimization efforts carried out in the previous section, it was found that the resulting matrix $\boldsymbol{K}_B$ may not be positive definite, see (Wang et al 2018) for justification and examples. In such cases, it was proposed that this matrix be modified to become positive definite. This modification was accomplished:

(a) without affecting the part of $\boldsymbol{K}_B$ that is positive definite, e.g., the linear stiffness matrix $\boldsymbol{K}^{(1)}$;

(b) inducing the smallest changes possible to this matrix.

The procedure proposed in (Wang et al 2018) is summarized here in Appendix B and its application to the matrix $\boldsymbol{K}_C$ discussed.

3.3.3. The Matrix $\boldsymbol{K}^{(tt)}$ Is Not Well Identifiable

An unusual feature of the matrix $\boldsymbol{K}_C$ is that it involves the matrix $\boldsymbol{K}^{(tt)}$ which does not appear in the reduced order model equations, Eqs (1.7) or (3.23), and thus its identification/selection requires further discussions.

At first, it was intended to identify the mean value of this matrix. An indirect approach was devised in which the terms $\alpha_{lr}\, T^{(n)}$ and $C_{jklr}\, \alpha_{lr}\, T^{(n)}$ were recognized as components *lr* and *jk* of the thermal only strain tensor $\boldsymbol{\varepsilon}_n^{(th)}$ and the corresponding stress tensor $\boldsymbol{\sigma}_n^{(th)}$ both induced by the thermal mode *n*. Then, the coefficient $K_{mn}^{(tt)}$ corresponds to the integral (summation over all nodes/elements) of the product $\boldsymbol{\varepsilon}_m^{(th)} : \boldsymbol{\sigma}_n^{(th)}$. It remained then to determine the thermal strain and stresses. This

was accomplished by applying temperature along mode *n* on the structure with all of its nodes restrained, the resulting stress distribution would then equal $\boldsymbol{\sigma}_n^{(th)}$ and the corresponding strains $\boldsymbol{\varepsilon}_n^{(th)}$ could then be obtained using the tensor of elasticity.

The implementation of this identification approach within Nastran was not successful, leading, even for very small reduced order models, to matrices $\boldsymbol{K}_C$ that were not positive definite. Accordingly, another strategy was devised. Specifically, since $\boldsymbol{K}^{(tt)}$ is only present in $\boldsymbol{K}_C$, not in Eqs (1.7) or (3.23), its determination is effectively part of the stochastic modeling effort. Then, its value being unclear, it was argued that $\boldsymbol{K}^{(tt)}$ should be determined by the entropy optimization effort. It is shown in Appendix C that this condition leads to $\bar{\boldsymbol{L}}_{TT}$, in Eq. (3.21), is equal to the identity matrix.

This result completes the determination of the lower triangular matrix $\bar{\boldsymbol{L}}_{\boldsymbol{K}}$, its structural only blocks $\bar{\boldsymbol{L}}_{SS}^{(1)}$, $\bar{\boldsymbol{L}}_{SS}^{(2)}$, and $\bar{\boldsymbol{L}}_{SS}^{(3)}$ are determined by the Cholesky decomposition of the positive definite $\boldsymbol{K}_B$ resulting of the sections 3.3.1 and 3.3.2 above. Moreover, from Eqs (3.18) and (3.19),

$$\bar{\boldsymbol{L}}_{TS}^{(1)} = \boldsymbol{F}^{(th)T}\left[\bar{\boldsymbol{L}}_{SS}^{(1)}\right]^{-T} \quad \text{and} \quad \bar{\boldsymbol{L}}_{TS}^{(2)} = \left[\tilde{\boldsymbol{K}}^{(th)T} - \bar{\boldsymbol{L}}_{TS}^{(1)}\,\bar{\boldsymbol{L}}_{SS}^{(2)T}\right]\left[\bar{\boldsymbol{L}}_{SS}^{(3)}\right]^{-T}. \quad (3.27), (3.28)$$

3.4. Implementation of Separate Uncertainty Levels

The matrix $\boldsymbol{K}_C$ involves two different properties of the structure: its elasticity tensor and its coefficient of thermal expansion the level of variability of which may be different. This situation is similar to the maximum entropy modeling of uncertainties that satisfy and violate certain symmetries, see (Murthy et al 2014) for a rotordynamic

application and (Matney et al 2011) for an implementation focused on material properties. In these investigations, it was proposed to *compound* the effects, i.e., $\boldsymbol{H}$ matrices, induced by both types of uncertainties.

In the present context, the compounding of the uncertainties in the elasticity and thermal expansion tensors can be achieved by expressing $\boldsymbol{H}_{\boldsymbol{K}}$ as

$$\boldsymbol{H}_{\boldsymbol{K}} = \boldsymbol{H}_T \, \boldsymbol{H}_S \tag{3.29}$$

where

$$\boldsymbol{H}_T = \begin{pmatrix} \boldsymbol{I} & \boldsymbol{0} & \boldsymbol{0} \\ \boldsymbol{0} & \boldsymbol{I} & \boldsymbol{0} \\ \boldsymbol{H}_{TS}^{(1)} & \boldsymbol{H}_{TS}^{(2)} & * \end{pmatrix} \quad \text{and} \quad \boldsymbol{H}_S = \begin{pmatrix} \boldsymbol{H}_{SS}^{(1)} & \boldsymbol{0} & \boldsymbol{0} \\ \boldsymbol{H}_{SS}^{(2)} & \boldsymbol{H}_{SS}^{(3)} & \boldsymbol{0} \\ \boldsymbol{0} & \boldsymbol{0} & \boldsymbol{I} \end{pmatrix}. \tag{3.30), (3.31}$$

In the above equations, $\boldsymbol{I}$ denotes the identity matrix of appropriate dimensions and the * designates a matrix partition which is irrelevant as it does not arise further in the computations, affecting only the matrix $\boldsymbol{K}^{(tt)}$ of the random structures. Rewriting Eq. (3.20) with (3.29) yields

$$\boldsymbol{K}_C = \bar{\boldsymbol{L}}_{\boldsymbol{K}} \, \boldsymbol{H}_T \, \boldsymbol{H}_S \, \boldsymbol{H}_S^T \, \boldsymbol{H}_T^T \, \bar{\boldsymbol{L}}_{\boldsymbol{K}}^T = \left(\bar{\boldsymbol{L}}_{\boldsymbol{K}} \, \boldsymbol{H}_T \right) \boldsymbol{H}_S \, \boldsymbol{H}_S^T \left(\bar{\boldsymbol{L}}_{\boldsymbol{K}} \, \boldsymbol{H}_T \right)^T \tag{3.32}$$

it is seen that the randomization of the structural properties is a two-step process. First, is the randomization by $\boldsymbol{H}_T$ transforming the mean model matrix $\bar{\boldsymbol{K}}_C$ into the random one

$$\boldsymbol{K}_C = \bar{\boldsymbol{L}}_{\boldsymbol{K}} \, \boldsymbol{H}_T \, \boldsymbol{H}_T^T \, \bar{\boldsymbol{L}}_{\boldsymbol{K}}^T = \left(\bar{\boldsymbol{L}}_{\boldsymbol{K}} \, \boldsymbol{H}_T \right) \left(\bar{\boldsymbol{L}}_{\boldsymbol{K}} \, \boldsymbol{H}_T \right)^T \tag{3.33}$$

which serves as a mean model for the further randomization by $\boldsymbol{H}_S$.

Note in the above process that the random matrix $\boldsymbol{H}_T$ only affects the *ST* blocks of $\boldsymbol{K}_C$, i.e., $K_{ijl}^{(th)}$ and $F_{il}^{(th)}$, and thus it models the uncertainty associated with the thermal expansion which is present only in those terms. On the contrary, the components of the random matrix $\boldsymbol{H}_S$ will affect all blocks of the $\boldsymbol{K}_C$ matrix and thus is appropriate for the modeling of the uncertainty in the elasticity tensor which is present in all elements of $\boldsymbol{K}_C$.

The selection of blocks of the $\boldsymbol{H}_S$ and $\boldsymbol{H}_T$ matrices as the identity or the zero matrix does not conform with the discussion of Eqs (1.1) – (1.4) and Fig. 1.1 but it is consistent with the extended nonparametric formulation developed in (Mignolet and Soize 2008) in which the uncertainty associated with the corresponding eigenvalues is set to zero while no constraint is imposed on the variability of the other eigenvalues. Accordingly, the block $\boldsymbol{H}_{TS}^{(1)}$ and $\boldsymbol{H}_{TS}^{(2)}$ are simulated as off-diagonal elements of the matrix $\boldsymbol{H}$ of Fig. 1.1, i.e., as independent identically distributed zero mean Gaussian random variables with standard deviation σ related to a uncertainty level δ_T. Finally, the 2x2 top left block of $\boldsymbol{H}_S$ is simulated as in Eqs (1.1) – (1.4) and Fig. 1.1 with the appropriate matrix size, i.e., $M + M^2$, and uncertainty level δ_S.

3.5. Example of Application – Straight Beam

3.5.1. Mean Model

The panel of (Matney et al 2011) was considered to demonstrate the application of the above uncertainty modeling strategies and provide a first assessment of the effects of

on the structural-thermal response uncertainty on the thermal properties and/or on the coefficient of thermal expansion.

Following (Matney et al 2011), the panel was modeled as an isotropic clamped-clamped beam with properties given in Table 3.1 and was modeled by finite elements in MSC.Nastran. The structural model consisted of 40 CBEAM elements while the thermal one involved 40 CQUAD4 elements along the beam and 6 through thickness.

Table 3.1. Clamped-Clamped Beam Mean Properties

Beam Length (L)	0.2286 m
Cross-section Width (w)	0.0127 m
Cross-section Thickness (h)	$7.88\ 10^{-4}$ m
Density	2700 kg/m^3
Young's Modulus	73,000 MPa
Shear Modulus	27,730 MPa
Coeff. Thermal Expansion	$2.5\ 10^{-5}$ /°C
Mesh (CBEAM)	40

The beam was subjected to a triangular flux of width $2\Delta=0.4\ L$, see Fig. 3.1, oscillating about the middle of the beam ($a_0 = L/2$) with a frequency Ω and an amplitude $\delta=0.075\ L$. The peak heat flux was selected so that the peak temperature on the upper surface of the beam would be 10°C for the steady problem ($\Omega = 0$) while the bottom surface was maintained at 0°C. The ends of the beam were also maintained at 0°C. This thermal loading led to a tip static deflection of 0.65 thickness and thus to a nonlinear geometric behavior.

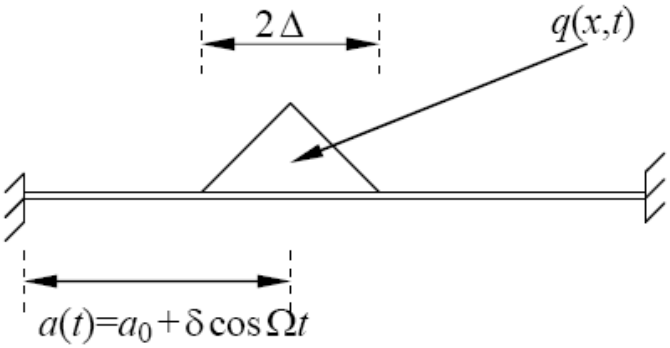

Figure 3.1. Beam Panel Subjected to an Oscillating Shock.

A reduced order model of the panel was constructed using 17 structural modes and 12 thermal basis functions, see ((Matney et al 2011) for details, which led to an excellent prediction of the full Nastran results. Of particular interest here is the peak response vs. frequency Ω which displays a peak for Ω approximately equal to 1/2 of the first linear natural frequency of the beam, see Fig. 3.2.

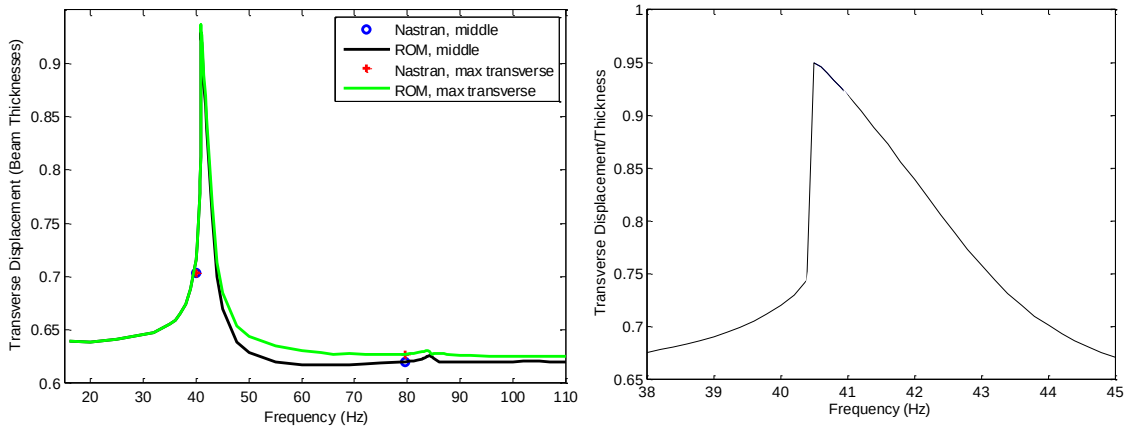

Figure 3.2. Maximum Transverse Deflection on the Beam and at the Beam Middle as a Function of the Flux Oscillation Frequency Ω as Determined from the ROM and Nastran Computations.

3.5.2. Uncertainty Modeling and Analysis

The consideration of uncertainty on the conductance properties was first carried out. In selecting the simulation strategy, Eqs. (1.1) – (1.4) or Eqs. (2.11) – (2.14), it was first noted in the results presented in (Matney et al 2011) that the temperature distribution rapidly decayed to zero away from the zone heated by the triangular flux. This observation suggested that the temperature distribution exhibited a localized behavior. To confirm this expectation, a concentrated flux was applied to the beam and the resulting steady temperature was determined using a full finite element analysis, see Fig. 3.3(a). It is clearly seen that the temperature is strongly localized. In fact, this behavior results from the fixed temperature boundary condition on the bottom. If this condition was replaced by an adiabatic one, the temperature distribution would be the one shown in Fig. 3.3(b) which is extended to the entire panel, i.e., exhibits a global behavior.

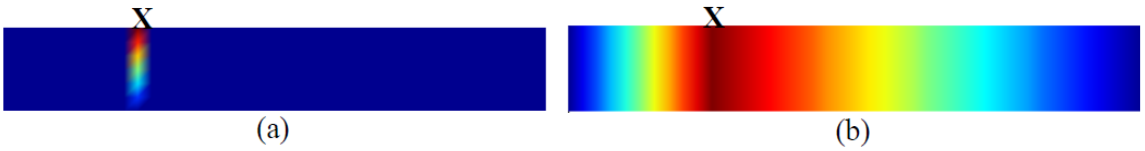

Figure 3.3. Distribution of Temperature in a Beam Due to a Single Heat Flux at the Location Marked by X. (a) Adiabatic Boundary Condition on Beam Top but Zero Temperature on Bottom. (b) Adiabatic Boundary Conditions Throughout.

The localized vs. global character of the temperature distribution can also be assessed from the eigenvalues of the conductance-capacitance problem as shown in Fig. 3.4. A localized character is associated with a series of close eigenvalues occurring at a nonzero value, see Fig. 3.4(a), while a global problem results when these values are spread in relative values. The existence of these two opposite behaviors for the mean model suggests that the uncertainty modeling strategy of the conductance and capacitance

matrices should similarly be able to induce mostly global or mostly local variations. On this basis, the maximum entropy approach for localized responses, Eqs (2.11) – (2.14), is proposed here to model these uncertain matrices regardless of the thermal boundary conditions.

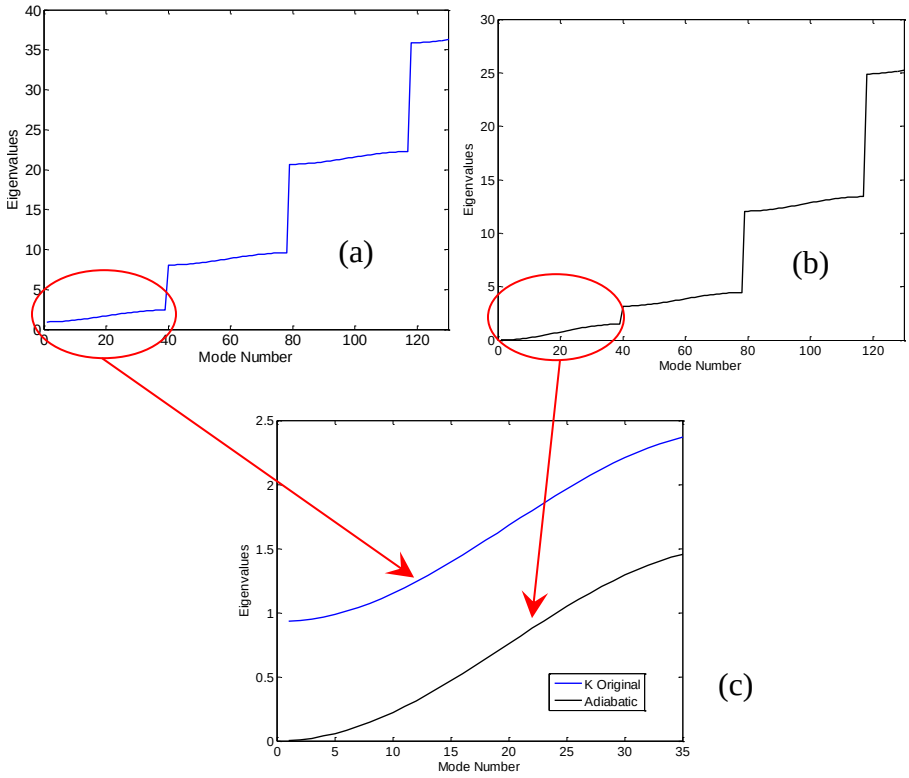

Figure 3.4. Comparisons of Eigenvalues of the Conductance-Capacitance Problem. (a) Case (a) of Fig. 3.3, (b) Case (b) of Fig. 3.3. (c) Comparison

Given the localized behavior of the current example problem (with the fixed temperature boundary conditions), see Fig. 3.3(a) or 3.4(a), it was expected that the uncertainty would mostly be introduced on the local component of the model, i.e., $\tilde{K}_L$. Nevertheless, the effects of introducing the uncertainty on $\tilde{K}_G$ and $\tilde{K}_L$ were separately assessed first then jointly. The overall uncertainty level was quantified as in (Soize 2012) by the dispersion parameter δ defined by Eq. (1.4).

Then, shown in Fig. 3.5 is the temperature distribution on the beam at a representative time induced by the oscillating flux. The yellow band represents the range of values between the 5th and 95th percentile of the temperature obtained at each node point for a value of δ=0.05 on the global component of the conductance matrix, $\tilde{K}_G$, and no uncertainty on its local counterpart, $\tilde{K}_L$. Note that the uncertainty band extends very far reaching the boundaries as expected from a global behavior. On the contrary, see Fig. 3.6 the temperature induced by a similar uncertainty in $\tilde{K}_L$ remains very localized to the middle of the beam where the flux is defined. Combining these two uncertainties leads to the results of Fig. 3.7 which exhibit broad band near the flux and only a very small band away from it as would be physically expected.

Having successfully produced random samples of the temperature distribution, it was next desired to propagate this uncertainty to the structural response. Each sample of the temperature was input to the structural ROM to determine the response over the range of oscillation frequencies Ω corresponding to the peak in Fig. 3.2(b). The resulting uncertainty band corresponding to the 5th-95th percentile was then evaluated for each frequency and is shown in Fig. 3.8. Note the broad range of frequencies over which the peak is observed and that the width of the (yellow) uncertainty band in the response at peak is wider than the one on the temperature, i.e., about ±10% of the mean value vs. ±5% in Fig. 3.7.

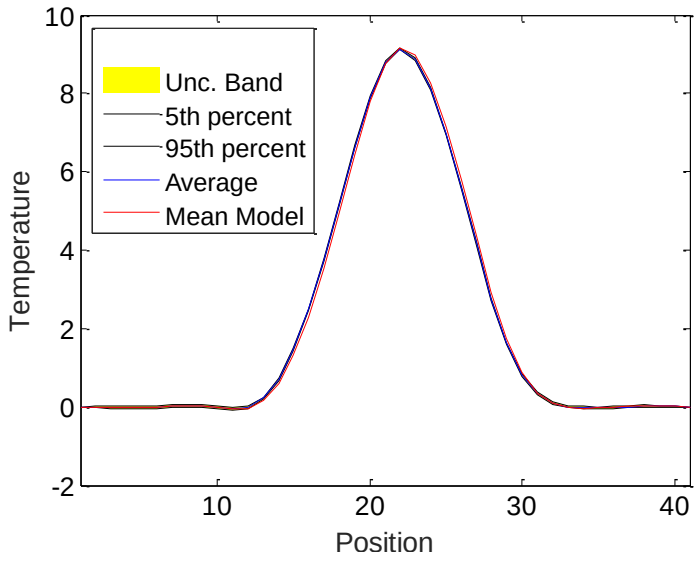

Figure 3.5. Uncertainty Band Induced by Introducing Uncertainty Only in the Global Component of the ROM Conductance Matrix. 40Hz Oscillating Triangular Heat Flux.

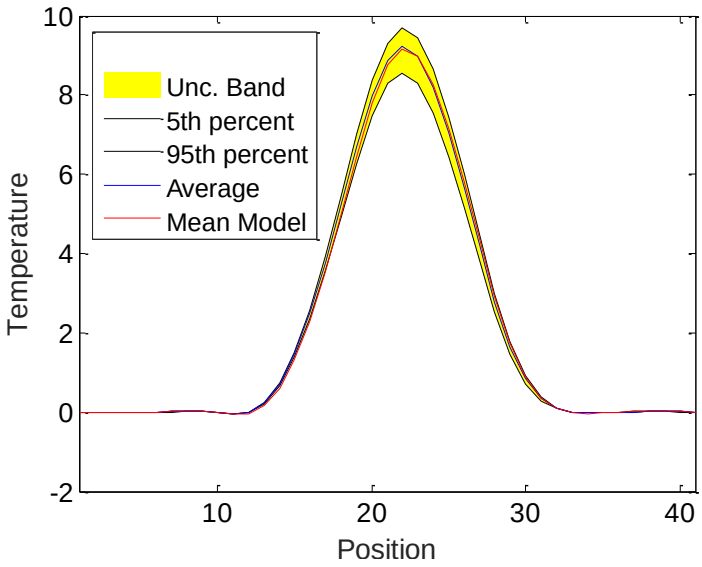

Figure 3.6. Uncertainty Band Induced by Introducing Uncertainty Only in the Local Component of the ROM Conductance Matrix. 40Hz Oscillating Triangular Heat Flux.

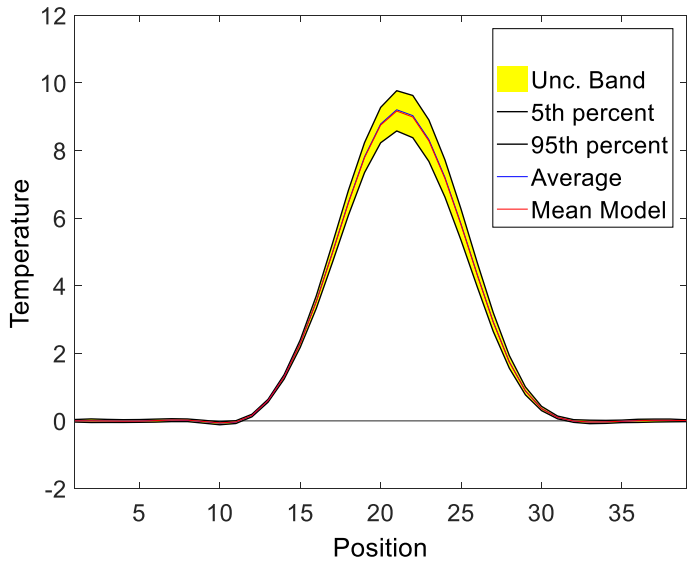

Figure 3.7. Uncertainty Band Induced by Introducing Uncertainty on Both Local and Global Components of the ROM Conductance Matrix. 40Hz Oscillating Triangular Heat Flux.

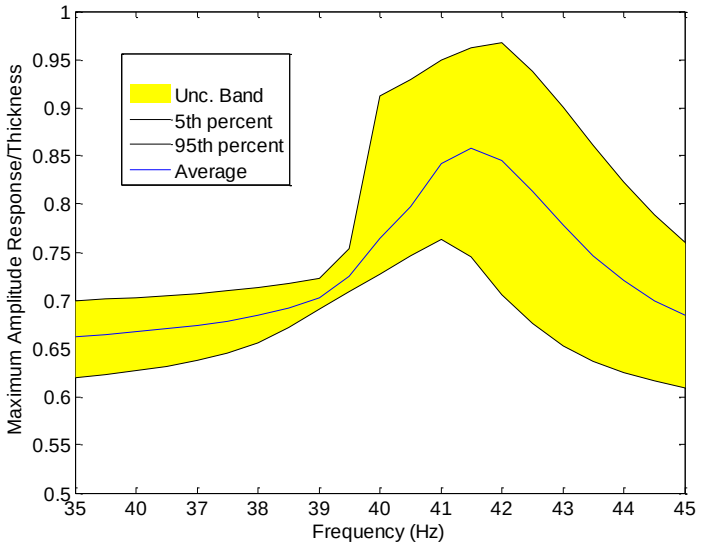

Figure 3.8. Uncertainty Band on Peak Structural Response as a Function of the Flux Oscillating Frequency. Uncertainty on Conductance.

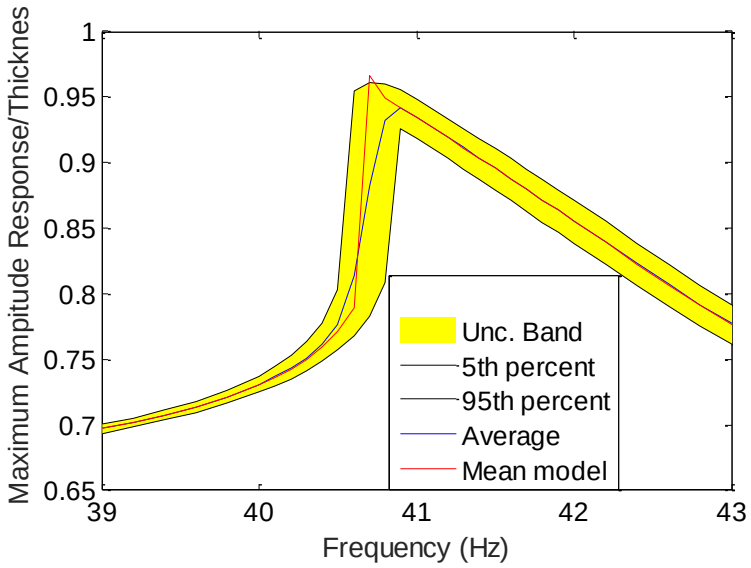

Figure 3.9. Uncertainty Band on Peak Structural Response as a Function of the Flux Oscillating Frequency. Uncertainty on Thermal-Structural Coupling Parameters.

Uncertainty in the structural model was next considered, first in the thermal expansion, i.e., on the thermal-structural coupling, was introduced first through the matrix $\boldsymbol{H}_T$ with $\boldsymbol{H}_S$ set to the identity matrix and proceeding with Eqs (B.12) and (B.13) to resolve the singularity of the matrix $\boldsymbol{K}_C$. Note that the matrix $\bar{\boldsymbol{K}}_{23}$ was not found to be a significant contributor to the mean response and thus Eq. (B.14) was not implemented. The uncertainty analysis was carried out with a value of $\delta = 10^{-4}$. This value seems very small, giving rise to coefficients of variation of 0.59% (l =1), 0.35% (l =3), 0.80% (l =5) on the parameters $K_{11l}^{(th)}$ and 0.56% (l =1), 3.05% (l =3), 7.84% (l =5) on $F_{1l}^{(th)}$ which are the key driving terms to the first and dominant structural mode. Then, shown in Fig. 3.9 is the uncertainty band and mean model prediction of the peak beam (transverse) response as a function of frequency. Note that the width of the band, ±2.5% of the mean value at the resonance, is significantly larger than the above coefficients of

variations of the parameters demonstrating a strong sensitivity of the response with respect to the coefficient of thermal expansion and thus the importance of carrying such uncertainty analyses.

The uncertainty on the structural part only was also considered and implemented through the matrix $\boldsymbol{H}_S$ with $\boldsymbol{H}_T$ set to the identity matrix. This effort was carried out with a value of $\delta = 0.02$ which corresponds to a coefficient of variation of the first natural frequency of 0.56%. Then, shown in Fig. 3.10 are the uncertainty band and mean model prediction of the peak beam (transverse) response as a function of frequency. Once again, it is seen that the uncertainty level on the response is much larger than it is for the model coefficients, confirming the sensitivity of the response. Finally, shown in Fig. 3.11 is uncertainty band induced by both structural and thermal expansion uncertainties. As expected, this band is wider than the ones seen in Figs. 3.9 and 3.10 and corresponding to each uncertainties separately.

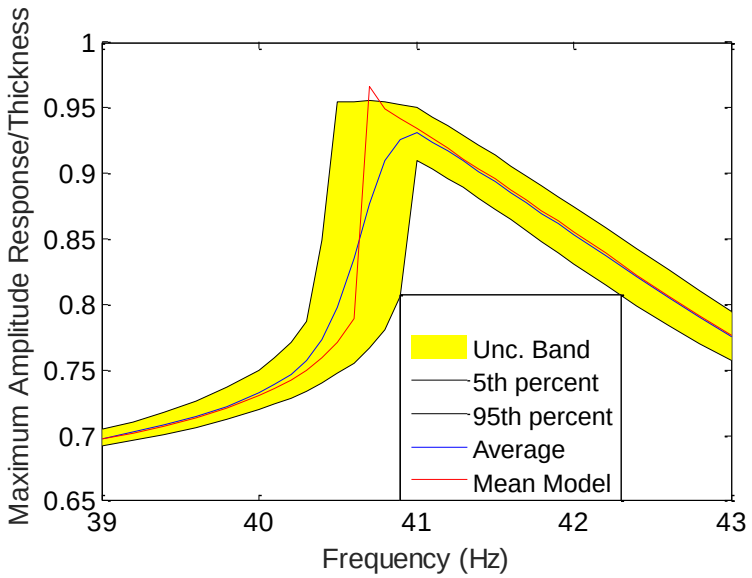

Figure 3.10. Uncertainty Band on Peak Structural (Transverse) Response as a Function of the Flux Oscillating Frequency. Uncertainty on Structural Parameters Only.

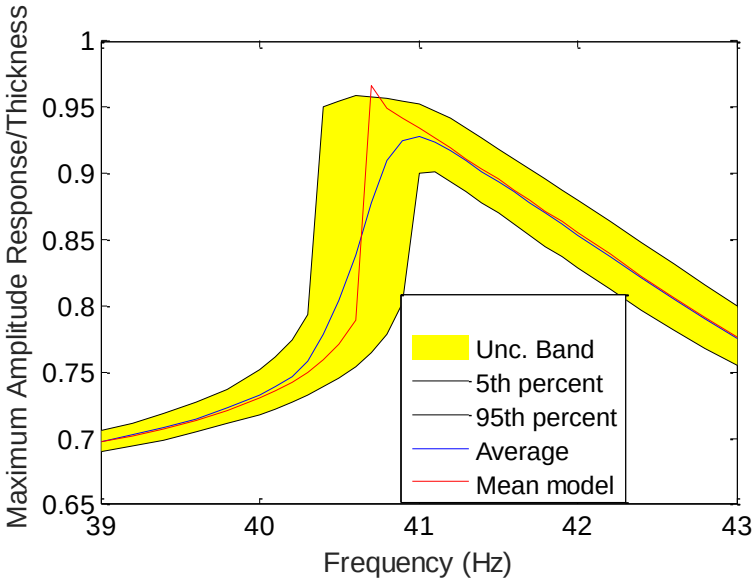

Figure 3.11. Uncertainty Band on Peak Structural (Transverse) Response as a Function of the Flux Oscillating Frequency. Uncertainty on Structural and Thermal-Structural Coupling Parameters.

3.6. Example of Application – Panel with Stiffeners

3.6.1. Mean Model

The second validation is on the panel with stiffeners as shown in Fig. 3.12 which was originally considered in (Culler and McNamara 2011) and is subjected to a trajectory spanning Mach 2 to Mach 12 in 300 seconds with fully coupled structural/thermal/aerodynamic computations. Full details of the panel properties are in (Culler and McNamara 2011) but some key features are:

(i) nonlinear geometric structural effects are considered,

(ii) the coefficient of thermal expansion is linearly dependent on temperature but the tensor of elasticity is not,

(iii) the heat conduction problem is solved on the undeformed configuration with capacitance and conductance properties varying with temperature,

(iv) the aerodynamic forces are determined from piston theory while the aerodynamic heat flux is estimated from Eckert reference enthalpy method,

(v) the structural problem is solved quasi statically while the heat conduction is marched through a time step;

(vi) the computations of the thermal problem and the structural one are staggered, marched with time step of 0.5s. The thermal solution at one time step is obtained first, from the thermal and structural fields at the previous time step. Then, the structural problem is solved using the current temperature distribution.

A structural-thermal ROM of this panel providing a close match of finite element results was developed in (Matney et al 2015) and shown in Fig. 3.13 is a comparison of the maximum transverse displacement and the temperature of the center of the panel predicted by the finite element model (Culler and McNamara 2011) and by the ROM (Matney et al 2015). In this ROM, the structural model included 44 structural basis functions, and the thermal model included 42 basis functions.

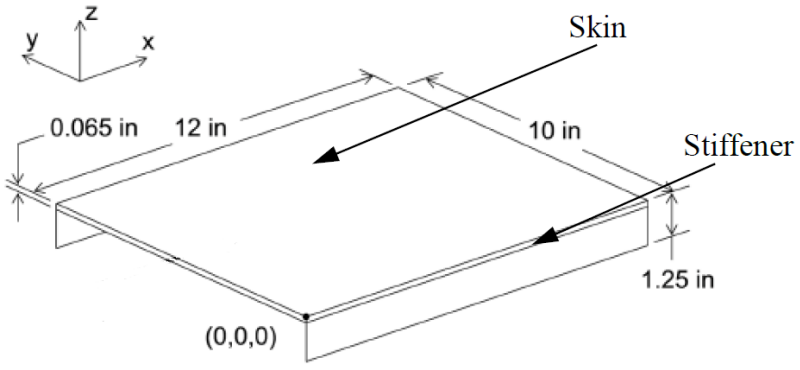

Figure 3.12. A Hypersonic Panel with Stiffener (Culler and McNamara 2011).

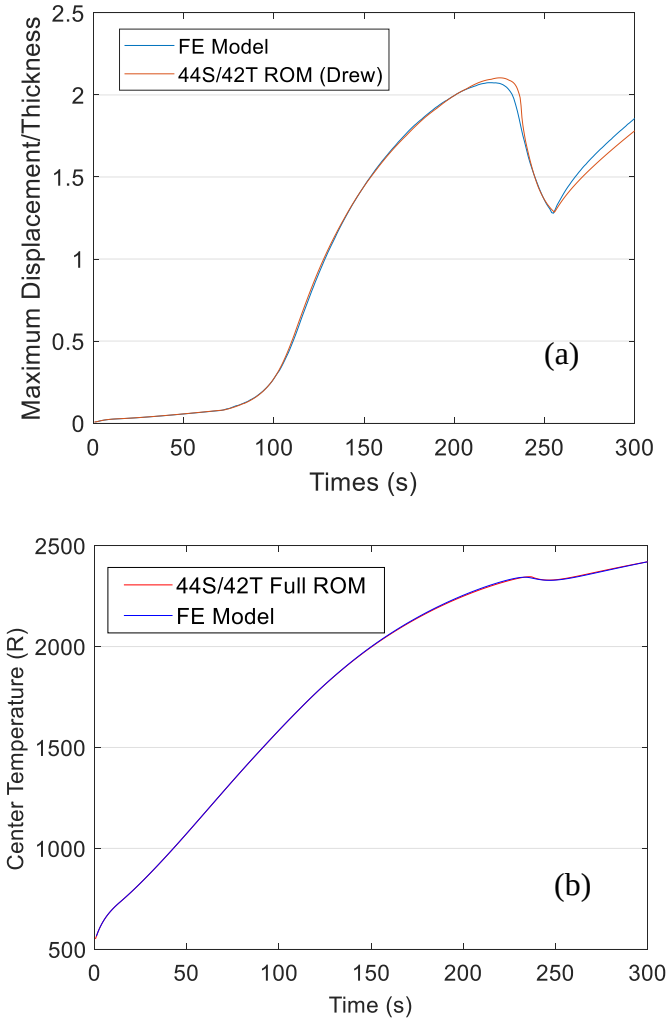

Figure 3.13. (a) Maximum Transverse Displacements and (b) Temperature of the Panel Center Over the Trajectory. Predictions by Finite Element Models (Culler and McNamara 2011) and Structural-Thermal Full ROM (Matney et al 2015).

3.6.2. Uncertainty Modeling and Analysis

Owing to the dependence of the coefficient of thermal expansion on the temperature, the introduction of uncertainty in the structural and structural-thermal properties was carried out on the $\boldsymbol{K}_D$ matrix of Appendix A and according to the discussion of Section 3.3.2 for the handling of the positive definiteness issues. In this problem, the block $\bar{\boldsymbol{K}}_{23}$ in Eq. (B.7) was found to be important in determining the mean response. Accordingly,

the uncertainty was introduced following Eqs (B.12)-(B.14) with levels δ_S and δ_T for $\boldsymbol{K}_{23}$ equal to those for $\boldsymbol{K}_{11}$ and $\boldsymbol{K}_{13}$.

Due to the issues described in (Wang et al 2018), the ROM coefficients identified from Nastran computations typically do not satisfy the basic symmetry properties derived in (Muravyov and Rizzi 2003) and (Mignolet and Soize 2008), such as $\bar{K}^{(3)}_{nnnm} = 3\bar{K}^{(3)}_{mnnn}$, see Eq. (3.24b). In (Wang et al 2018) and section 3.5.2 these conditions were enforced by symmetrization, see (Mignolet and Soize 2008). For the present ROM however, the symmetrization was found to affect the prediction of the mean model. Thus, to avoid this negative effect, a mapping was first established between symmetrized and non-symmetrized identified coefficients of the mean model. This mapping was then used in reverse to transform the random coefficients simulated on the basis of the symmetrized model to random coefficients relevant to the non-symmetrized ROM.

It is known from prior investigations of this panel that its behavior is very sensitive to small changes, e.g., visible differences were obtained with two different versions of Nastran, and thus the levels of uncertainty were selected small. Considering first structural uncertainty only (i.e., $\delta_T = 0$), δ_S was selected as 0.001. Then, the coefficient of variation of $\boldsymbol{K}^{(th)}_{111}$ and $\boldsymbol{K}^{(th)}_{1111}$ were found to be 0.37%, while those of $\boldsymbol{F}^{(th)}_{11}$ and $\boldsymbol{F}^{(th)}_{111}$ equaled 2.70%. Plotted in Figs. 3.14 – 3.15 are the 5 realizations and 10-90% uncertainty band of maximum displacements along with the mean model for the entire 300s trajectory. It is clear that the effect of uncertainty is increasing with increasing time and Mach number. It should also be noted that the drop in maximum response occurring

at about 230s for the mean model was not duplicated by two of the realizations shown suggesting that the change of dominant mode did not happen for that realization.

The effects of thermal uncertainty only (i.e., $\delta_S = 0$) were also considered with $\delta_T = 0.005$. This selection leads to coefficient of variation of $\boldsymbol{K}_{111}^{(th)}$ and $\boldsymbol{K}_{1111}^{(th)}$ about 0.00% and 0.00%, in $\boldsymbol{F}_{11}^{(th)}$ and $\boldsymbol{F}_{111}^{(th)}$ about 5.27% and 43.33%. Then, shown in Figs. 3.16 – 3.17 are the evolution of the maximum response on the panel for 5 samples and band showing again that the variability of the response is very prominent near the mode switching event.

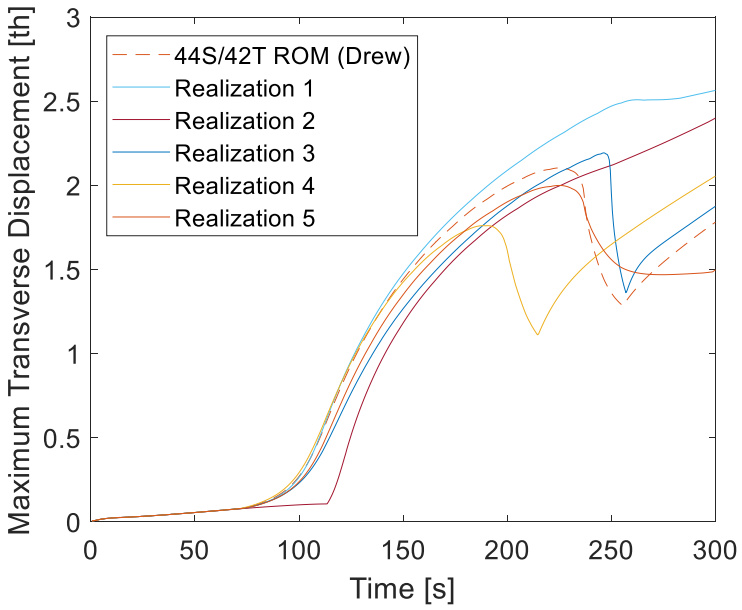

Figure 3.14. Maximum Displacement of the Panel Over 300s, 5 Realizations with $\delta_S = 0.001$ and $\delta_T = 0$, Along with the Mean Model.

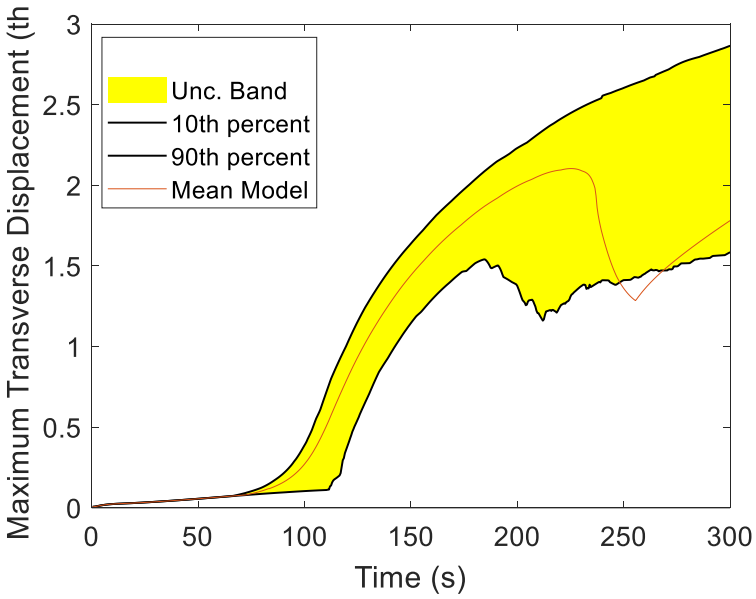

Figure 3.15. Maximum Displacement of the Panel Over 300s, 10 – 90% uncertainty band from 98 realizations with $\delta_S = 0.001$ and $\delta_T = 0$, Along with the Mean Model.

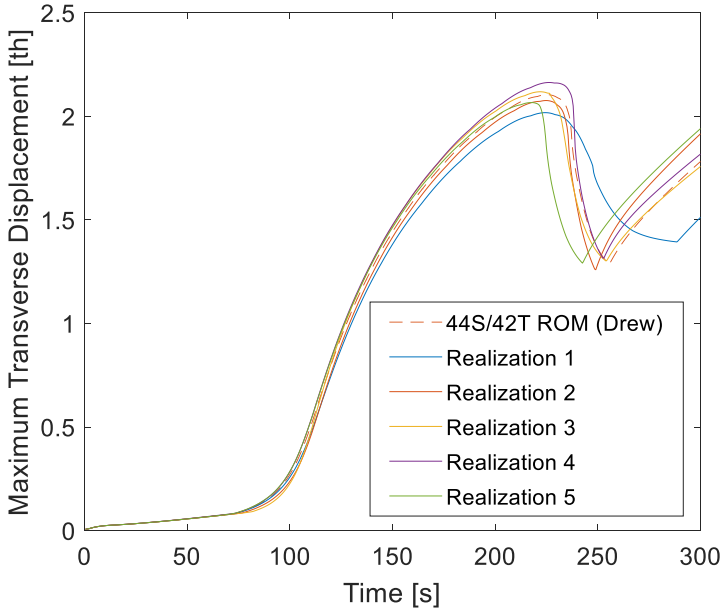

Figure 3.16. Maximum Displacement of the Panel Over 300s, 3 Realizations with $\delta_S = 0$ and $\delta_T = 0.005$, Along with the Mean Model.

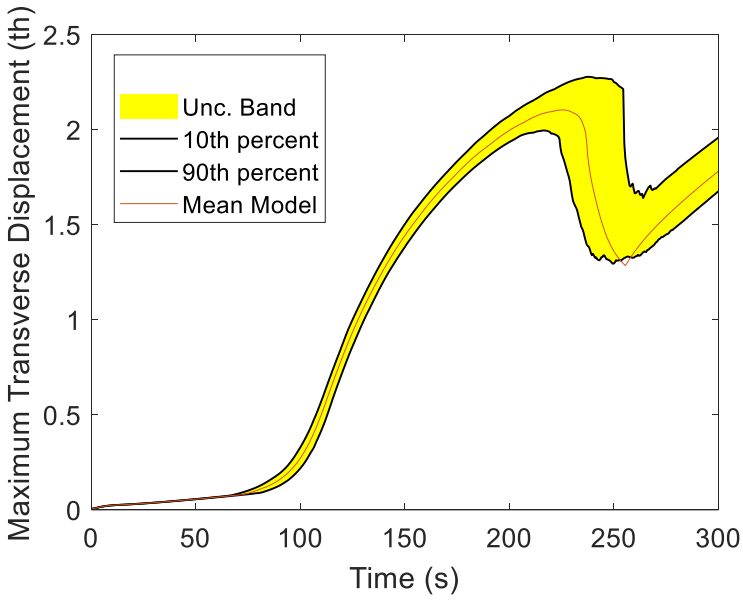

Figure 3.17. Maximum Displacement of the Panel Over 300s, 10 – 90% uncertainty band from 100 realizations with $\delta_S = 0$ and $\delta_T = 0.005$, Along with the Mean Model.

4. MAXIMUM ENTROPY STRUCTURAL-THERMAL UNCERTAINTY MODELING AT THE FINITE ELEMENT LEVEL

4.1. Introduction

A modification of the maximum entropy modeling approach was developed in Chapter 2 when the uncertain response is expected to exhibit a localized behavior. That modification was achieved by understanding the properties of the ROM matrices leading to a localization of the response and adapting the method to meet those properties. Another approach, however, would be to introduce the uncertainty in a more spatially localized manner to mitigate the globalization associated with the maximization of the entropy. It is such an approach which is proposed here, i.e., to introduce the uncertainty on each finite element matrix (mass, stiffness, conduction, etc.) following the maximum entropy concept and treating the corresponding matrix from the baseline model as a mean ROM. This approach represents a novel compromise between the modeling of uncertainty within the elements (e.g., by randomizing the elasticity tensor) on one end and at the level of a global ROM on the other. It brings some epistemic uncertainty not present in the former approach while retaining more local character than the latter one.

Validations of this approach to a heated structural problem is carried out below. It is moreover demonstrated that the approach can be used to model the uncertainty in the elasticity tensor and the coefficient of thermal expansion (CTE) to relate element/nodal strains and temperatures to their stress counterpart.

4.2. Single Physics Elemental Level Uncertainty Modeling

As described in the introduction, the focus of the present effort is on developing an uncertainty modeling strategy at the level of the finite element. To this end, denote by

$\overline{\boldsymbol{K}}$ an elemental matrix (stiffness, mass, conductance) of the baseline finite element. Next, assume that the only properties required for its uncertain counterpart $\boldsymbol{K}$ are that this matrix is positive definite, symmetric, and non-singular. Then, following the maximum entropy strategy, one can express

$$\boldsymbol{K} = \overline{\boldsymbol{L}}_{\boldsymbol{K}}\, \boldsymbol{H}_{\boldsymbol{K}}\, \boldsymbol{H}_{\boldsymbol{K}}^{T}\, \overline{\boldsymbol{L}}_{\boldsymbol{K}}^{T} \tag{4.1}$$

where $\overline{\boldsymbol{L}}_{\boldsymbol{K}}$ is a decomposition of $\overline{\boldsymbol{K}}$ satisfying

$$\overline{\boldsymbol{K}} = \overline{\boldsymbol{L}}_{\boldsymbol{K}}\, \overline{\boldsymbol{L}}_{\boldsymbol{K}}^{T} \tag{4.2}$$

and $\boldsymbol{H}_{\boldsymbol{K}}$ is a lower triangular matrix as defined in Fig. 1.1. The process could then be repeated for each element in turn.

In applying the above concepts, there are two key issues which must be carefully addressed. The first one is that *the matrices* $\boldsymbol{H}_{\boldsymbol{K}}$ *corresponding to different elements cannot be simulated independently of each other*. Doing so would induce very high spatial frequency variations which are unphysical. Rather, it is proposed here to adopt the matrix field modeling proposed in (Soize 2006) which views each element H_{ij} as the transformation of a zero mean, unit variance Gaussian field P_{ij} with a specified stationary autocorrelation function

$$R(\boldsymbol{y}) = E\left[P_{ij}(\boldsymbol{x})P_{ij}(\boldsymbol{x}')\right] \qquad \boldsymbol{y} = \boldsymbol{x}' - \boldsymbol{x} \tag{4.3}$$

where $\boldsymbol{x}$ and $\boldsymbol{x}'$ denote the coordinates of two elements (e.g., of their center). Specifically, for $i \neq j$

$$H_{ij} = \sigma P_{ij} \tag{4.4}$$

while for $i = j$

$$H_{ii} = F_{H_{ii}}^{-1}\left[F\left(P_{ij}\right)\right] \tag{4.5}$$

where F is the cumulative distribution function of the standard Gaussian random variable and $F_{H_{ii}}^{-1}$ is the inverse of the cumulative distribution function of the Gamma random variable H_{ii}, see Chapter 1.2 for detail.

The correlation between random elemental matrices of neighboring finite elements implied by the above algorithm must be reflected on every component of the *assembled* matrix. That is, if a strong correlation is expected between two different finite elements, then there must exist a similarly strong correlation between the components of their elemental matrices *which are added together in the construction of the global matrix*. Since the matrix $\boldsymbol{H_K}$ is built from the independent fields P_{ij}, this condition can be satisfied if:

(1) the elemental matrices of the mean and uncertain models are expressed in the *same* (i.e., global) frame of reference, and

(2) each simulated sample of the random global matrix is independent of the ordering of the nodes in each element.

This latter condition can be achieved as follows.

(i) Organize the mean elemental matrices $\overline{\boldsymbol{K}}$ consistently with the ordering of its degrees of freedom as: degree of freedom 1 for all nodes, degree of freedom 2 for all nodes, etc.

(ii) Adopt lower triangular (or block lower triangular) decompositions $\overline{\boldsymbol{L}}_{\boldsymbol{K}}$ to retain the same ordering of the degrees of freedom.

(iii) Restrict the random matrices $\boldsymbol{H_K}$ so that each of their samples is invariant with respect to a permutation of the ordering of the nodes. This is achieved here by expressing

$$\boldsymbol{H_K} = \boldsymbol{H} \otimes \boldsymbol{I_r} \tag{4.6}$$

where $\boldsymbol{H}$ is a *m*x*m* random matrix simulated as described in Eq. (4.3)-(4.5) where *m* is the number of degrees of freedom per node. Moreover, $\boldsymbol{I_r}$ denotes the *r*x*r* identity matrix where *r* is the number of nodes per element and $\otimes$ denotes the Kronecker product operation.

Once the elemental matrix (or matrices) have been simulated for each element, the finite element model is reassembled and the response can be determined. Proceeding with a series of such simulations provides a population of responses from which statistics can be determined.

4.3. Uncertainty on Heated Structures

It is next desired to extend the above formulation to heated structures in which there is uncertainty in both the structural and structural-thermal coupling (i.e., coefficient of thermal expansion) properties. The governing equations for a particular element can be written as

$$\boldsymbol{M}\ddot{\boldsymbol{x}} + \boldsymbol{K}\boldsymbol{x} = \boldsymbol{F}_{th}\,T + \boldsymbol{F}_{str} \tag{4.7}$$

where $\boldsymbol{M}$ is the element mass matrix, $\boldsymbol{K}$ the elemental isothermal stiffness matrix and $\boldsymbol{F}_{str}$ are applied static structural loads, assumed deterministic. Moreover, *T* is the temperature of the element and $\boldsymbol{F}_{th}$ is the vector of thermal "forces" at each node and each degree of freedom of the element. They are assumed here to be temperature

independent reflecting a similar property of the coefficient of thermal expansion (the extension to the case of a coefficient of thermal expansion linearly dependent on temperature is discussed in previous chapter). Finally, $\boldsymbol{x}$ is the vector of displacement degrees of freedom of the elements.

It is worthwhile to recognize, e.g., see Song et al (2017), that the vector $\boldsymbol{F}_{th}$ depends on both the coefficient of thermal expansion but also on the elasticity tensor of the element. Thus, a randomization of K to reflect uncertainties in this tensor cannot be done alone, it ought to include $\boldsymbol{F}_{th}$ as well. This point was instrumental in the discussion of (Song et al 2017) and led to the introduction of a matrix combining cold stiffness properties and thermal effects which was shown to be positive definite. Following this discussion but reduced to the linear case (nonlinear geometric effects were also included in (Song et al 2017)) demonstrates that the positive semi definite elemental matrix of interest is

$$\boldsymbol{K}_C = \begin{bmatrix} \boldsymbol{K} & \boldsymbol{F}_{th} \\ \boldsymbol{F}_{th}^T & \boldsymbol{K}_{TT} \end{bmatrix} \tag{4.8}$$

where $\boldsymbol{K}_{TT}$ is the elemental version of the matrix introduced in (Song et al 2017) which does not appear in Eq. (4.8), see below for discussion.

Based on this observation, it is concluded that the elemental modeling of heated structures desired here should be performed as in previous section on the matrix $\boldsymbol{K}_C$ of mean $\bar{\boldsymbol{K}}_C$ (an overbar is used consistently as before to denote matrices related to the mean model). To this end, note first that the structural degrees of freedom need to be reordered as described above. Then, let $\bar{\boldsymbol{L}}_C$ be a decomposition of $\bar{\boldsymbol{K}}_C$ satisfying

$$\bar{\boldsymbol{K}}_C = \bar{\boldsymbol{L}}_C \, \bar{\boldsymbol{L}}_C^T . \tag{4.9}$$

More specifically, assume here that $\bar{\boldsymbol{L}}_C$ is selected in the block triangular form

$$\bar{\boldsymbol{L}}_C = \begin{bmatrix} \bar{\boldsymbol{L}}_{\boldsymbol{K}} & 0 \\ \bar{\boldsymbol{L}}_{th} & \bar{\boldsymbol{L}}_{TT} \end{bmatrix} \tag{4.10}$$

Then, introducing Eq. (4.10) into Eq. (4.9), it is readily seen that $\bar{\boldsymbol{L}}_{\boldsymbol{K}}$ is defined as before, Eq. (4.2), and thus with the symmetry condition

$$\bar{\boldsymbol{L}}_{\boldsymbol{K}} = \bar{\boldsymbol{K}}^{1/2} \tag{4.11}$$

Next, from Eq. (4.9) and (4.10), the block $\bar{\boldsymbol{L}}_{th}$ should be determined to satisfy

$$\bar{\boldsymbol{L}}_{th} \, \bar{\boldsymbol{L}}_{\boldsymbol{K}}^T = \bar{\boldsymbol{F}}_{th}^T \tag{4.12}$$

In evaluating this block, two properties of the stiffness matrix $\bar{\boldsymbol{K}}$ and the thermal forces vector $\bar{\boldsymbol{F}}_{th}$ play a key role. Specifically,

(a) the matrix $\bar{\boldsymbol{K}}$ is only positive semi definite exhibiting the 6 rigid body modes as the element is free-free, and

(b) the application of the temperature does not induce any rigid body displacements.

Denoting by $\boldsymbol{\Phi}_{RB}$ the matrix formed by stacking in columns the 6 rigid body modes, the above two properties imply that

$$\bar{\boldsymbol{K}} \, \boldsymbol{\Phi}_{RB} = \boldsymbol{0} \quad \text{and} \quad \boldsymbol{\Phi}_{RB}^T \bar{\boldsymbol{F}}_{th} = \boldsymbol{0} . \tag{4.13), (4.14}$$

The singularity of $\bar{\boldsymbol{K}}$ and thus $\bar{\boldsymbol{L}}_{\boldsymbol{K}}$ (see Eq. (4.11)) prevents its inversion to determine $\bar{\boldsymbol{L}}_{th}$ directly from Eq. (4.12) but Eq. (4.13) guarantees that there are finite norm matrices $\bar{\boldsymbol{L}}_{th}$ satisfying Eq. (4.12). To proceed, let $\bar{\boldsymbol{\Phi}}_D$ be the matrix of the

normalized deformation (non-rigid) modes of $\bar{\boldsymbol{K}}$ stacked in columns and denote by $\bar{\boldsymbol{\Lambda}}_D$ the corresponding diagonal matrix of non-zero eigenvalues. Then, Eq. (4.13) implies that $\boldsymbol{F}_{th}$ can be expressed as

$$\bar{\boldsymbol{F}}_{th} = \bar{\boldsymbol{\Phi}}_D \, \bar{\boldsymbol{p}} \quad \text{with} \quad \bar{\boldsymbol{p}} = \bar{\boldsymbol{\Phi}}_D^T \, \bar{\boldsymbol{F}}_{th} \ . \tag{4.15), (4.16}$$

Moreover, to avoid the presence of the null space of $\bar{\boldsymbol{K}}$ in $\bar{\boldsymbol{L}}_{th}$, let

$$\bar{\boldsymbol{L}}_{th} = \bar{\boldsymbol{q}}^T \bar{\boldsymbol{\Phi}}_D^T . \tag{4.17}$$

Then, introducing Eq. (4.15) and (4.17) in Eq. (4.12) leads to

$$\bar{\boldsymbol{q}} = \bar{\boldsymbol{\Lambda}}_D^{-1/2} \, \bar{\boldsymbol{p}} . \tag{4.18}$$

To complete the decomposition of Eqs (4.9) and (4.10), it remains to obtain the block $\bar{\boldsymbol{L}}_{TT}$ which is in principle derived from the matrix $\bar{\boldsymbol{K}}_{TT}$. This matrix is difficult to estimate accurately non-intrusively from a commercial finite element code. Then, considering that it does not appear in the governing equations, Eq. (7), it has been proposed that it be selected to maximize the entropy of the simulated matrices $\boldsymbol{K}_C$. This is achieved (see Appendix C) when the block $\bar{\boldsymbol{L}}_{TT}$ is equal to the identity matrix which is assumed here in the sequel.

The randomization of the matrix $\boldsymbol{K}_C$ is then proposed as in Eq. (4.2), i.e.,

$$\boldsymbol{K}_C = \bar{\boldsymbol{L}}_C \, \boldsymbol{H}_C \, \boldsymbol{H}_C^T \, \bar{\boldsymbol{L}}_C^T \tag{4.19}$$

where $\boldsymbol{H}_C$ is the random block lower triangular matrix

$$\boldsymbol{H}_C = \begin{bmatrix} \boldsymbol{H}_K & \boldsymbol{0} \\ \boldsymbol{H}_{th} & \boldsymbol{H}_{TT} \end{bmatrix} \tag{4.20}$$

where $\boldsymbol{H_K}$ is the matrix of Eq. (4.6) and $\boldsymbol{H}_{th}$ and $\boldsymbol{H}_{TT}$ are novel random matrices of form to be derived.

In this context, note first from the lower triangular form of both $\bar{\boldsymbol{L}}_C$ and $\boldsymbol{H}_C$ that $\boldsymbol{H}_{TT}$ would only affect the $\boldsymbol{K}_{TT}$ block. Since this matrix does not appear in the governing equations, Eq. (4.7), its value is irrelevant and thus $\boldsymbol{H}_{TT}$ needs not be computed nor discussed. It will be symbolically replaced by a ***** in the sequel to emphasize this fact.

Next, note that the matrix $\boldsymbol{K}_C$ involves two different properties of the structure: its elasticity tensor and its coefficient of thermal expansion, the level of variability of which may be different. To reflect these two variabilities, it is proposed here, as in Chapter 2 and (Song et al 2017), to *compound* them by expressing $\boldsymbol{H}_C$ as the product of two block lower triangular matrices, one expressing the uncertainty on the stiffness properties ($\boldsymbol{H}_S$) and the other on the thermal properties ($\boldsymbol{H}_T$), i.e.,

$$\boldsymbol{H}_C = \boldsymbol{H}_T \, \boldsymbol{H}_S \tag{4.21}$$

where

$$\boldsymbol{H}_T = \begin{pmatrix} \boldsymbol{I} & \boldsymbol{0} \\ \boldsymbol{H}_{TS} & \boldsymbol{*} \end{pmatrix} \text{ and } \boldsymbol{H}_S = \begin{pmatrix} \boldsymbol{H_K} & \boldsymbol{0} \\ \boldsymbol{0} & \boldsymbol{I} \end{pmatrix}. \tag{4.22), (4.23}$$

In the above equations, $\boldsymbol{I}$ denotes the identity matrix of appropriate dimensions. Rewriting Eq. (4.19) with Eq. (4.21) yields

$$\boldsymbol{K}_C = \bar{\boldsymbol{L}}_C \, \boldsymbol{H}_T \, \boldsymbol{H}_S \, \boldsymbol{H}_S^T \, \boldsymbol{H}_T^T \, \bar{\boldsymbol{L}}_C^T = \left(\bar{\boldsymbol{L}}_C \, \boldsymbol{H}_T\right) \boldsymbol{H}_S \, \boldsymbol{H}_S^T \left(\bar{\boldsymbol{L}}_C \, \boldsymbol{H}_T\right)^T \tag{4.24}$$

from which it is seen that the randomization of the structural properties is a two-step process. First is the randomization by $\boldsymbol{H}_T$ transforming the mean model matrix $\bar{\boldsymbol{K}}_C$ into the random one

$$\boldsymbol{K}_C = \bar{\boldsymbol{L}}_C \boldsymbol{H}_T \boldsymbol{H}_T^T \bar{\boldsymbol{L}}_C^T = \left(\bar{\boldsymbol{L}}_C \boldsymbol{H}_T\right)\left(\bar{\boldsymbol{L}}_C \boldsymbol{H}_T\right)^T \tag{4.24}$$

which serves as a mean model for the further randomization by $\boldsymbol{H}_S$.

The selection of blocks of the $\boldsymbol{H}_S$ and $\boldsymbol{H}_T$ matrices as the identity or the zero matrix does not conform with the discussion of Fig. 1.1 but it is consistent with the extended nonparametric formulation developed in (Mignolet and Soize 2008) in which the uncertainty associated with the corresponding eigenvalues is set to zero while no constraint is imposed on the variability of the other eigenvalues. Accordingly, the block $\boldsymbol{H}_{TS}$ is simulated from off-diagonal elements of the matrix $\boldsymbol{H}$ of Fig. 1.1, i.e., from independent identically distributed zero mean Gaussian random processes with standard deviation σ_T related to a uncertainty level δ_T, see below.

Performing the matrix multiplications in Eqs (4.21) and (4.24) and comparing the results with Eqs (4.8) and (4.20) leads to

$$\boldsymbol{H}_{th} = \boldsymbol{H}_{TS} \boldsymbol{H}_{\boldsymbol{K}}^T \tag{4.25}$$

$$\boldsymbol{F}_{th} = \bar{\boldsymbol{L}}_{\boldsymbol{K}} \boldsymbol{H}_{\boldsymbol{K}} \boldsymbol{H}_{TS}^T + \bar{\boldsymbol{L}}_{\boldsymbol{K}} \boldsymbol{H}_{\boldsymbol{K}} \boldsymbol{H}_{\boldsymbol{K}}^T \bar{\boldsymbol{L}}_{th}^T \tag{4.26}$$

together with Eq. (4.1) for the stiffness matrix.

Note in Eq. (4.26) that $\boldsymbol{F}_{th}$ involves the compounding of the uncertainties in the structural and thermal properties in $\boldsymbol{H}_{\boldsymbol{K}}$ and $\boldsymbol{H}_{TS}$, respectively, which is consistent

with the fact that $\boldsymbol{F}_{th}$ involves both properties. On the contrary, the stiffness matrix $\boldsymbol{K}$ only involves the structural uncertainties in $\boldsymbol{H}_{\boldsymbol{K}}$, also consistently with its definition.

Moreover, the stiffness matrix $\boldsymbol{K}$ and the vector $\boldsymbol{F}_{th}$ of the uncertain structures must retain the properties (a) and (b) above with respect to the rigid body modes, i.e.,

$$\boldsymbol{K}\,\boldsymbol{\Phi}_{RB} = \boldsymbol{0} \quad \text{and} \quad \boldsymbol{\Phi}_{RB}^{T}\boldsymbol{F}_{th} = \boldsymbol{0} \qquad (4.27), (4.28)$$

Both of these conditions are satisfied by the forms of Eq. (4.1) and (4.26) since

$$\bar{\boldsymbol{L}}_{\boldsymbol{K}}^{T}\,\boldsymbol{\Phi}_{RB} = \bar{\boldsymbol{L}}_{\boldsymbol{K}}\,\boldsymbol{\Phi}_{RB} = \boldsymbol{0} \qquad (4.29)$$

It remains to select the form of the random matrix $\boldsymbol{H}_{TS}$ to complete the formulation. As discussed in (Song and Mignolet 2018) and above, it is necessary that this matrix be such that each realization of the thermal force vector $\boldsymbol{F}_{th}$ permutes, as the mean model, under a permutation of the node numbers. To express this condition, let

$$\boldsymbol{P}_e = \text{Bdiag}\left(\boldsymbol{P}_r, \boldsymbol{P}_r, \ldots, \boldsymbol{P}_r\right) \qquad (4.30)$$

where Bdiag is the operation creating a block diagonal matrix of the blocks specified and $\boldsymbol{P}_r$ is an arbitrary *r*x*r* permutation matrix where, as before, *r* is the number of nodes per element. Under this permutation,

$$\bar{\boldsymbol{K}} \;\rightarrow\; \boldsymbol{P}_e^{T}\,\bar{\boldsymbol{K}}\,\boldsymbol{P}_e \quad \text{and thus} \quad \bar{\boldsymbol{L}}_{\boldsymbol{K}} \;\rightarrow\; \boldsymbol{P}_e^{T}\,\bar{\boldsymbol{L}}_{\boldsymbol{K}}\,\boldsymbol{P}_e \qquad (4.31), (4.32)$$

$$\bar{\boldsymbol{F}}_{th} \;\rightarrow\; \boldsymbol{P}_e^{T}\,\bar{\boldsymbol{F}}_{th} \quad \text{and thus} \quad \bar{\boldsymbol{L}}_{th} \;\rightarrow\; \bar{\boldsymbol{L}}_{th}\,\boldsymbol{P}_e \qquad (4.33), (4.34)$$

Then, one also needs Eqs (4.31) and (4.33) to be true for the uncertain matrices, i.e.,

$$\boldsymbol{K} \;\rightarrow\; \boldsymbol{P}_e^{T}\,\boldsymbol{K}\,\boldsymbol{P}_e \quad \text{and} \quad \boldsymbol{F}_{th} \;\rightarrow\; \boldsymbol{P}_e^{T}\,\boldsymbol{F}_{th} \qquad (4.35), (4.36)$$

The condition (4.35) implies

$$\boldsymbol{P}_e^T \, \boldsymbol{H_K} \, \boldsymbol{H_K}^T \, \boldsymbol{P}_e = \boldsymbol{H_K} \, \boldsymbol{H_K}^T \tag{4.37}$$

which is automatically satisfied by Eq. (4.6) as

$$\boldsymbol{P}_e^T \, \boldsymbol{H_K} \, \boldsymbol{P}_e = \boldsymbol{H_K} \ . \tag{4.38}$$

Focusing next on the condition (4.36), it can be rewritten with the above results as

$$\boldsymbol{H}_{TS} \quad \rightarrow \quad \boldsymbol{H}_{TS} \, P_e \tag{4.39}$$

to be satisfied for every realization in $\boldsymbol{H}_{TS}$. A first approach to satisfy this condition is to impose

$$\boldsymbol{H}_{TS} \, P_e = \boldsymbol{H}_{TS} \tag{4.40}$$

which is satisfied by

$$\boldsymbol{H}_{TS} = \boldsymbol{h}_{TS} \otimes \boldsymbol{J}_r \tag{4.41}$$

where $\boldsymbol{h}_{TS}$ is a row vector of *m* components defined as random fields with a specified correlation length; and $\boldsymbol{J}_r$ denotes the row vector of dimension *r* with all elements equal to one.

The selection of Eq. (4.41) leads however to negligible uncertainty effects in the absence of structural uncertainty. This occurs because the Kronecker product by $\boldsymbol{J}_r$ effectively induces vectors $\boldsymbol{H}_{TS}$ which are along the rigid body modes only. Then, the product $\bar{\boldsymbol{L}}_{\boldsymbol{K}} \, \boldsymbol{H}_{TS}^T$ is zero and, in the absence of structural uncertainty, i.e., with $\boldsymbol{H_K}$ equal to the identity matrix, one finds from Eq. (4.26) that $\boldsymbol{F}_{th} = \bar{\boldsymbol{F}}_{th}$. Thus, no uncertainty is introduced in the system.

Another approach to satisfy Eq. (4.39) is to express $\boldsymbol{H}_{TS}$ in terms of a mean model matrix/vector which exhibits the permutation. Given the size of the block $\boldsymbol{H}_{TS}$, it is proposed here to express it in terms of $\bar{\boldsymbol{L}}_{th}$ as

$$\boldsymbol{H}_{TS} = \bar{\boldsymbol{L}}_{th}\,\boldsymbol{U} \tag{4.42}$$

where $\boldsymbol{U}$ is a random matrix. Given Eq. (4.34), Eq. (4.39) would be satisfied by a matrix $\boldsymbol{U}$ proportional to the identity matrix but the more general form would satisfy

$$\boldsymbol{P}_e^T\,\boldsymbol{U}\,\boldsymbol{P}_e = \boldsymbol{U}\,. \tag{4.43}$$

This condition is satisfied in particular with

$$\boldsymbol{U} = \mathrm{diag}\left(\boldsymbol{h}_{TS} \otimes \boldsymbol{J}_r\right) \tag{4.44}$$

where diag is the operation taking a vector and creating the diagonal matrix having these elements along the diagonal.

The application of the above approach to introduce uncertainty in a heated structure thus proceed as follows. First, from the mean model stiffness matrix $\bar{\boldsymbol{K}}$, determine $\bar{\boldsymbol{L}}_{\boldsymbol{K}}$ according to Eq. (4.11) and in the process find the deformation modes $\bar{\boldsymbol{\Phi}}_D$ and the corresponding matrix of eigenvalues $\bar{\boldsymbol{\Lambda}}_D$. Then, from the mean model thermal forces $\bar{\boldsymbol{F}}_{th}$, determine the vector $\bar{\boldsymbol{p}}$ according to Eq. (4.16) and the representation of $\bar{\boldsymbol{L}}_{th}$ from Eqs (4.17) and (4.18). This completes the decomposition of the mean model.

The introduction of uncertainty is achieved next with the *m*x*m* random matrix $\boldsymbol{H}$ simulated as described in Eqs (4.3)-(4.5) from a set of independent Gaussian random processes with specified correlation length and with an uncertainty level δ_S relating to Fig. 1.1 according to

$$\sigma_S = \frac{\delta_S}{\sqrt{m+1}} \quad \text{and} \quad \mu_S = \frac{1}{2\sigma_S^2} \qquad (4.45), (4.46)$$

Each realization of this matrix is then multiplied (Kronecker product) by $\boldsymbol{I}_r$ to obtain the corresponding sample of $\boldsymbol{H}_{\boldsymbol{K}}$, Eq. (4.6), and then of the stiffness matrix $\boldsymbol{K}$ using Eq. (4.1).

Next, samples of *m* additional independent Gaussian random processes with specified correlation length (not necessarily the same as for the structural problem) are generated and multiplied by the common standard deviation $\sigma_T = \delta_T / \sqrt{m+3}$, δ_T being the thermal uncertainty level. They are then stacked in the vector $\boldsymbol{h}_{TS}$ from which realizations of the vector $\boldsymbol{H}_{TS}$ are obtained using Eqs (4.42) and (4.44). Finally, the realizations of the random thermal force vector $\boldsymbol{F}_{th}$ are computed from Eq. (4.26).

4.4. Validation on Correlation Length of Elemental Matrix Components

The construction of the random elemental matrices according to Eqs (4.1)-(4.6) and (4.44) relies on 2 parameters, the overall uncertainty level δ and the correlation length L_{corr}. While the former parameter is well defined in terms of the elemental matrices, see Eq. (10), the latter operates at the upstream stage of the simulation of the random fields P_{ij}. Accordingly, it is desirable to first assess how L_{corr} relates to the correlation between components of the simulated $\boldsymbol{K}$ matrices of different elements.

To this end, two structural models were constructed with 100 identical beam elements, one in straight line, the other forming a half circle, see Fig. 4.1. The finite element model was developed in Nastran with CBEAM elements with 6 degrees of freedom per node and 2 nodes per elements, i.e., 12 degrees of freedom per element.

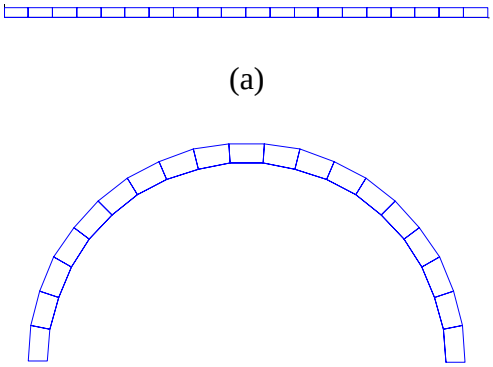

(a)

(b)

Figure 4.1. Beam Models for Correlation Length Analysis. (a) Straight Beam, (b) Half Circle Beam.

Each element of the mean model of the two structures was assumed to have length 0.0057m, a rectangular cross section with sides 0.0127m (width) × 7.88 10^{-4}m (thickness) and be made of homogenous, isotropic, elastic material with Young modulus E = 73.000MPa and Poisson's ratio of ν = 0.316. The correlation length L_{corr} and uncertainty level δ of the random fields P_{ij} were set to 10 element lengths, i.e., 0.057m, and 0.1, respectively. For the curved beam, the correlation length was quantified along the arc length of the inner circle.

Since the mean elemental matrices of each element are identical, the random elemental matrices of elements $K_{ij}(n)$, n denoting the element number (between 1 and 100), are at least wide sense stationary and one can compute the correlation lengths

$$L_{corr}^{(ij)} = \frac{\sum_{m=1} \left| R_{KK}^{(ij)}(m) \right|}{R_{KK}^{(ij)}(0)} \tag{4.47}$$

where $R_{KK}^{(ij)}(m)$ denotes the autocovariance of the component *ij* of the random elemental stiffness matrix defined as

$$R_{KK}^{(ij)}(m) = E\left\{\left[K_{ij}(n) - \bar{K}_{ij}\right]\left[K_{ij}(n+m) - \bar{K}_{ij}\right]\right\} \tag{4.48}$$

Then, shown in Fig. 4.2 is a sample of the autocovariance functions of the elements $K_{ij}(n)$ and of the random field P_{11} as estimated from the population of 3000 realizations using Eq. (4.48) with *n* = 1. Next, performing the summation over all lags *m* = 1, ..., 99 in Eq. (4.47) leads to the correlation lengths which are shown in Fig. 4.3 and which are very similar to those of the random fields P_{ij}. It appears from Figs 4.2 and 4.3 that the simulated components of the elemental stiffness matrix obey a correlation structure similar to the one of the original Gaussian fields P_{ij}.

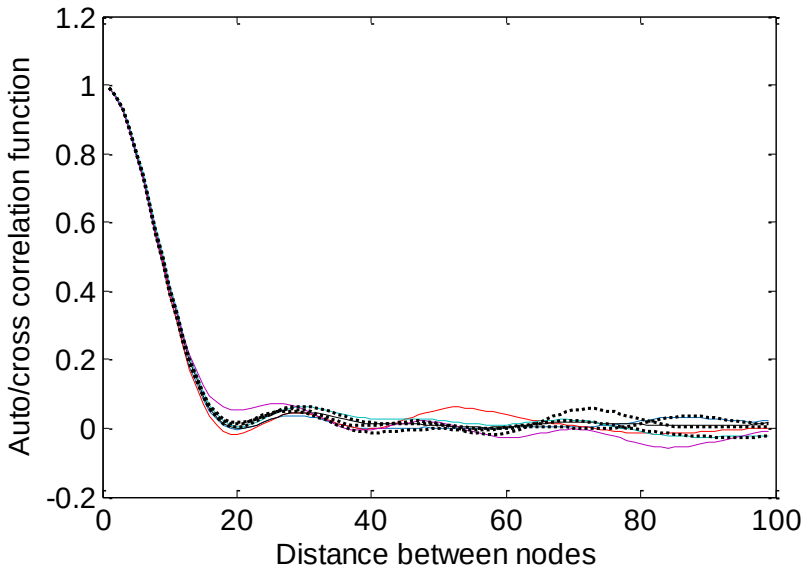

Figure 4.2. Autocovariance Functions of Some Components $K_{ij}(n)$ (in Colors) and $P_{ij}(n)$ (in Black Dashed Lines).

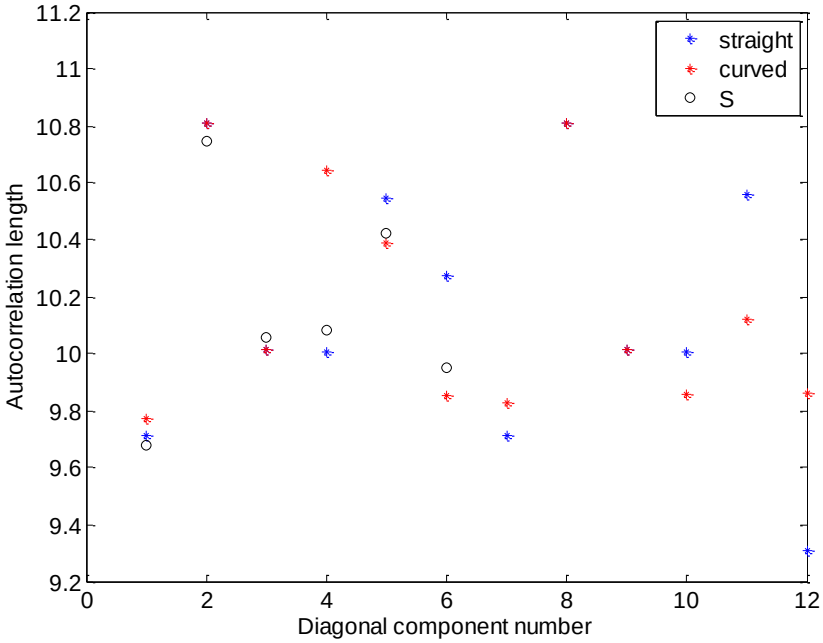

(a)

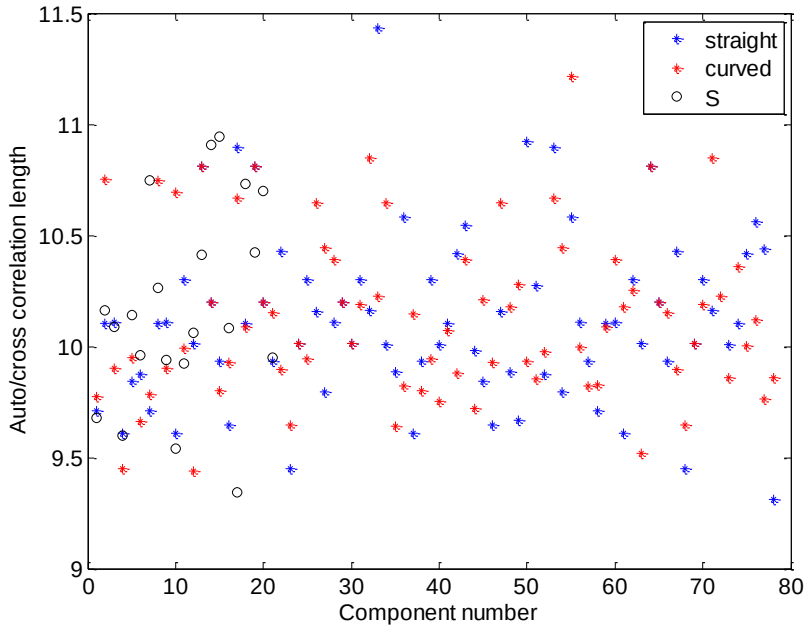

(b)

Figure 4.3. Correlation Length of the Components $K_{ij}(n)$ (in Number of Elements) for the Straight and Curved Beams. (a) Diagonal Components, $i = j$ =1, .., 12, (b) All Components, $i \geq j$. Also Shown On Are the Correlation Lengths of the Processes $P_{ij}(n)$, (a) $i = j$ =1, .., 6, (b) $i \geq j$, i.

4.5. Application Example

To illustrate the above uncertainty modeling, consider the annulus shown in Fig. 4.4 of inner radius 0.8m, outer radius 1m, thickness 0.002m clamped on its inner radius and free on the outer one. The material, aluminum, is assumed to be homogenous and isotropic with Young's modulus $E = 7.3\ 10^{10}$ Pa, Poisson's ratio $\nu = 0.316$, and coefficient of thermal expansion $\alpha = 2.5\ 10^{-5}$/°C. The annulus is subjected to a uniform pressure of 1Pa or a uniform temperature of 1°C in the quadrant $\theta \in [180,270]$ degrees highlighted in yellow in Fig. 4.4. To evaluate the displacement field of the annulus, it was modeled by 4-node (so $r = 4$) shell finite elements within Nastran (CQUAD4 elements) with a mesh of 144 nodes around the periphery and 6 in the radial direction. Each node has 6 degrees of freedom and thus $m = 6$.

The autocorrelation function of (Soize 2006) was selected here with a correlation length equivalent to 60 deg. of the internal radius or about 24 elements Moreover, the structural uncertainty level δ_S was set to 0.1 which corresponds to a coefficient of variation of the first natural frequency of the entire structure equal to 3%. Then, with a uniform pressure loading, shown in yellow in Fig. 4.5(a) is the uncertainty band corresponding to the 5th and 95th percentile of the transverse displacement of the periphery as determined from the 300 samples of the response. The response is clearly localized as the one from the mean model. For comparison, shown in Fig. 4.5(b) is the uncertainty band generated by the approach of (Song and Mignolet 2018). While a one to one comparison of the bands cannot be made as the methods involve different parameters, it is clear that the predictions are similar in all qualitative aspects.

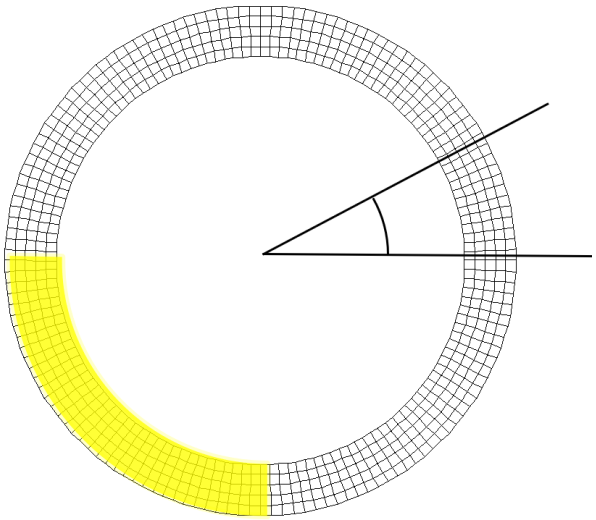

Figure 4.4 . The Annulus and Its Finite Element Model, Loading Domain Highlighted in Yellow.

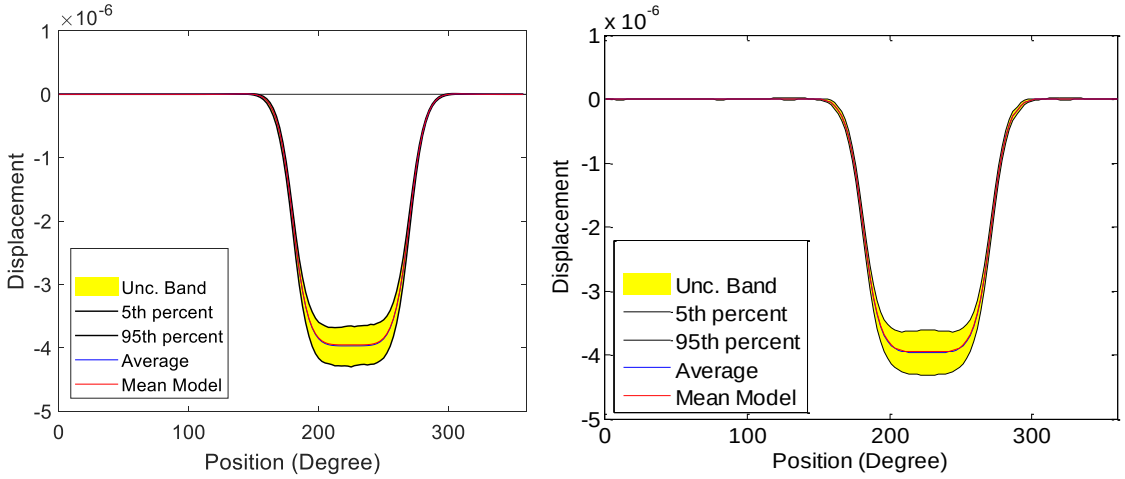

Figure 4.5. Static Transverse Displacement at the Periphery of the Mean Annulus (in Red) and 5th-95th Percentile Uncertainty Band from (a) the Above Uncertain Finite Element Model, (b) (Song and Mignolet 2018).

Next the loading was changed to temperature loading only, i.e., with $\boldsymbol{F}_{str} = \boldsymbol{0}$ on all elements. The correlation length was also set to 60 degree and δ_S was set to 0.1. The matrix $\boldsymbol{H}_{TS}$ was set to zero so that the uncertainty is on the structural only terms. Then, shown in Fig. 4.6 are the 5th-95th percentile uncertainty bands of the displacements at the

edge obtained from 300 realizations. Note that the band in the transverse direction includes both positive and negative values with an average approximately zero which is the mean model result. Thus, the introduction of uncertainty has led to transverse displacements not existing in the mean model, i.e., epistemic uncertainty has indeed been introduced.

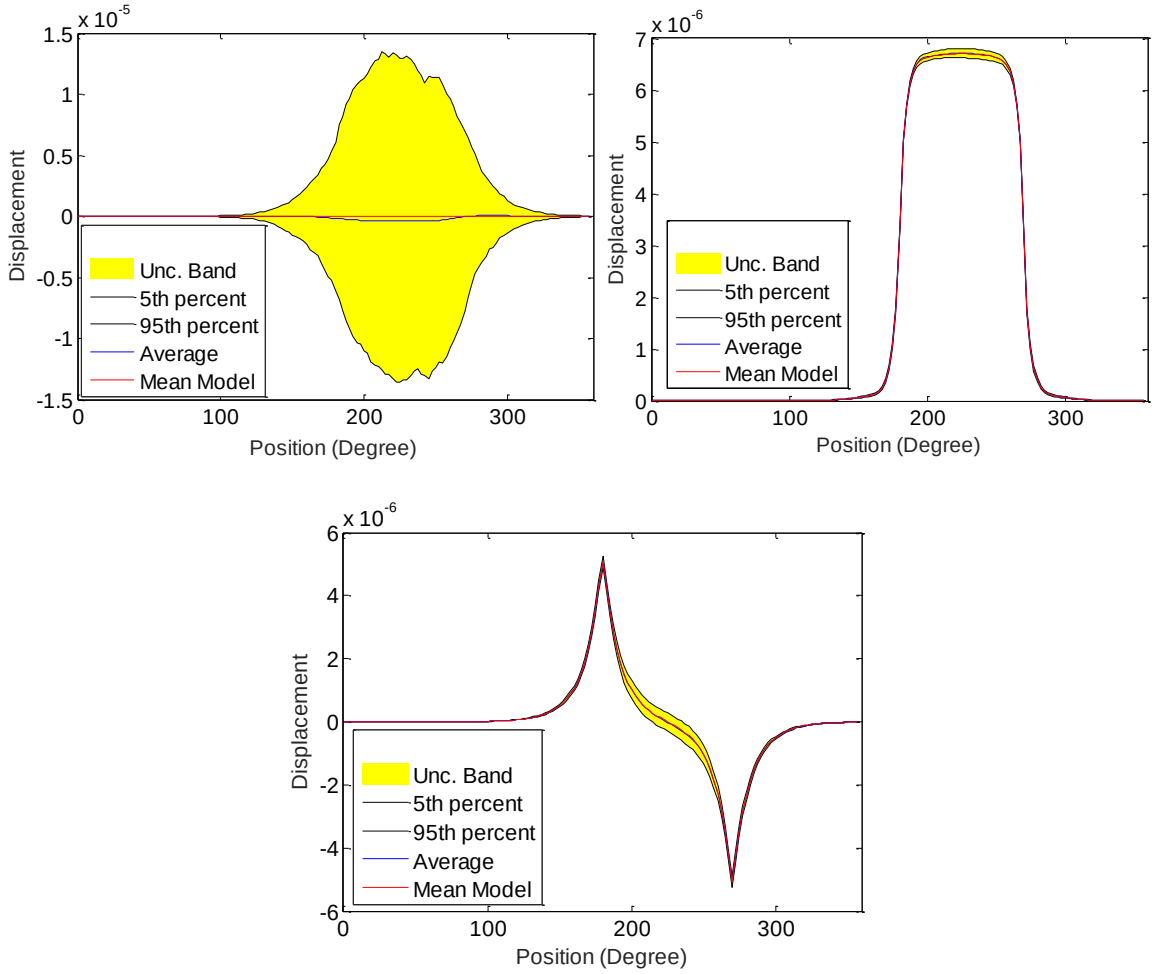

Figure 4.6 Displacements (in m) at the Periphery of the Mean Annulus (in Red) and 5th-95th Percentile Uncertainty Band in (a) Transverse, (b) Radial and (c) Tangential Direction. Uncertainty on Stiffness.

It was next of interest to introduce uncertainty on the thermal force part only. This is done by setting $\boldsymbol{H_K}$ as the identity matrix in Eqs (4.1) and (4.26) leaving the

uncertainty from the $\boldsymbol{H}_{TS}$ block only. The elements of this matrix were simulated as in Eqs (4.42) and (4.44) with the same correlation length of 60 degree of the internal radius and an uncertainty level δ_T =0.1. Then, shown in Fig. 4.7 are the 5th-95th percentile uncertainty band in the transverse, radial, and tangential directions at the edge of the plates obtained from 300 realizations. Note here that the structural symmetry of the flat annulus has not been modified since there is no structural uncertainty and thus the transverse displacements are zero as for the mean model.

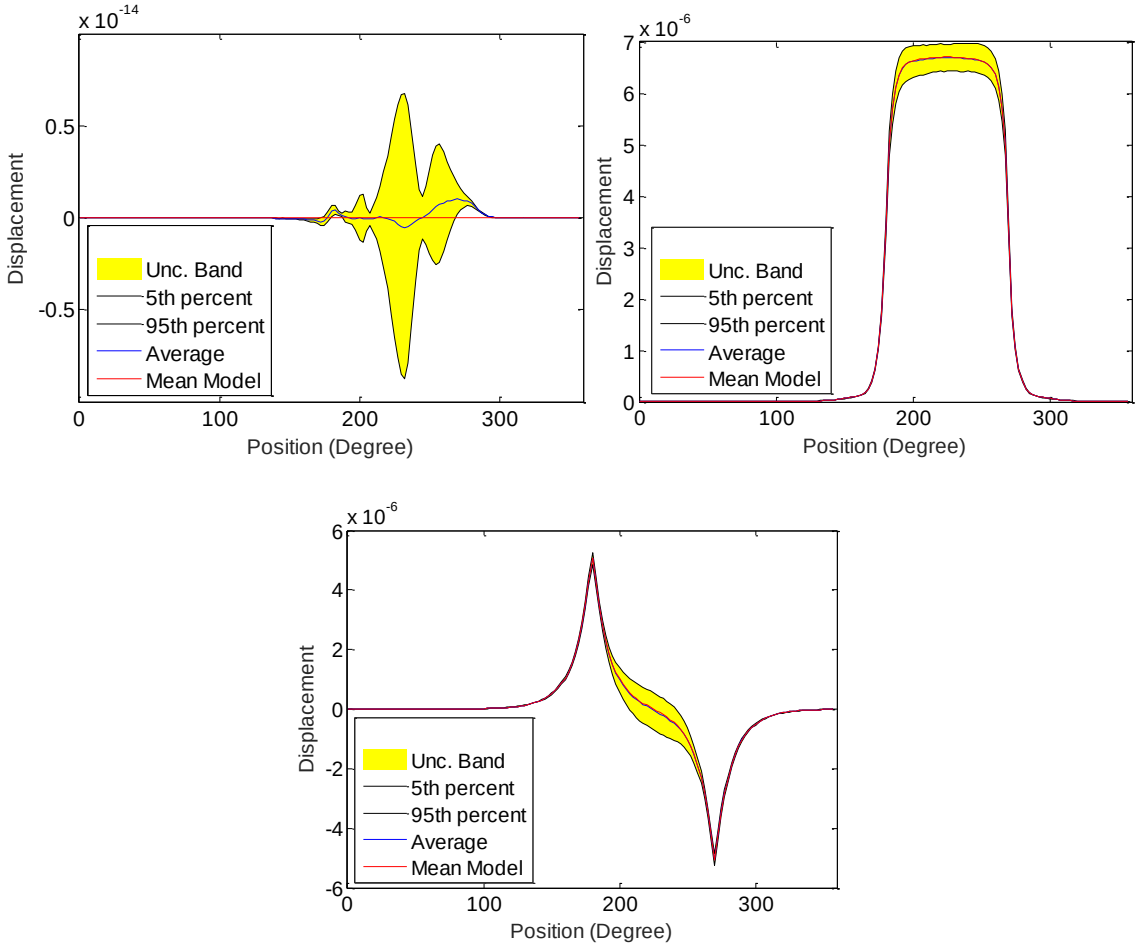

Figure 4.7 Displacements (in m) at the Periphery of the Mean Annulus (in Red) and 5th-95th Percentile Uncertainty Band in (a) Transverse, (b) Radial and (c) Tangential Direction. Uncertainty on Thermal Force Only.

Finally, shown in Fig. 4.8 are the uncertainty bands obtained when combining both types of uncertainties. As expected, these bands are then wider than they are when either set of uncertainty alone is present but only marginally so.

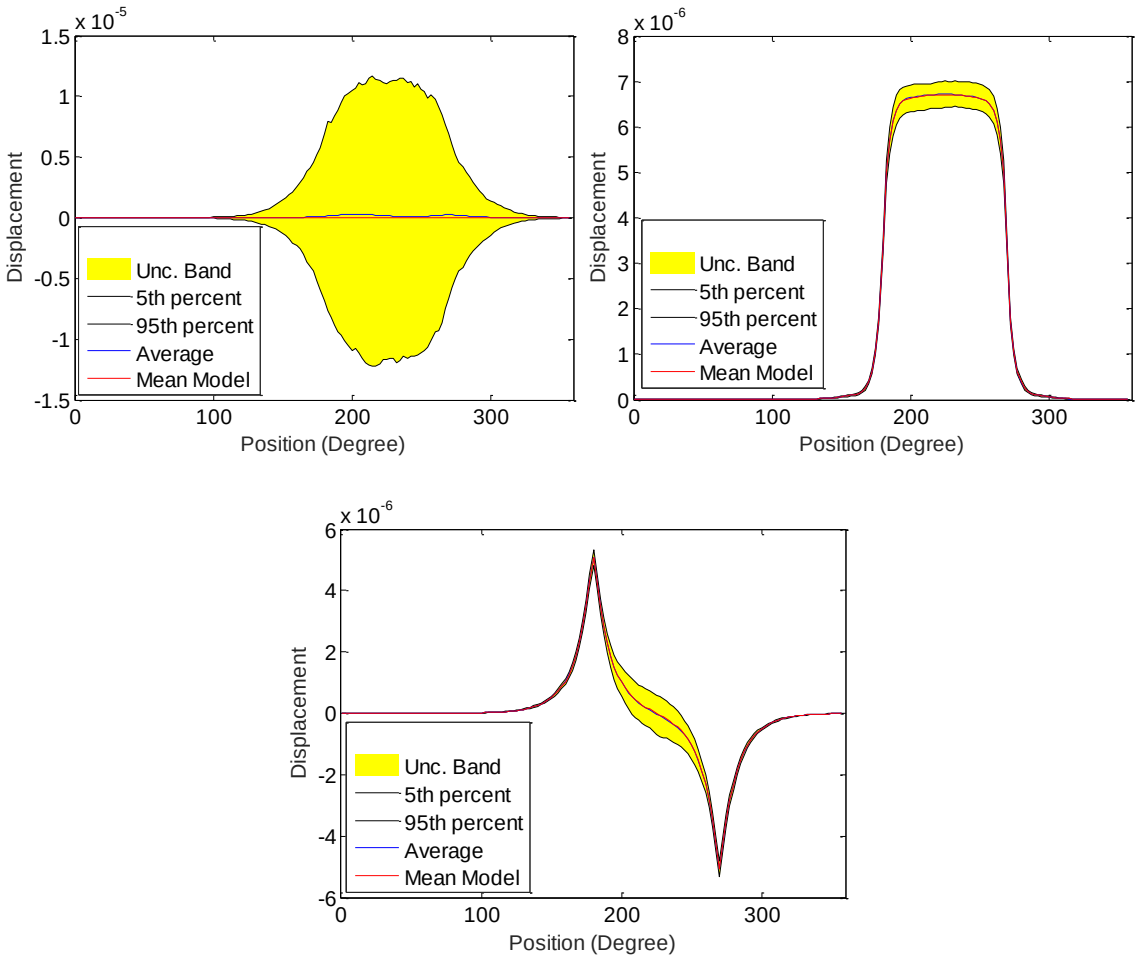

Figure 4.8 Displacements (in m) at the Periphery of the Mean Annulus (in Red) and 5th-95th Percentile Uncertainty Band in (a) Transverse, (b) Radial and (c) Tangential Direction. Uncertainty on Both Stiffness and Thermal Force.

4.6. Summary

The focus of this investigation was on the development and first validation of a novel uncertainty modeling strategy that operates at the elemental level of finite element models of heated linear structures. A key feature of the approach is that the elemental

stiffness matrix and thermal force vector are simulated *jointly* to respect the dependence of both of them on the elasticity properties of the structure. Following the maximum entropy approach, the method produces samples of these elemental matrices and vectors given their mean and two sets of parameters that describe (i) the overall level of uncertainty (structural and thermal separately) and (ii) the correlation of the structural and coefficient of thermal expansion properties, separately, across the structure. Owing to the use of the maximum entropy approach, the proposed modeling strategy accounts for aleatoric and some epistemic uncertainty of both types of material properties. The ease of application of the method was demonstrated on a first example.

5. NONLINEAR REDUCED ROMS: FORMULATION AND APPLICATIONS

5.1. Introduction

Nonlinear reduced order models are built by first choosing a sufficient number of modes to form the basis functions. These chosen modes must be able to capture the response of the structure over its entire trajectory and up to a required accuracy. Even under white noise dynamic excitations, but especially in static conditions, this mode selection strategy often overstates the number of modes that are really active/play an important role in the response prediction. The penalty for having a basis too large is an increase in computational cost in (i) identifying the ROM and (ii) computing the solution, especially in multi-physics problems.

The approach investigated here to address this issue is a data-driven reduction of the ROM into a reduced ROM (RROM). This reduction would proceed as follows. Firstly, the (full) ROM would be used to compute the response for an appropriate number of loading conditions or time steps, e.g., these could be the first 10 to 15 of a series of similar static loadings in a static problem or the first 10 to 15 time steps in a transient problem. This data would then be used, in a proper orthogonal decomposition (POD) format, to rotate the ROM basis into a set of modes that represent the response in the most compact form. These modes would be those, and only those, that are kept for the RROM.

It is anticipated that the RROM would be used to compute the response for the next series of loading conditions/time steps, then a check would take place to assess whether the RROM is still valid. If yes, then continue march the RROM. If not, then the full ROM would be restarted for another number of loading conditions/time steps with the previous

RROM results as initial conditions. This new full ROM data then can be used for determining new RROM.

The ROM reduction strategy would be particularly helpful when considering uncertainty given (i) the repeated computations that are required in a Monte-Carlo simulation, and (ii) that the ROM reduction can actually be modeled as epistemic uncertainty and thus accounted in the computations.

5.2. Reduced ROM

5.2.1. Basis Reduction

Let the snapshots of the full ROM generalized coordinates q_i , i = 1, ..., $\bar{M}$, at each load level s or time step s be stacked into a vector $\boldsymbol{q}_S$ and let the matrix $\boldsymbol{Q}$ be formed as $\boldsymbol{Q} = [\boldsymbol{q}_1, \boldsymbol{q}_2, \dots, \boldsymbol{q}_N]$, where N is the number of snapshots selected. Next, a POD analysis is performed on the matrix $\boldsymbol{Q}$ and the first several eigenvectors $\boldsymbol{u}_i$ of the matrix $\boldsymbol{Q}\boldsymbol{Q}^T$ are used to define the new basis. Denoting the eigenvector matrix $\boldsymbol{U} = [\boldsymbol{u}_1, \boldsymbol{u}_2, \dots, \boldsymbol{u}_M]$, where M is the number of POD eigenvectors retained, the new basis can be expressed as

$$\boldsymbol{\Psi}_r = \boldsymbol{\Psi}_f \boldsymbol{U} \tag{5.1}$$

where $\boldsymbol{\Psi}_{\mathrm{f}} = \left[\boldsymbol{\Psi}^{(1)}, \boldsymbol{\Psi}^{(2)}, \dots, \boldsymbol{\Psi}^{(\bar{\mathrm{M}})}\right]$ includes the modes of the full ROM and $\boldsymbol{\Psi}_{\mathrm{r}} = \left[\boldsymbol{\Psi}_{\mathrm{r}}^{(1)}, \boldsymbol{\Psi}_{\mathrm{r}}^{(2)}, \dots, \boldsymbol{\Psi}_{\mathrm{r}}^{(\mathrm{M})}\right]$ contains the modes in the reduced ROM.

A practical detail of the above approach relates to the dual modes whose generalized coordinates are typically much smaller than those of the linear modes. Yet, it is known that their contributions to the response is fundamental. Moreover, it was desired to maintain one part of the basis as originating from the low frequency linear modes of the

structure. This situation has led to the following two-step application of the above strategy.

The generalized coordinates associated with the transverse/linear modes are first considered leading to a snapshot matrix $\boldsymbol{Q}^{(t)}$, where *t* denotes transverse part. The size of this matrix is $n_t \times N$, where n_t is the number of transverse modes in the full ROM. Once the corresponding eigenvector matrix, denoted as $\boldsymbol{U}^{(t)}$, has been determined, the residuals of the projection of the transverse response of the full ROM on the reduced ROM basis can be evaluated at each snapshot as

$$\boldsymbol{Q}^{(res)} = \boldsymbol{Q}^{(t)} - \boldsymbol{U}^{(t)}\boldsymbol{x} \tag{5.2}$$

where $\boldsymbol{x}$ is the best fit of the equation $\boldsymbol{U}^{(t)}\boldsymbol{x} = \boldsymbol{Q}^{(t)}$.

In the second step, these above residuals are grouped with the dual part of the selected snapshots to form the matrix

$$\boldsymbol{Q}' = \begin{bmatrix} \boldsymbol{Q}^{(res)} \\ \boldsymbol{Q}^{(d)} \end{bmatrix} \tag{5.3}$$

where $\boldsymbol{Q}^{(d)}$ is the dual part of $\boldsymbol{Q}$, and has dimension $\left(\bar{M} - n_t\right) \times N$. Then, the dual part of the reduced ROM basis is achieved by performing the POD analysis on $\boldsymbol{Q}'$, leading to the transformation matrix $\boldsymbol{U}'$. Assembling the two steps leads to the combined transformation matrix

$$\boldsymbol{U} = \begin{bmatrix} \boldsymbol{U}^{(t)} & \boldsymbol{U}'^{(t)} \\ 0 & \boldsymbol{U}'^{(d)} \end{bmatrix} \text{ where } \boldsymbol{U}' = \begin{bmatrix} \boldsymbol{U}'^{(t)} \\ \boldsymbol{U}'^{(d)} \end{bmatrix} \tag{5.4}$$

to be used in Eq. 5.1.

When the structure is subjected to the effects of temperature, in addition to mechanical/aerodynamic loading, the structural basis is increased by a series of "thermal enrichments", i.e., basis functions necessary to capture the displacements induced by the temperature which often are different from those resulting from mechanical/aerodynamic loads. When such enrichments are present, their reduction is done separately of the linear and duals modes as a third POD step leading to a transformation matrix $\boldsymbol{U}^{(e)}$ which can be combined with those from the transverse and dual modes as

$$\boldsymbol{U} = \begin{bmatrix} \boldsymbol{U}^{(t)} & \boldsymbol{U}'^{(t)} & \mathbf{0} \\ \mathbf{0} & \boldsymbol{U}'^{(d)} & \mathbf{0} \\ \mathbf{0} & \mathbf{0} & \boldsymbol{U}^{(e)} \end{bmatrix}. \tag{5.5}$$

Finally, the reduction of the thermal basis is also achieved, as above but in a single step leading to a separate transformation matrix $\boldsymbol{V}$.

5.2.2. Evaluation of ROM Coefficients

Having established the basis of the RROM, it remains to determine its stiffness coefficients. This identification could be performed as for the full ROM, see (Mignolet et al 2013, Perez et al 2014, Perez et al 2011, Matney et al 2011), but this effort can be significantly reduced by recognizing that the dependence of the governing equations on the generalized coordinates (structural and thermal) is polynomial. Accordingly, it is possible to map directly the RROM coefficients from their ROM counterparts. For instance:

$$K_{ab}^{(1)} = \bar{K}_{ij}^{(1)} U_{ia} U_{jb} \tag{5.6}$$

$$K^{(2)}_{abc} = \bar{K}^{(2)}_{ijl} U_{ia} U_{jb} U_{lc} \tag{5.7}$$

$$K^{(3)}_{abcd} = \bar{K}^{(3)}_{ijlp} U_{ia} U_{jb} U_{lc} U_{pd} \tag{5.8}$$

$$K^{(th)}_{abc} = \bar{K}^{(th)}_{ijl} U_{ia} U_{jb} V_{lc} \tag{5.9}$$

where the coefficients with overbar are those of the full ROM and those without refer to the RROM.

5.3. Validation Example

A first assessment of the RROM methodology was conducted on the panel with stiffeners in Section 3.6, see Fig. 3.12, which was originally considered in (Culler and McNamara 2011) and is subjected to a trajectory spanning Mach 2 to Mach 12 in 300 seconds with fully coupled structural/thermal/aerodynamic computations. From the summary presented in Section 3.6, recalled that the coupled solution procedure between the thermal and structural models are staggered and time-marched with a step of 0.5s. The thermal solution at one time step is obtained first, from the thermal and structural fields at the previous time step. Then, the structural problem is solved using the current temperature distribution.

As shown in Section 3.6, a structural-thermal ROM of this panel providing a close match of finite element results was developed in (Matney et al 2015) and shown in Fig. 3.13 is a comparison of the maximum transverse displacement and the temperature of the center of the panel predicted by the finite element model (Culler and McNamara 2011) and by the ROM (Matney et al 2015). In this ROM, the structural model included 44 structural basis functions, split into linear modes, dual modes, and thermal enrichments, and 42 thermal basis functions. The construction of the structural basis followed a series

of steps that have been practiced on a variety of structural models and thus was considered to be close to optimal. The construction of the thermal basis however was more challenging owing to the potential for the temperature distribution to exhibit local effects which are difficult to predict a priori in this fully coupled problem. It is thus expected that the thermal basis could likely be reduced. A simple metric used below to evaluate the computational advantage of the reduction in bases is the number of coefficients in the ROM. Since the coefficient of thermal expansion depends linearly on temperature while the tensor or elasticity does not, the number of structural ROM coefficients is of order $M^4/6 + M^2\mu^2/4$ which is much larger than those present in the thermal ROM, i.e., order of $\mu^2/2$ coefficients. Thus, only the reduction in structural ROM coefficients is considered below. Clearly, the evaluation of the restoring force from the linear, quadratic, and cubic stiffness terms is not the only computational cost involved in marching the ROM but it may be expected to be the dominant one for *M* large enough as the solution of linear equations, involved in any marching/solution procedure, would only involve order of M^3 or μ^3 operations.

5.3.1. Effects of Size of RROMs

Given its complexity, the size of the bases, and the presence of two different ROMs, structural and thermal, this problem is an excellent test case to validate the Reduced ROM concept. It was first desired to assess whether a reduction of the bases could actually be achieved. To this end, a somewhat typical span of the full ROM data was selected, i.e., between 76 and 100 seconds of the mission. During that time, the panel exhibits a rapid increase in the transverse response. The corresponding ROM data, i.e.,

the 50 snapshots of displacements and temperature distributions was then treated by the 3-step POD approach described above and led to several sets of M structural modes and μ thermal ones, depending on the number of eigenvectors retained in the POD analysis. Each of these RROMs was then identified, i.e., a complete identification was performed here vs. using Eqs. (5.6) - (5.9) to avoid possible loss of accuracy issues that would have clouded the discussion of the results presented below. Finally, each RROM was marched in the same manner as the full ROM and its structural and thermal predictions were then compared to those of the full ROM. The RROMs were considered accurate as long as largest relative norm of the differences in thermal and structural predictions (taken here as the ROM generalized coordinates) reached 2.5%.

The length of time for which each of these RROM was found to be accurate and the corresponding reduction in the number of coefficients as compared to the full ROM are presented in Table 5.1. Note in this table that the structural ROM order is split between number of linear modes, duals, and thermal enrichments, respectively. Moreover, the reduction in the number of structural coefficients is shown as a percentage of the full number corresponding to the 44 structural modes and 42 thermal ones.

The results of Table 5.1 clearly demonstrate the potential computational benefit of using RROMs, the 30 structural and 10 thermal modes RROM would have nearly 90% less coefficients, so the RROM would run approximately 10 times faster than the ROM. Yet, it would provide an accurate prediction of the response for a significant length of time (54 seconds, approximately 1/6 of the mission length). As the number of structural and thermal modes is decreased, the computational benefit is further increased but the length of time for which the RROM is valid decreases. This finding likely reflects the

evolving nature of the structural deformations and temperature distribution over the mission profile: keeping a small number of modes only allows the capture of the physics in the close neighborhood of where the full ROM data was chosen. It is interesting to note that increasing the order of one of the two physical models, i.e., structural and thermal, does not necessarily increase the span of validity of the RROM, as seen for the two order 15 structural RROM: increasing the number of thermal modes from 5 to 7 does not change this span. It is most likely because matching the structural deformation is the most significant weakness of these RROMs. When the structural order is increased to 30, the increase of the number of thermal modes from 7 to 10 does lead to an increase span of validity, likely because the thermal RROM is now the least accurate.

Table 5.1. RROM Validity and Cost Reduction vs. Order Selected. ROM Data from 76-100s.

Structural RROM orders	Thermal RROM order	Coeff. Reduction (%)			Valid for (s)
		from M	from μ	both	
5+5+5	5	92.7	56.9	99.3	13.5
5+5+5	7	92.7	56.1	99.2	13.5
6+6+6	6	89.2	56.6	98.6	23.5
7+7+7	7	84.7	56.1	97.4	24.5
8+8+8	8	79.1	55.7	95.6	21
9+9+9	9	72.3	55.1	93.0	26.5
10+10+10	7	64.0	56.1	90.1	42
10+10+10	10	64.0	54.5	89.3	54

5.3.2. Effects of Length of Full ROM Data Used

The next step of the RROM assessment was focused on understanding the effects of the span of full ROM data selected for the POD process. This was done by selecting various length of full ROM data, one starting at 76s and another at the beginning (0s) and constructing RROMs of fixed orders, then evaluating for how long these RROMs were

valid. The structural RROM orders were selected as 5+5+5 for the data starting at the beginning and 10+10+10 from 76s onward. In both cases, 7 thermal modes were included in the RROM. As seen in Table 5.2, these orders lead to reductions of the number of structural coefficients by approximately 99% and 90%, respectively.

Table 5.2. RROM Validity and Cost Reduction vs. Span of Full ROM Data.

Data Span (s)	Structural RROM order	Thermal RROM order	Coeff. Reduction			Valid for (s)
			from *M*	from μ	both	
0.5-7	5+5+5	7	92.7	56.1	99.2	42
0.5-13	5+5+5	7	92.7	56.1	99.2	40
0.5-20	5+5+5	7	92.7	56.1	99.2	53
0.5-25	5+5+5	7	92.7	56.1	99.2	65
0.5-35	5+5+5	7	92.7	56.1	99.2	66
76-88	10+10+10	7	64.0	56.1	90.1	26
76-95	10+10+10	7	64.0	56.1	90.1	28
76-100	10+10+10	7	64.0	56.1	90.1	42
76-110	10+10+10	7	64.0	56.1	90.1	58

The results of Table 5.2 confirm what might have been expected, i.e., that using a larger number of snapshots leads to a basis that better captures the physics and thus is valid for longer times but the benefit tapers off as the data length increases. For example, 25 seconds of data at the beginning of the mission permits the prediction for an ensuing 65 seconds but adding 10 more seconds of data (20 more snapshots) only lead to 1 more second of RROM validity. A similar situation can also be seen for the data started at 76s: increasing the data span by 5 seconds, from 20s to 25s, leads to an increase of the accurate prediction range by 14s but increasing the data span by an extra 10s (i.e., 35s total) only increases the prediction range by 16s.

The data of Table 5.2 also indicates that the range of validity of a RROM is not only a function of its orders and data length but also of the evolving physics. Near the

beginning of the mission, the displacements and temperature change slowly as seen in Fig. 3.13 and a low orders RROM may be valid for a "long time", e.g., for 65s using 25s of data. However, around the 76s time, that same length of data and a RROM with structural orders doubled is only valid for 42s. This shorter prediction time reflects the much faster changes in structural deformations and temperatures taking place.

5.4. Development of Adaptive RROMs For Efficiency and Accuracy

The above discussion has demonstrated the strong potential of RROMs to achieve computational effort reductions, but it also shown that the RROMs may not be applicable to the entire range of loading conditions desired and/or the entire mission trajectory. Accordingly, it is proposed here to proceed with a succession of full ROM/RROM computations where the RROMs are *adapted* to previously determined full ROM data as follows, see Fig. 5.1 for flowchart.

(i) March the full ROM for a small span of time/loading conditions.

(ii) Based on these responses of the full ROM, construct a RROM by the multi step POD process.

(iii) Start marching the RROM with initial conditions corresponding to the full ROM end point projected on the RROM basis.

(iv) Periodically use the response of the RROM as initial estimate to run the full ROM to check the validity of the RROM and continue as long as the RROM predictions are accurate.

(v) If/when the RROM predictions are no longer accurate, i.e., the discrepancy between the ROM and RROM predictions in (iv) is too large, march the full ROM for a short time starting from a RROM estimate of the ROM solution.

Then, construct a new RROM based on the response of the full ROM in this period. Start marching this RROM.

(vi) Repeat (iv) and (v) until the end of the mission or the set of loading cases to be considered is exhausted.

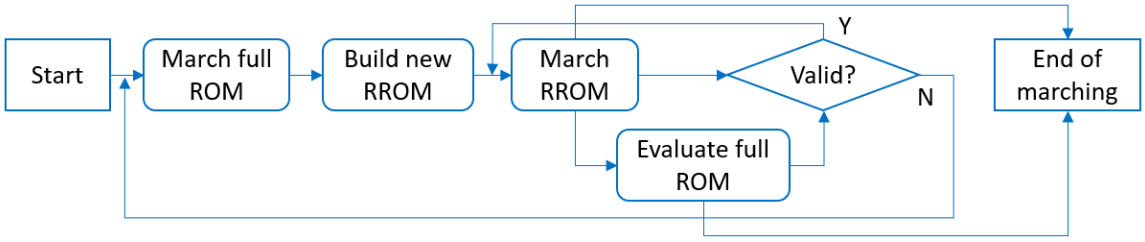

Figure 5.1. Flowchart of the RROM Construction and Adaptation Processes.

The above discussion has demonstrated the worth of RROMs to enhance the computational efficiency of large ROMs and thus warrants a deeper analysis of some of the key steps of the approach. Specifically, the next subsections will address the important questions of:

(i) restarting the ROM from an available RROM solution,

(ii) determining the time at which a RROM is no longer accurate enough and doing so without the knowledge of the full ROM solution,

(iii) selecting the number of POD eigenvectors in the RROM, and

(iv) selecting the length of data of full ROM for the construction of RROMs.

5.4.1. Restarting the full ROM

In seeking to implement the above procedure to the structural/thermal/aerodynamic response of the hypersonic panel of Fig. 3.12, it was first recognized that using the RROM solution to deduce the corresponding full ROM solution (not an estimate of it) is not possible in the given format. The challenge is that the thermal and structural

computations are staggered and thus there is no iteration taking place over the thermal and structural solution *together* to obtain the joint solution at one time. Thus, to obtain the full ROM thermal solution at one particular time step, one would require the full ROM thermal and structural solutions at the previous time step. Since neither is available, there does not appear a way to exactly get the full ROM thermal solution without marching from time $t = 0$. The same problem is encountered when trying to obtain the full ROM structural solution at one time step as the full ROM temperature distribution at that time is not known.

The best palliative is then to select the temperature and displacements at the time step just before restart as originating exactly from the RROM. The staggered marching then proceeds from this information and the ROM temperature field is obtained at the next step using the ROM deformations (which affect the temperature through the change in aerodynamics and thus in aero heating). The marching then continues leading to ROM based displacements and temperatures referred to here as the "approximate ROM solution". While this solution does not match the full ROM solution, which is marched since time $t = 0$, it is expected that it would converge back to it as the time after restart increases as long as the full ROM is stable in the neighborhood of these solutions. This is the case here as seen on Fig. 5.2 which shows the relative norm errors between the structural and thermal solutions obtained by the approximate ROM restarted at 76s, 156s, and 223s from 3 different RROMs (see below) and those obtained from the full ROM. It is seen that the error is indeed generally decreasing so that the approximate ROM solutions do indeed converge back to the full one.

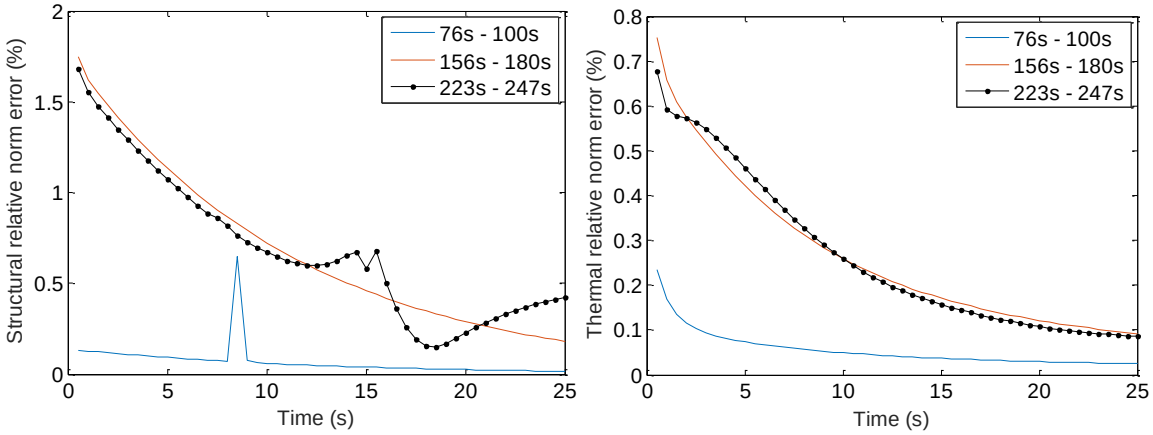

Figure 5.2. Relative Norm Errors Between 3 Approximate ROMs and the Full ROM. (a) Structural Error. (b) Thermal Error.

This convergence and the small levels of errors seen in Fig. 5.2 suggest that the approximate ROM may reflect well enough the physics in the problem to serve as appropriate data for the rotation/downsizing of the basis from ROM to RROM. To confirm this potential, the above adaptation process, see Fig. 5.1, was implemented with 4 RROMs each based on 25 seconds of full ROM (for the 1st RROM) or approximate ROM (for the other 3). The details of these RROMs are presented in Table 5.3 and shown in Fig. 5.3 are the predictions of typical structural deflection and temperature time histories obtained by the adaptive process and by the full ROM. Clearly, the matching is very good to excellent and these RROM provide a significant decrease in the computation effort: averaging the reductions in coefficients weighted by time span of validity yields an overall reduction by 93.6% over the 200s of RROM computations! If one factors in the full ROM computations (100s), the reduction is still by 62.4%, even though the adaptation has not been optimized.

Table 5.3. Adaptive RROM Validity and Cost Reduction.

Data Span (s)	Structural ROM orders	Thermal ROM order	Coeff. Reduction			Valid from (s)	Valid till (s)
			from M	from μ	both		
1-25	5+5+5	5	92.7	56.9	99.3	26	75
76-100	10+10+10	10	64.0	54.5	89.3	101	155
156-180	7+7+7	7	84.7	56.1	97.4	181	222
223-247	9+12+9	9	64.0	55.1	89.6	248	300

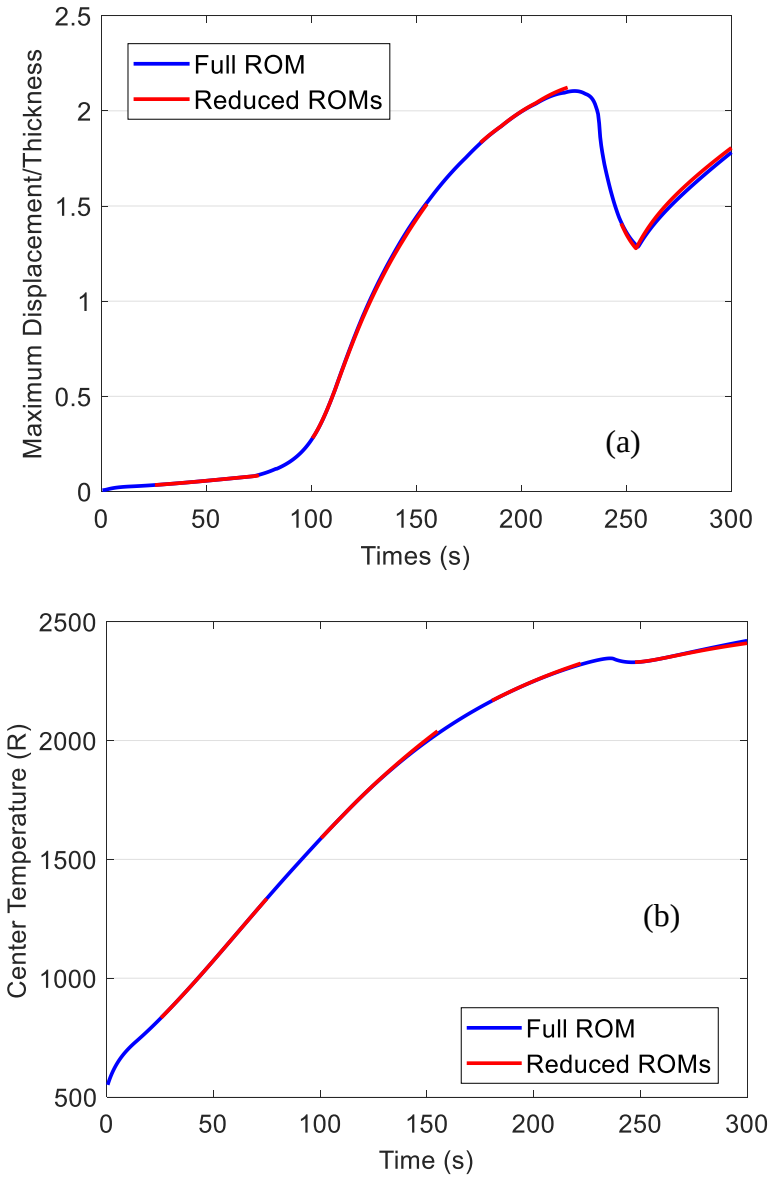

Figure 5.3. Predictions of (a) the Maximum Transverse Displacement and (b) the Temperature of the Panel Center by the Full ROM and the Reduced ROMs

5.4.2. Determining if the RROM is no longer valid

Since the above computations were only a first assessment of the adaptive RROM process, the assessment of the validity of the RROMs and the determination of the stop times of Table 5.3 was performed in comparison to the (available) full ROM predictions with the relative error, referred to as "full error", limited to 2.5% as discussed in connection with Tables 5.1 and 5.2. This is not appropriate for future applications because the full ROM predictions would in general not be available. Moreover, as discussed above, the staggering of the computations prevents obtaining them from the RROM solutions. However, based on the above discussion one can introduce two alternate error measures:

structural error: error between the structural RROM and approximate ROM predictions at a given time *t* with the temperature obtained from the RROM

thermal error: error between the thermal RROM and approximate ROM predictions at a given time *t* with the deformations obtained from the RROM.

Note that both of these errors are computed independently at each time *t*, there is no marching as is done when simulating data according to the approximate ROM.

Shown in Fig. 5.4 are the structural and thermal errors each corresponding to a particular RROM segment together with the corresponding full ROM errors. While the magnitudes of these two types of error are typically different, their behaviors are very similar, except for the oscillatory behavior of the thermal error. Most notably, both structural/thermal errors and their full counterparts grow steadily at approximately the same rate. This property enables the use of the thermal and structural errors as indicators of the accuracy of the RROM solutions to be used in future applications.

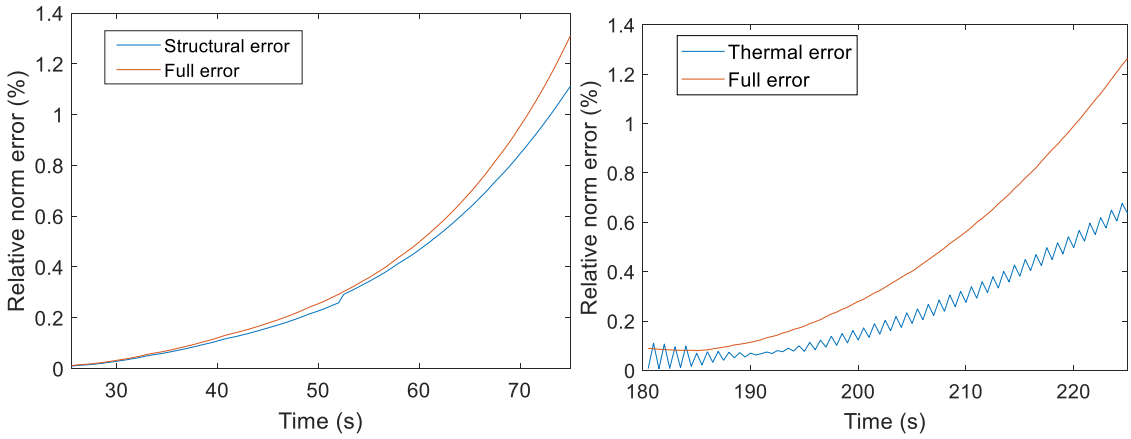

(a) (b)

Figure 5.4. Comparisons of the Structural and Thermal Errors to the Full Errors for Selected RROMs.

5.4.3. Selecting the length of data of full ROM and the number of POD eigenvectors

As observed from Section 5.3, there are two major factors affecting the length of time a RROM is valid. One of them is the number of solution snapshots of the full (or approximate as its best surrogate, see Section 5.4.1) ROM used to construct the reduced basis, the other is the number of modes selected into this basis. In the data of Table 5.3, these two factors were chosen rather arbitrarily to obtain some perspective on their influence. To achieve maximum computational efficiency, a formal strategy of these parameters needs to be devised. Clearly, with more full ROM snapshots the RROM is likely to have longer valid time, see Table 5.2, but this also implies a longer, computationally more expensive full ROM run. Similarly, with a larger basis the RROM would have longer valid time but would be costlier, see Table 5.1.

These trade-offs must be addressed and it is proposed here is to rely on an “average cost” for each full ROM – RROM period defined as

$$C_{avg} = \left(C_F L_F + C_R L_R\right) / \left(L_F + L_R\right) \tag{5.10}$$

where L_F and L_R are the length of time the full ROM and RROM are marched, and C_F and C_R are the cost per time step of the full ROM and RROM which can each be determined from

$$C = M^4 / 6 + M^2 \mu^2 / 4 \tag{5.11}$$

where M is the number of structural modes and μ is the number of thermal modes of either full ROM or RROM.

It is proposed here that the numbers of POD eigenvectors retained in the RROM and the length of full ROM data L_F be selected to minimize the average cost C_{avg}, Eq. (5.10) assuming that such a minimum occurs. To test this strategy and confirm the existence of a minimum, RROMs of different basis sizes were constructed using different approximate ROM data lengths from the time of 76s onward. The average cost is given in Table 5.4 for different RROM basis sizes for 25s of approximate ROM data. Moreover, shown in Table 5.5 are the average costs for various approximate ROM data lengths keeping the RROM basis sizes constant. Similar data is presented in Tables 5.6 and 5.7 using full ROM data starting from 1s onward. It appears from these tables that a minimum does indeed take place, and corresponds to the 10+10+10 structural-10 thermal modes RROM built from 25s of approximate ROM data for the 76s onward period while for the 1s onward period it is for the 7+7+7 structural-7 thermal modes RROM built from 15s of full ROM data. These numbers of modes and lengths of ROM data are consistent with the intuitive selection carried out earlier.

Table 5.4. Average Cost of Full ROM – RROM Period Starting from 76s Onward, 25s of Approximate ROM Data, Varying RROM Size.

RROM size	Valid for (s)	Average cost
5+5+5+5	13.5	9.6349E+05
6+6+6+6	23.5	7.7198E+05
7+7+7+7	24.5	7.6541E+05
8+8+8+8	21	8.3296E+05
9+9+9+9	26.5	7.7087E+05
10+10+10+10	54	5.7552E+05
11+11+11+11	62	5.8918E+05
12+12+12+12	68.5	6.3458E+05
13+13+12+13	68.5	6.9461E+05
14+14+12+14	73.5	7.5212E+05
15+15+12+15	74	8.3517E+05

Table 5.5. Average Cost of Full ROM – RROM Period Starting from 76s Onward, Varying Data Length Used

RROM size	11+11+11+11		10+10+10+10		9+9+9+9	
Data length (s)	Valid for (s)	Average cost	Valid for (s)	Average cost	Valid for (s)	Average cost
15	35.5	6.0125E+05	33.5	5.6604E+05	25.5	6.1264E+05
20	31.5	7.1520E+05	31	6.7552E+05	27.5	6.8233E+05
25	62	5.8918E+05	54	5.7552E+05	26.5	7.7087E+05
30	64	6.2885E+05	56	6.1830E+05	54	5.9445E+05

Table 5.6. Average Cost of Full ROM – RROM Period Starting from 1s Onward, 25s of Full ROM Data, Varying RROM Size.

RROM size	Valid for (s)	Average cost
3+3+3+3	18	8.6010E+05
4+4+4+4	42.5	5.5012E+05
5+5+5+5	49.5	5.0267E+05
6+6+6+6	65	4.2542E+05
7+7+7+7	65	4.3799E+05
8+8+8+8	67	4.4874E+05
9+9+9+9	67.5	4.7499E+05

Table 5.7. Average Costs of Full ROM – RROM Period Starting from 1s Onward, Varying Data Length Used

RROM size	5+5+5+5		6+6+6+6		7+7+7+7	
Data length (s)	Valid for (s)	Average cost	Valid for (s)	Average cost	Valid for (s)	Average cost
15	27.5	5.2818E+5	29.5	5.1189E+5	57.5	3.3588E+05
20	42	4.8359E+5	61.5	3.7821E+5	68.5	3.6338E+05
25	49.5	5.0267E+5	65	4.2542E+5	65	4.3799E+05
30	66	4.6879E+5	66	4.7605E+5	64	4.9760E+05

These observations indicate that beginning at a certain point in the trajectory, there exists an optimum combination of length of full ROM data and size of RROM that yields the lowest cost. A selection strategy of these optimum parameters can be performed as follows:

(i) march the full ROM or approximate ROM for a few time steps (7 – 10 seconds);

(ii) with Eqs. (5.1) – (5.5), build RROM basis functions of different sizes, determine the valid time of these RROMs and their average cost;

(iii) march the full ROM or approximate ROM for a little longer, e.g., 1 second;

(iv) with this longer data, build RROM basis functions of different sizes, determine the valid time of these RROMs and their average cost;

(v) compare (iv) with (ii), if the lowest average cost of (iv) is smaller than (ii), then iterate (iii) - (iv) and compare the result of the last two iterations, if the lowest average cost of last iteration is equal or larger than previous iteration, then

(vi) select the RROM with lowest cost in the current iteration to continue marching.

The key step in the above strategy is (ii) which would lead to a large cost if carried out as stated. What would be desired instead would be to estimate this time without running the RROM for the entire time span. It is suggested here to use, and more

specifically model, the representation error with respect to the response of the full ROM/approximate ROM to establish an estimator of the valid time.

Shown in Fig. 5.5 is the time history of the representation error in the transverse displacements of a 10 linear modes basis using the approximate ROM data in the period 76s – 100s, plotted after the end of this period. This curve was first approximated by a 6th order autoregressive model with quadratic, linear and constant exogenous terms using the first 15s of data, and the matching is very good until the required level, i.e., up to 155s which corresponds to 2.5% error in displacement (see the example in Section 5.4.1).

Plotted in Fig. 5.6 are the representation error and its corresponding approximation for the 8 linear modes basis RROM. Using this approximation to estimate the RROM valid time would lead to a 1 – 2 seconds error and in turn to a 1% – 2% of difference in average cost which is not significant. However, the quality of the approximation is not guaranteed in other cases, e.g., for the thermal representation error with 10 thermal modes, see Fig. 5.7. While the approximation obtained using the first 15s of data is not good, using the entire 55s of data would lead to a good fit. In fact, using simply a quadratic polynomial also gives good fit in most cases using the entire 55s of data. These findings suggest that:

(1) the errors grow closely to quadratically (or as a quadratic polynomial), especially after a "long" time, however, at the beginning there is a transient present,

(2) because of the transient, the modeling of the error using a quadratic polynomial is typically not very accurate if using only a short length of data at the beginning,

(3) the modeling of the transient using exponential terms, relying on an autoregressive modeling, often improves the matching but not always or not always significantly,

(4) the use of short data, e.g., a few seconds, at the beginning as a predictor of the curves would require the modeling of the transient in an appropriate functional form.

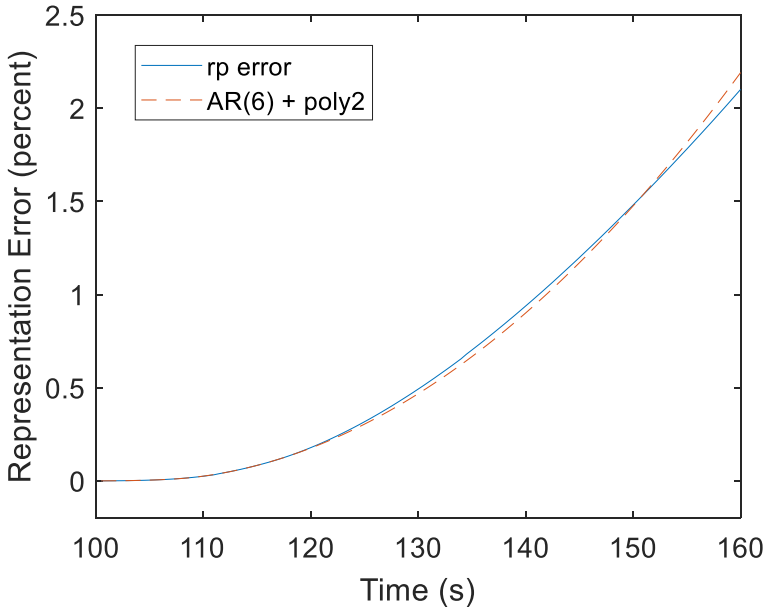

Figure 5.5. Linear Part Representation Error of a 10 Linear Mode Basis Built Using Approximate RROM Data from 76s – 100s, and the Curve Fit with 6th Order Autoregressive Model with Quadratic Terms.

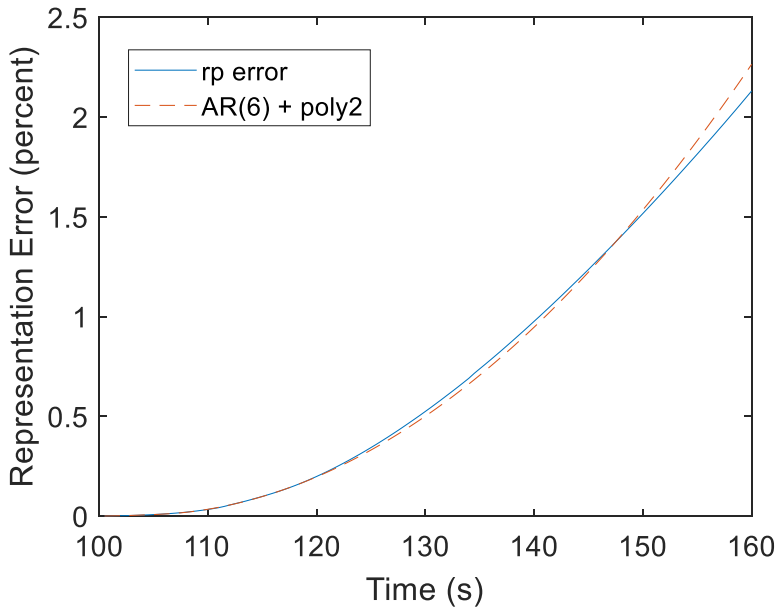

Figure 5.6. Linear Part Representation Error of an 8 Linear Mode Basis Built Using Approximate RROM Data from 76s – 100s, and the Curve Fit with 6th Order Autoregressive Model with Quadratic Terms.

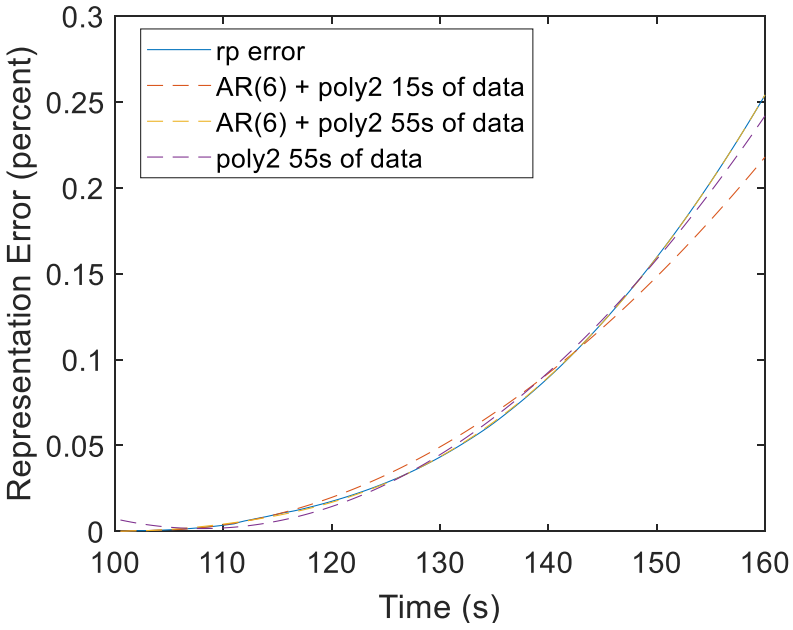

Figure 5.7. Thermal Representation Error of an 10 Thermal Mode Basis Built Using Approximate RROM Data from 76s – 100s; the Curve Fit with 6th Order Autoregressive Model with Quadratic Terms using 15s of data; and the Curve fit with Quadratic Polynomial Only Using 55s of Data.

An alternative approach to estimate the number of POD eigenvectors (and length of ROM data) would be to analyze the behavior of the error for different number of modes (and length of ROM data) to assess the difference in rates of growth of the error. Such a comparison is shown in Fig. 5.8 for the linear representation error with different number of POD eigenvectors plotted only over a short period after the RROM start, i.e., from 100s-110s. Seeking a model that has a "small" number of modes and a "slow" growth of the error would suggest the best choice is 8 linear modes in this case. A similar analysis for the dual representation error, see Fig. 5.9, suggests 10 dual modes as basis. These selections are close to the model built in Section 5.4.1, where a 10 linear, 10 dual, 10 thermal enrichment and 10 thermal modes basis was chosen as the best after several trials using different mode numbers. Based on this limited analysis, it is believed that the comparative analysis of short term data can be successfully used to select good approximate values of the number of basis functions to be used in the RROM.

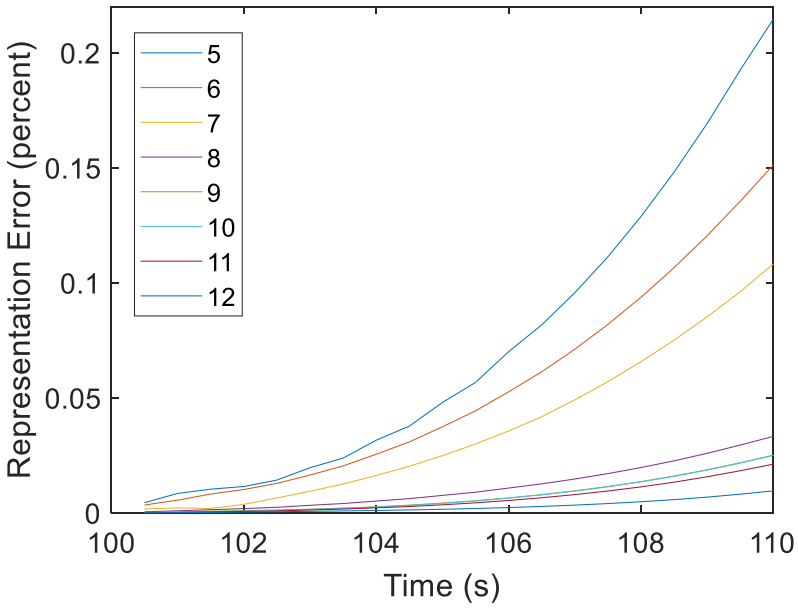

Figure 5.8. Growth of Linear Representation Error of Different Number of Modes.

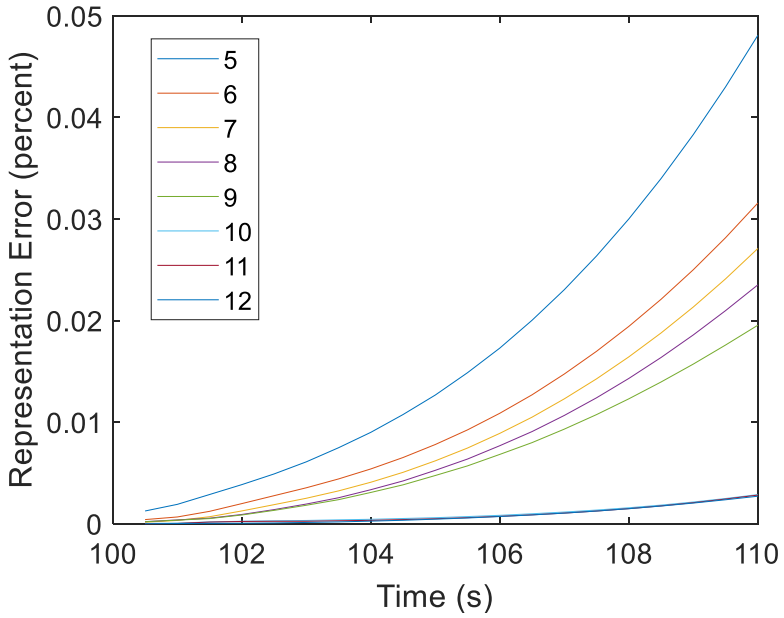

Figure 5.9. Growth of Dual Representation Error of Different Number of Modes.

6. SUMMARY

This proposal focuses primarily on the modeling of uncertainty in coupled structural-thermal models of heated structures and on its propagation to the response and temperature distribution. This effort is carried out at the level of reduced order models and finite element elemental matrices of both structural response and heat conduction using the maximum entropy framework/nonparametric approach first proposed by (Soize 2000).

6.1. Uncertainty Modeling of Structures with Localized Behavior at ROM Level

While the maximum entropy has been widely used and validated on many - mostly structural - problems, it had never been reported that its use leads to a globalization of the uncertain response when the mean model has a localized response. While this situation may be physically admissible, there are certainly situations in which one expects the uncertain response to be localized as well. This problem is especially relevant in the present context because heat conduction is prone to localization. Accordingly, an extension of the maximum entropy method was developed in Chapter 2 to address this issue. This Chapter also addressed the reverse problem of generating uncertain localized responses when the mean model response is global, as is observed in bladed disks due to mistuning.

A study of the eigenvalues/eigenvectors of the stiffness matrix of structures exhibiting localized responses showed that either their lowest eigenvalues are densely populated or their modes are strongly localized to the domain of the excitation. These observations suggested that the part (the “local” component) of the ROM stiffness matrix associated with these eigenvalues/eigenvectors be modeled separately from the rest of the

stiffness matrix (the "global" component) to maintain the localization. The stochastic modeling of the local and global components of the ROM stiffness matrix was achieved differently but both on the basis of the maximum entropy concepts leading to a 3-hyperparameter model. One of these hyperparameters, δ_G, controls the globalization of the uncertainty, another, δ_1, governs the level of uncertainty in the localized zone, and a third one, δ_L, controls the distortion of the response in the localized zone. This approach was successfully demonstrated on two structures: an annulus, which exhibits closely spaced eigenvalues of its stiffness matrix, and to a chain of oscillators for which the eigenvalues of the stiffness matrix are well separated but the eigenvectors are strongly localized. It was found that the hyperparameter δ_1 and its associated component of the stochastic model play a dominant role in the overall uncertainty of the response.

The second part of Chapter 2 focused on structures, e.g., bladed disks, for which the mean model exhibits global mode shapes while those of the uncertain structures are strongly localized. This behavior is often recognized as originating from closely spaced natural frequencies and triggered by uncertainty in specific parts of the structures, e.g., of the blades in bladed disks, which is challenging to implement within global ROMs of the entire structure. To model these effects, the local component of the ROM stiffness matrix associated with its closely spaced eigenvalues was mapped back to the finite element domain where the uncertainty was introduced. The application of this approach to a bladed disk finite element model demonstrated that the localization can indeed be produced and that it primarily results from the hyperparameter δ_L and its associated component of the stochastic model.

6.2. Thermal – Structural Uncertainty Modeling at ROM Level

Having extended the nonparametric method, Chapter 3 returned to the main focus of this effort, i.e., the modeling and assessment of uncertainty on thermal and structural properties on the temperature and response of heated structures. This study was conducted directly on coupled thermal-structural reduced order models using maximum entropy concepts to randomize the associated matrices. Moreover, nonlinear geometric effects were included in the structural ROM. The resulting analysis is thus carried out very efficiently as compared to a similar effort involving a modeling of uncertainty at the finite element model level.

The uncertainty on the conductance properties was considered first. Using a particular beam example, it was shown that the behavior of the temperature distribution may be strongly dependent on the boundary conditions, i.e., being localized near the applied flux or very global. Then, the simulation strategy chosen for the uncertain ROM conductance matrices is a recent extension of the nonparametric approach in which the local and global characters of the uncertainty on the temperature can be separately controlled. Accordingly, this approach is applicable to the various type of thermal boundary conditions. This uncertainty on the thermal properties was propagated to the nonlinear structural response by imposing the random temperature distributions on the panel. The results demonstrate a level of variability of the response that is similar to that of the temperature distributions.

The uncertainties on the structural, i.e., structural and thermal-structural coupling (thermal expansion) properties was considered next. It was shown that these uncertainties may indeed be modeled directly at the ROM level and both appear through the positive

definite matrix $\boldsymbol{K}_C$ of Eq. (3.18). Yet, the formulation permits the imposition of uncertainties on either property separately or together through their compounding in Eq. (3.29). Further, practical implementation details that appear when the mean ROM is identified from a black box finite element code were pointed out and resolved in a general setting. The application of these concepts to the beam example was finally performed and it was observed that a coefficient of variation around 0.6% of the key structural-thermal coupling terms led to a much increased variability, of the order of ±2.5%, of the structural response near its peak demonstrating a significant sensitivity of this response with respect to the coefficient of thermal expansion uncertainty. A similar sensitivity was also observed with respect to the structural only parameters of the model. Application example was also made in a panel with stiffeners under hypersonic airflow, the uncertainty modeling also suggests a large sensitivity of the response at higher Mach number with respect to uncertainties in elasticity tensor and coefficient of thermal expansion.

6.3. Maximum Entropy Structural-Thermal Uncertainty Modeling at the Finite Element Level

The maximum entropy uncertainty modeling, when associated with reduced order model, is very efficient computationally. As stated in Chapter 1, it permits to introduce aleatoric as well as some epistemic uncertainty in to the model, which is a desirable feature in uncertainty modeling of hypersonic vehicles. However, as demonstrated in Chapter 2 for localized responses, the introduction of epistemic uncertainty at the global ROM level main affect features of the solution. While the strategy to maintain particular properties on the random ROM *matrices* is clear in the maximum entropy strategy, it is

much more difficult to maintain particular features of the ROM *solution*. As demonstrated in Chapter 2, this difficulty is rooted, at least in part, with the level i.e., global ROM, at which the epistemic uncertainty is introduced.

Accordingly, a new approach was introduced and first validated in Chapter 4 in which uncertainty is introduced at the elemental level of finite element models of heated linear structures. A key feature of the approach is that the elemental stiffness matrix and thermal force vector are simulated *jointly* to respect the dependence of both of them on the elasticity properties of the structure. Following the maximum entropy approach, the method produces samples of these elemental matrices and vectors given their mean and two sets of parameters that describe (i) the overall level of uncertainty (structural and thermal separately) and (ii) the correlation of the structural and coefficient of thermal expansion properties, separately, across the structure. Owing to the use of the maximum entropy approach, the proposed modeling strategy accounts for aleatoric and some epistemic uncertainty of both types of material properties. The ease of application of the method was demonstrated on a first example.

6.4. Nonlinear Reduced ROMs

While the ROMs are much more efficient than full finite element model solutions, they can still be computationally expensive especially when facing aero-thermal-structural coupled problems. This cost is of course further heightened when propagating uncertainties using Monte-Carlo simulations. The focus of the proposed investigation in Chapter 5 was on the development and first validation of a data-driven reduction process of structural-thermal ROMs into “reduced ROMs” (RROMs) of much smaller but potentially evolving bases that lead to predictions of the structural response

and temperature with an accuracy similar to that of the original, “full”, ROMs at a much reduced computational cost. A dedicated process centered around Proper Orthogonal Decompositions (POD) was formulated to extract dominant eigenvectors of the various types of basis functions (linear and dual modes, thermal enrichments, and thermal basis functions). This process was validated on a representative hypersonic panel problem and significant reductions of the structural and thermal bases, especially of the latter, were observed. Moreover, these reductions in bases led to significant decreases of the number of coefficients in the model and correspondingly of the computational effort, between 62% and 94% reduction in computations.

It was noted that a RROM may not be valid for the entire range of load level/trajectory thereby leading to the need to adapt the RROMs. The key questions of how large the RROM basis should be to optimize the RROM computational benefit and of the determination of the time/loading condition at which to adapt were discussed and strategies to resolve them proposed. The validation of this RROM methodology was critically and successfully performed on the coupled structural-thermal-aerodynamic response of a representative hypersonic panel.

REFERENCES

Batou, A., and Soize, C. 2012. Rigid multibody system dynamics with uncertain rigid bodies. *Multibody System Dynamics* Vol. 27 (No. 3): 285-319.

Bladh, R., Castanier, M. P., and Pierre, C. 2001 Component-mode-based reduced order modeling techniques for mistuned bladed disks- part II: application. *Journal of Engineering for Gas Turbines and Power* Vol. 123 (No. 1): 100-108.

Capiez-Lernout, E., Soize, C., and Mignolet, M.P. 2014. Post-buckling nonlinear static and dynamical analyses of uncertain cylindrical shells and experimental validation. *Computer Methods in Applied Mechanics and Engineering* Vol. 271: 210-230.

Culler, A.J., and McNamara, J.J. 2011. Impact of fluid-thermal-structural coupling on response prediction of hypersonic skin panels. *AIAA Journal* Vol. 49: 2393-2406.

Durand, J.-F., Soize, C., and Gagliardini, L. 2008. Structural-acoustic modeling of automotive vehicles in presence of uncertainties and experimental identification and validation. *Journal of the Acoustical Society of America* Vol. 124 (No. 3): 1513-1525.

Falkiewicz, N.J. and Cesnik, C.E.S. 2011. Proper orthogonal decomposition for reduced-order thermal solution in hypersonic aerothermoelastic simulations. *AIAA Journal* Vol. 49, No. 5.

Ghanem, R. and Spanos, P.D. 1991. *Stochastic Finite Elements: A Spectral Approach*. New York: Springer-Verlag.

Gogulapati, A., Brouwer, K., Wang, X.Q., Murthy, R., McNamara, J.J. and Mignolet, M.P. 2017. Full and reduced order aerothermoelastic modeling of built-up aerospace panels in high-speed flows. Pr*oceedings of the AIAA Science and Technology Forum and Exposition (SciTech2017)*. Dallas, Texas. Jan. 9-13. AIAA Paper AIAA 2017-0180.

Gogulapati, A., Deshmukh, R., Crowell, A.R., McNamara, J.J., Vyas, V., Wang, X.Q., Mignolet, M.P., Beberniss, T., Spottswood, S.M. and Eason, T.G. 2014. Response of a panel to shock impingement: modeling and comparison with experiments, *Proceedings of the AIAA Science and Technology Forum and Exposition (SciTech2014).* National Harbor, Maryland. Jan. 13-17. AIAA Paper AIAA 2014-0148.

Gogulapati, A., Deshmukh, R., McNamara, J.J., Vyas, V., Wang, X.Q., Mignolet, M.P., Beberniss, T., Spottswood, S.M. and Eason, T.G. 2015. Response of a panel to shock impingement: modeling and comparison with experiments - part 2.

Proceedings of the AIAA Science and Technology Forum and Exposition (SciTech2015). Orlando, Florida. Jan. 5-9. AIAA Paper AIAA 2015-0685.

Hollkamp, J.J., Gordon, R.W., Spottswood, S.M. 2005. Nonlinear modal models for sonic fatigue response prediction: a comparison of methods. *Journal of Sound and Vibration* Vol. 284: 1145 - 1163.

Kim, K., Khanna, V., Wang, X.Q. and Mignolet, M.P. 2009. Nonlinear reduced order modeling of flat cantilevered structures, *Proceedings of the 50th Structures, Structural Dynamics, and Materials Conference*. Palm Springs, California. May. AIAA-2009-2492.

Kim, K., Radu, A.G., Wang, X.Q., and Mignolet, M.P. 2013. Nonlinear reduced order modeling of isotropic and functionally graded plates. *International Journal of Non-Linear Mechanics* Vol. 49: 100-110.

Matney, A., Mignolet, M.P., Culler, A.J., McNamara, J.J., and Spottswood, S.M. 2015. Panel response prediction through reduced order models with application to hypersonic aircraft. *Proceedings of the AIAA Science and Technology Forum and Exposition (SciTech2015)*. Orlando, Florida. Jan. 5-9. AIAA 2015-1630.

Matney, A.K., Mignolet, M.P., Spottswood, S.M., Culler, A.J., McNamara, J.J. 2014. Thermal reduced order model adaptation to aero-thermo-structural interactions. *Proceedings of the AIAA Science and Technology Forum and Exposition (SciTech2014)*. National Harbor, Maryland. Jan. 13-17. AIAA 2014-0493

Matney, A.K., Perez, R.A., and Mignolet, M.P., 2011. Nonlinear unsteady thermos-elastodynamic response of a panel subjected to an oscillating flux by reduced order models. *Proceedings of the 52nd Structures, Structural Dynamics and Materials Conference.* Denver, Colorado. Apr. 4-7. AIAA 2011-2016.

Matney, A., Spottswood, S.M. and Mignolet, M.P. 2012. Nonlinear structural reduced order modeling methods for hypersonic structures. *Proceedings of the 53rd Structures, Structural Dynamics and Materials Conference*. Honolulu, Hawaii. April. AIAA-1972.

McEwan, M.I., Wright, J.R., Cooper, J.E., Leung, A.Y.T. 2001. A combined modal/finite element analysis technique for the dynamic response of a non-linear beam to harmonic excitation. *Journal of Sound and Vibration* Vol. 243 (4): 601-624.

Mignolet, M.P., Przekop, A., Rizzi, S.A., and Spottswood, S.M. 2013 A review of indirect/non-intrusive reduced order modeling of nonlinear geometric structures. *Journal of Sound and Vibration* Vol. 332: 2437-2460.

Mignolet, M.P., Radu, A.G., and Gao, X. 2003. Validation of Reduced Order Modeling for the Prediction of the Response and Fatigue Life of Panels Subjected to Thermo-Acoustic Effects, *Proceedings of the 8th International Conference on Recent Advances in Structural Dynamics*. Southampton, United Kingdom. Jul. 14-16.

Mignolet, M.P., and Soize, C. 2008. Nonparametric stochastic modeling of linear systems with prescribed variance of several natural frequencies. *Probabilistic Engineering Mechanics* Vol. 23: 267-278.

Mignolet, M.P., and Soize, C. 2008. Stochastic reduced order models for uncertain geometrically nonlinear dynamical systems. *Computer Methods in Applied Mechanics and Engineering* Vol. 197: 3951-3963.

Muravyov, A.A. and Rizzi, S.A. 2003. Determination of nonlinear stiffness with application to random vibration of geometrically nonlinear structures. *Computers and Structures* Vol. 81: 1513-1523.

Murthy, R., Mignolet, M.P., and El-Shafei, A. 2010. nonparametric stochastic modeling of structural uncertainty in rotordynamic systems: part I – formulation. *Journal of Engineering for Gas Turbines and Power* Vol. 132.

Murthy, R., Mignolet, M.P., and El-Shafei, A. 2010. Nonparametric stochastic modeling of structural uncertainty in rotordynamic systems: part II – applications. *Journal of Engineering for Gas Turbines and Power* Vol. 132.

Murthy, R., Tomei, J., Wang, X.Q., Mignolet, M.P., and El-Shafei, A. 2014. Nonparametric stochastic modeling of structural uncertainty in rotordynamics: unbalance and balancing aspects. *Journal of Engineering for Gas Turbines and Power* Vol. 136 (No. 6): 062506-1 - 062506-12.

Murthy, R., Wang, X.Q., Matney, A., and Mignolet, M.P. 2016. Optimum thermal modes for coupled structural - thermal reduced order models. *Proceedings of the AIAA Science and Technology Forum and Exposition (SciTech2016)*. San Diego, California. Jan. 4-8. AIAA 2016-1709.

Ohayon, R., and Soize, C. 2014. *Advanced computational vibroacoustics - reduced-order models and uncertainty quantification*. New York: Cambridge University Press.

Przekop, A., Guo, X., Rizzi, S.A. 2012. Alternative modal basis selection procedures for nonlinear random response simulation. *Journal of Sound and Vibration* Vol. 331: 4005-4024.

Przekop, A., Rizzi, S.A. 2006. Nonlinear acoustic response of an aircraft fuselage sidewall structure by a reduced-order analysis. *Proceedings of the 9th International Conference on Recent Advances in Structural Dynamics*. Southampton, UK. July 17-19.

Przekop, A., Rizzi, S.A. 2006. Nonlinear reduced order finite element analysis of structures with shallow curvature. *AIAA Journal* Vol. 44: 1767-1778.

Przekop, A., Rizzi, S.A. 2007. Dynamic snap-through of thin-walled structures by a reduced-order method. *AIAA Journal* Vol. 45: 2510-2519.

Perez, R., Wang, X.Q. and Mignolet, M.P. 2010. Steady and unsteady nonlinear thermoelastodynamic response of panels by reduced order models, *Proceedings of the 51st Structures, Structural Dynamics, and Materials Conference*. Orlando, Florida. April. AIAA-2010-2724.

Perez, R., Wang, X.Q. and Mignolet, M.P. 2011. Nonlinear reduced order models for thermoelastodynamic response of isotropic and FGM panels. *AIAA Journal* Vol. 49: 630-641.

Perez, R., Wang, X.Q. and Mignolet, M.P. 2014. Non-intrusive structural dynamic reduced order modeling for large deformations: enhancements for complex structures. *Journal of Computational and Nonlinear Dynamics* Vol. 9 (No. 3): 031008-1 - 031008-12.

Perez, R., Wang, X.Q. and Mignolet, M.P. 2014. Prediction of displacement and stress fields of a notched panel with geometric nonlinearity by reduced order modeling, *Journal of Sound and Vibration* Vol. 333: 6572-6589.

Richter, L.A., and Mignolet, M.P. 2017. Stochastic modeling of uncertain mass characteristics in rigid body dynamics. *Mechanical Systems and Signal Processing* Vol. 87: 43-53.

Rizzi, S.A., Przekop, A. 2008. System identification-guided basis selection for reduced-order nonlinear response analysis. *Journal of Sound and Vibration* Vol. 315: 467-485.

Sankar, T.S., Ramu, S.A. and Ganesan, R. 1993. Stochastic finite element analysis for high speed rotors, *J. Vib. Acoust.* Vol. 115 (1): 59–64.

Sarrouy, E., Dessombz, O. and Sinou, J.-J. 2012. Stochastic analysis of the eigenvalue problem for mechanical systems using polynomial chaos expansion – application to a finite element rotor, *J. Vib. Acoust.* Vol. 134(5): 051009.

Schenk, C. and Schuëller, G. 2003. Buckling analysis of cylindrical shells with random geometric imperfections. *Int. J. Nonlinear Mech.* Vol. 38(7): 1119–1132.

Schenk, C. and Schuëller, G. 2007 Buckling analysis of cylindrical shells with cutouts including random boundary and geometric imperfections. *Comput. Methods Appl. Mech. Eng.* Vol. 196(35–36): 3424–3434.

Soize, C. 2000. A nonparametric model of random uncertainties for reduced matrix models in structural dynamics. *Probabilistic Engineering Mechanics* Vol. 15: 277-294.

Soize, C. 2006. Non-Gaussian positive-definite matrix-valued random fields for elliptic stochastic partial differential operators. *Computer Methods in Applied Mechanics and Engineering* Vol. 195: 26-64.

Soize, C. 2012. *Stochastic models of uncertainties in computational mechanics*. Reston, VA: American Society of Civil Engineers (ASCE).

Soize, C. 2017. *Uncertainty quantification: an accelerated course with advanced applications in computational engineering*. Cham, Switzerland: Springer.

Soize, C., and Chebli, H. 2003. Random uncertainties model in dynamic substructuring using a nonparametric probabilistic model. *Journal of Engineering Mechanics* Vol. 129 (No. 4): 449-457.

Soize, C., Poloskov, I.E. 2012. Time-domain formulation in computational dynamics for linear viscoelastic media with model uncertainties and stochastic excitation. *Computers and Mathematics with Applications* Vol. 64 (No. 11): 3594-3612.

Song, P., Matney, A., Murthy, R., Wang, X.Q., and Mignolet, M.P. 2016. Probabilistic modeling of thermal properties of hot structures and its propagation to the nonlinear geometric structural response. *Probabilistic Mechanics and Reliability Conference PMC 2016.* Nashville, Tennessee. May 23-25.

Song, P. and Mignolet, M.P. 2018. Maximum Entropy-Based Uncertainty Modeling at the Finite Element Level. *Proceedings of the AIAA Science and Technology Forum and Exposition (SciTech2018).* Kissimmee, Florida, Jan. 8-12. AIAA Paper AIAA-1657.

Song, P. and Mignolet, M.P. 2018. Reduced order model-based uncertainty modeling of structures with localized response. *Probabilistic Engineering Mechanics* Vol. 51:42-55.

Song, P., Wang, X.Q., Matney, A., Murthy, R., Mignolet, M.P. 2017. Nonlinear geometric thermoelastic response of structures with uncertain thermal and structural properties. *Proceedings of the AIAA Science and Technology Forum and Exposition (SciTech2017).* Dallas, Texas, Jan. 9-13. AIAA Paper AIAA 2017-0181.

Spottswood, S.M. and Allemang, R.J. 2007. On the investigation of some parameter identification and experimental modal filtering issues for nonlinear reduced order models. *Experimental Mechanics* Vol. 47: 511–521.

Wang, X.Q., Lin, J., Wainwright, B.A. and Mignolet, M.P. 2019. Multiple-Level Identification of Stiffness Coefficients in Nonlinear Reduced Order Modeling, *Proceedings of the International Modal Analysis Conference, IMAC XXXVII*. Orlando, Florida. Jan. 28-31.

Wang, X.Q., Mignolet, M.P., and Soize, C. 2018. Nonlinear Geometric Modeling of Uncertain Structures through Nonintrusive Reduced Order Modeling. *Proceedings of the Eighth International Conference on Computational Stochastic Mechanics*. Paros, Greece, Jun. 10-13.

Wang, X.Q., Phlipot, G.P., Perez, R.A. and Mignolet, M.P. 2018. Locally enhanced reduced order modeling for the nonlinear geometric response of structures with defects. *International Journal of Non-Linear Mechanics* Vol. 101: 1-7.

Wang, Y., Wang, X.Q. and Mignolet, M.P. 2018. Component-centric reduced order modeling for the prediction of the nonlinear geometric response of a part of a stiffened structure. *Journal of Computational and Nonlinear Dynamics* Vol. 13: 121006-1 – 121006-12.

APPENDIX A

ROM COEFFICIENTS WHEN CTE IS LINEARLY DEPENDENT ON TEMPERATURE

When the coefficient of thermal expansion depends linearly on temperature, Eq. (1.7) is replaced by (Matney Et al 2011)

$$M_{ij}\ddot{q}_j + D_{ij}\dot{q}_j + \left[K_{ij}^{(1)} + K_{ijl}^{(th)}\tau_l + K_{ijlp}^{(th)}\tau_l\tau_p \right] q_j + K_{ijl}^{(2)} q_j q_l + K_{ijlp}^{(3)} q_j q_l q_p = F_i + F_{il}^{(th)}\tau_l + F_{ilp}^{(th)}\tau_l\tau_p \tag{A.1}$$

where

$$K_{mnp}^{(th)} = \int_{\Omega_0} \frac{\partial U_i^{(m)}}{\partial X_k} \frac{\partial U_i^{(n)}}{\partial X_j} C_{jklr}\, \alpha_{lr}^{(0)}\, T^{(p)}\, d\boldsymbol{X} \tag{A.2}$$

$$K_{mnps}^{(th)} = \int_{\Omega_0} \frac{\partial U_i^{(m)}}{\partial X_k} \frac{\partial U_i^{(n)}}{\partial X_j} C_{jklr}\, \alpha_{lr}^{(1)}\, T^{(p)} T^{(s)}\, d\boldsymbol{X} \tag{A.3}$$

and

$$F_{mn}^{(th)} = \int_{\Omega_0} \frac{\partial U_i^{(m)}}{\partial X_k} C_{iklr}\, \alpha_{lr}^{(0)}\, T^{(n)}\, d\boldsymbol{X} \tag{A.4}$$

$$F_{mnp}^{(th)} = \int_{\Omega_0} \frac{\partial U_i^{(m)}}{\partial X_k} C_{iklr}\, \alpha_{lr}^{(1)}\, T^{(n)} T^{(p)}\, d\boldsymbol{X}\,. \tag{A.5}$$

In these equations, it was assumed that

$$\alpha_{lr}(\boldsymbol{X}) = \alpha_{lr}^{(0)} + \alpha_{lr}^{(1)} T(\boldsymbol{X}) = \alpha_{lr}^{(0)} + \alpha_{lr}^{(1)} T^{(p)}(\boldsymbol{X})\tau_p\,. \tag{A.6}$$

With Eq. (A.6), Eq. (3.14) becomes

$$E_C = \int_{\Omega_0} \left(w_m \frac{\partial U_i^{(m)}}{\partial X_j} + v_I\, Z_{ij}^{(I)} + z_m\, \alpha_{ij}^{(0)} T^{(m)} + \rho_I\, \alpha_{ij}^{(1)} Y^{(I)} \right) C_{ijkl} \left(w_n \frac{\partial U_k^{(n)}}{\partial X_l} + v_J\, Z_{kl}^{(J)} + z_n\, \alpha_{kl}^{(0)} T^{(n)} + \rho_J\, \alpha_{kl}^{(1)} Y^{(J)} \right) d\boldsymbol{X} \tag{A.7}$$

where

$$Y^{(I)} = T^{(m)} T^{(p)} \qquad \text{with} \qquad I = (m\text{-}1)\,\mu + p. \tag{A.8}$$

Since E_C is still positive for all w_m, v_I, z_m, and ρ_I, it is concluded by expanding that the matrix $\boldsymbol{K}_D$ defined as

$$\boldsymbol{K}_D = \begin{bmatrix} \boldsymbol{K}^{(1)} & \tilde{\boldsymbol{K}}^{(2)} & \boldsymbol{F}^{(th)} & \boldsymbol{F}_2^{(th)} \\ \tilde{\boldsymbol{K}}^{(2)T} & 2\tilde{\boldsymbol{K}}^{(3)} & \tilde{\boldsymbol{K}}^{(th)} & \tilde{\boldsymbol{K}}_2^{(th)} \\ \boldsymbol{F}^{(th)T} & \tilde{\boldsymbol{K}}^{(th)T} & \boldsymbol{K}^{(tt)} & \boldsymbol{K}_2^{(tt)} \\ \boldsymbol{F}_2^{(th)T} & \tilde{\boldsymbol{K}}_2^{(th)T} & \boldsymbol{K}_2^{(tt)T} & \boldsymbol{K}_3^{(tt)} \end{bmatrix} \tag{A.9}$$

is positive definite. In this matrix,

$$\left[\boldsymbol{F}_2^{(th)}\right]_{mJ} = F_{mnp}^{(th)} \qquad \text{with} \qquad J = (m\text{-}1)\,\mu + p \tag{A.10}$$

and

$$\left[\tilde{\boldsymbol{K}}_2^{(th)}\right]_{IJ} = K_{mnps}^{(th)} \quad \text{with } I = (m\text{-}1)\,\mu + n \quad \text{and} \quad J = (p\text{-}1)\,\mu + s. \tag{A.11}$$

Moreover, the elements of the matrix $\boldsymbol{K}^{(tt)}$ are still given by Eq. (3.17) but with α replaced by $\alpha^{(0)}$. Further, one also obtains

$$\left[\boldsymbol{K}_2^{(tt)}\right]_{mJ} = \int_{\Omega_0} \alpha_{jk}^{(0)} T^{(m)} C_{jklr}\, \alpha_{lr}^{(1)} T^{(n)} T^{(p)}\, d\boldsymbol{X} \quad \text{with} \quad J = (n\text{-}1)\,\mu + p \tag{A.12}$$

and

$$\left[\boldsymbol{K}_3^{(tt)}\right]_{IJ} = \int_{\Omega_0} \alpha_{jk}^{(1)} T^{(m)} T^{(n)} C_{jklr}\, \alpha_{lr}^{(1)} T^{(p)} T^{(s)}\, d\boldsymbol{X} \tag{A.13}$$

with $I = (m\text{-}1)\,\mu + n$ and $J = (p\text{-}1)\,\mu + s$.

Having established the necessary positive definiteness property, it remains to discuss the potential to identify the coefficients from finite element runs. Since $K_{ijlp}^{(th)}$ and $F_{ilp}^{(th)}$ multiply a product of two τ values, it is not possible to identify them directly if *p* and *l* are different. Specifically, one has

$$\bar{K}_{ijlp}^{(th)} = K_{ijlp}^{(th)} + K_{ijpl}^{(th)} \quad \text{and} \quad \bar{F}_{ilp}^{(th)} = F_{ilp}^{(th)} + F_{ipl}^{(th)} \quad p > l \tag{A.14}$$

but

$$\bar{K}_{ijll}^{(th)} = K_{ijll}^{(th)} \quad \text{and} \quad \bar{F}_{ill}^{(th)} = F_{ill}^{(th)}. \tag{A.15}$$

However, it is seen from Eq. (A.3) and (A.5) that the coefficients $K_{ijlp}^{(th)}$ and $F_{ilp}^{(th)}$ are symmetric with respect to their last two indices and thus from Eq. (A.14)

$$K_{ijlp}^{(th)} = K_{ijpl}^{(th)} = \frac{1}{2}\bar{K}_{ijlp}^{(th)} \quad \text{and} \quad F_{ilp}^{(th)} = F_{ipl}^{(th)} = \frac{1}{2}\bar{F}_{ilp}^{(th)} \quad p > l \tag{A.16}$$

The identification of the $\boldsymbol{K}_2^{(tt)}$ and $\boldsymbol{K}_3^{(tt)}$ has not been attempted since this effort was not successful for the simpler terms in $\boldsymbol{K}^{(tt)}$. Accordingly, $\boldsymbol{K}_2^{(tt)}$ and $\boldsymbol{K}_3^{(tt)}$ together with $\boldsymbol{K}^{(tt)}$ will be selected based on the maximization of the entropy leading, see Appendix C, to the corresponding block of the Cholesky decomposition being the identity matrix.

APPENDIX B

PROCEDURE TO MAKE $\boldsymbol{K}_B$ POSITIVE DEFINITE

As stated in the main text, the process to render the matrix $\boldsymbol{K}_B$ positive definite was achieved in (Wang et al 2018)

(a) without affecting the part of $\boldsymbol{K}_B$ that is positive definite, e.g., the linear stiffness matrix $\boldsymbol{K}^{(1)}$, and

(b) inducing the smallest changes possible to this matrix.

The condition (a) has been achieved iteratively by constructing the biggest block of the original matrix $\boldsymbol{K}_B$ that is positive definite. This block is at least of size M since the linear stiffness matrix $\boldsymbol{K}^{(1)}$ is positive definite. Accordingly, the top left block of $\boldsymbol{K}_B$ of size M+1 is first considered and it is checked for positive definiteness (e.g., by constructing its Cholesky decomposition). If it is positive definite, the algorithm moves to the top left block of size M+2 and the process is repeated.

Otherwise, a permutation of the rows and columns M+1 and M+2 is performed. If the top left block of size M+1 is now positive definite, the algorithm accepts the permutation and moves forward to the top left block of size M+2. On the contrary, the permutation between rows M+1 and M+2 is reversed and a permutation of rows M+1 and M+3 is performed followed by a positive definiteness check. This process concludes when no permutation of rows and columns achieves an increase in the size of the top left block of $\boldsymbol{K}_B$ which is positive definite.

At that point, the matrix $\boldsymbol{K}_B$ has been transformed in a symmetric matrix $\tilde{\boldsymbol{K}}_B$ which has the form

$$\tilde{\boldsymbol{K}}_B = \begin{bmatrix} \boldsymbol{K}_{11} & \boldsymbol{K}_{12} \\ \boldsymbol{K}_{12}^T & \boldsymbol{K}_{22} \end{bmatrix} \tag{B.1}$$

where $\boldsymbol{K}_{11}$ is positive definite and of size N_p, $\boldsymbol{K}_{12}$ is of size $N_p \times N_r$, and $\boldsymbol{K}_{22}$ is of size $N_r \times N_r$ where $N_r = M^2 + M - N_p$.

The task (b) above then proceeds with replacing the matrix $\tilde{\boldsymbol{K}}_B$ by

$$\hat{\boldsymbol{K}}_B = \begin{bmatrix} \boldsymbol{K}_{11} & \boldsymbol{K}_{12} \\ \boldsymbol{K}_{12}^T & \boldsymbol{K}_{22} \end{bmatrix} + \begin{bmatrix} \boldsymbol{0} & \Delta_1 \\ \Delta_1^T & \Delta_2 \end{bmatrix} = \tilde{\boldsymbol{K}}_B + \boldsymbol{\Delta} \qquad \text{(B.2)}$$

where the matrix $\boldsymbol{\Delta}$ will be selected to have the minimum Frobenius norm under the constraint that $\hat{\boldsymbol{K}}_B$ is at least positive semidefinite. The solution of this nonlinear optimization problem will be obtained iteratively through a sequence of linear optimization problems in which the positive definiteness constraint is enforced linearly. This process leads at iteration *m* to (Wang et al 2018)

$$\Delta_1 = \sum_{\tilde{\lambda}_i < 0} \mu_i \, \tilde{\boldsymbol{\psi}}_i^{(1)} \left[\tilde{\boldsymbol{\psi}}_i^{(2)} \right]^T, \quad \Delta_2 = \sum_{\tilde{\lambda}_i < 0} \mu_i \, \tilde{\boldsymbol{\psi}}_i^{(2)} \left[\tilde{\boldsymbol{\psi}}_i^{(2)} \right]^T \qquad \text{(B.3),(B.4)}$$

where $\tilde{\boldsymbol{\psi}}_i$ and $\tilde{\lambda}_i$ are the eigenvalues of the matrix $\boldsymbol{K}_B$ at iteration *m*. Moreover, the eigenvectors are partitioned into vectors $\tilde{\boldsymbol{\psi}}_i^{(1)}$ and $\tilde{\boldsymbol{\psi}}_i^{(2)}$ of N_p and N_r components, respectively. That is, $\tilde{\boldsymbol{\psi}}_i^T = \left[\left[\tilde{\boldsymbol{\psi}}_i^{(1)} \right]^T \left[\tilde{\boldsymbol{\psi}}_i^{(2)} \right]^T \right]$. Finally, the coefficients μ_i are solutions of the linear system of equations

$$\sum_{\tilde{\lambda}_r < 0} \left(2 a_{ri} \, b_{ri} + b_{ri}^2 \right) \mu_r = -\tilde{\lambda}_i \quad \text{with} \quad a_{rs} = \left[\tilde{\boldsymbol{\psi}}_r^{(1)} \right]^T \tilde{\boldsymbol{\psi}}_s^{(1)} \quad \text{and} \quad b_{rs} = \left[\tilde{\boldsymbol{\psi}}_r^{(2)} \right]^T \tilde{\boldsymbol{\psi}}_s^{(2)} \qquad \text{(B.5)}$$

Solving the linear system of equations (B.5) yields the values of the coefficients μ_i which can then be reintroduced in Eq. (B.3) and (B.4) to yield the unknown partitions Δ_1 and Δ_2 of Δ.

The resulting matrix $\hat{\boldsymbol{K}}_B$ will then in general not be positive definite but the process can be repeated with a new $\tilde{\boldsymbol{K}}_B = \hat{\boldsymbol{K}}_B$ until a matrix $\hat{\boldsymbol{K}}_B$ positive definite/semidefinite is finally obtained. At that point, the rows/columns permutations performed to obtain the largest block positive definite are reversed leading to a matrix $\boldsymbol{K}'_B$ which is positive definite and thus could serve as the basis for the structural uncertainty modeling.

In principle, achieving the positive definiteness of the structural only component of the matrix $\boldsymbol{K}_C$ (i.e., $\boldsymbol{K}_B$) is sufficient to enable the stochastic modeling process as defined in Eqs (3.19)-(3.22). Unfortunately, barely achieving positive definiteness or semidefiniteness induces ill conditioning in the propagation of the uncertainty to the structural-thermal matrices of the model. Indeed, if $\boldsymbol{K}_B$ is singular, then so is $\bar{\boldsymbol{L}}_{SS}^{(3)}$ (see Eq. (3.21) and it is not possible to determine $\bar{\boldsymbol{L}}_{TS}^{(2)}$ which should satisfy (see Eq. (3.19) and (3.21))

$$\bar{\boldsymbol{L}}_{SS}^{(2)}\,\bar{\boldsymbol{L}}_{TS}^{(1)T} + \bar{\boldsymbol{L}}_{SS}^{(3)}\,\bar{\boldsymbol{L}}_{TS}^{(2)T} = \tilde{\boldsymbol{K}}^{(th)}. \tag{B.6}$$

If the matrix $\boldsymbol{K}_B$ is not singular but has very small eigenvalues, $\bar{\boldsymbol{L}}_{TS}^{(2)}$ will have large terms that depend strongly on these small eigenvalues. Considering further that they

probably result from the introduction of the matrix Δ_1 and Δ_2, not from an actual property of the structure, it is concluded that the values of $\bar{\boldsymbol{L}}_{TS}^{(2)}$ will be large and unphysical.

To remedy this situation, two options are proposed here. The first relies on splitingt the components of $\boldsymbol{F}^{(th)}$ and $\tilde{\boldsymbol{K}}^{(th)}$ consistently with the eigenvalues of the matrix $\boldsymbol{K}_B$. Specifically, assuming that permutations of rows and columns have been performed to transform this latter matrix into its form of Eq. (B.1), one has

$$\boldsymbol{K}_C = \begin{bmatrix} \boldsymbol{K}_{11} & \boldsymbol{K}_{12}+\Delta_1 & \boldsymbol{K}_{13} \\ \boldsymbol{K}_{12}^T+\Delta_1^T & \boldsymbol{K}_{22}+\Delta_2 & \boldsymbol{K}_{23} \\ \boldsymbol{K}_{13}^T & \boldsymbol{K}_{23}^T & \boldsymbol{K}^{(\boldsymbol{tt})} \end{bmatrix} = \boldsymbol{K}_C^{(1)} + \boldsymbol{K}_C^{(2)}. \tag{B.7}$$

In this equation,

$$\boldsymbol{K}_C^{(1)} = \begin{bmatrix} \boldsymbol{K}_{11} & \boldsymbol{K}_{12}+\Delta_1 & \boldsymbol{K}_{13} \\ \boldsymbol{K}_{12}^T+\Delta_1^T & \boldsymbol{K}_{22}+\Delta_2 & \boldsymbol{R} \\ \boldsymbol{K}_{13}^T & \boldsymbol{R}^T & \boldsymbol{K}^{(\boldsymbol{tt})} \end{bmatrix} \text{ and } \boldsymbol{K}_C^{(2)} = \begin{bmatrix} \boldsymbol{0} & \boldsymbol{0} & \boldsymbol{0} \\ \boldsymbol{0} & \boldsymbol{0} & \boldsymbol{K}_{23}-\boldsymbol{R} \\ \boldsymbol{0} & \boldsymbol{K}_{23}^T-\boldsymbol{R}^T & \boldsymbol{0} \end{bmatrix} \tag{B.8}$$

where $\boldsymbol{R}$ is a matrix such that the Cholesky decomposition of $\boldsymbol{K}_C^{(1)}$ is of the form

$$\bar{\boldsymbol{L}}_{\boldsymbol{K}}^{(1)} = \begin{pmatrix} \bar{\boldsymbol{L}}_{11} & \boldsymbol{0} & \boldsymbol{0} \\ \bar{\boldsymbol{L}}_{21} & \bar{\boldsymbol{L}}_{22} & \boldsymbol{0} \\ \bar{\boldsymbol{L}}_{31} & \boldsymbol{0} & \boldsymbol{I} \end{pmatrix} \tag{B.9}$$

in which the presence of the identity matrix in the 33 block results from the discussion of Appendix C. Performing the product of Eq. (B.3) leads to

$$\bar{\boldsymbol{L}}_{11}\bar{\boldsymbol{L}}_{11}^T = \boldsymbol{K}_{11};\quad \bar{\boldsymbol{L}}_{21}^T = \bar{\boldsymbol{L}}_{11}^{-1}\left[\boldsymbol{K}_{12}+\Delta_1\right];\quad \bar{\boldsymbol{L}}_{31}^T = \bar{\boldsymbol{L}}_{11}^{-1}\boldsymbol{K}_{13}\text{; and finally } \boldsymbol{R} = \bar{\boldsymbol{L}}_{21}\bar{\boldsymbol{L}}_{31}^T \tag{B.10}$$

which fully defines $\bar{\boldsymbol{L}}_{\boldsymbol{K}}^{(1)}$ and enables the generation of the structural only partition of random $\boldsymbol{K}_C$ matrices. The structural-thermal component of these matrices will be

obtained by summing, as for the mean model above, the contributions obtained using the $\bar{\boldsymbol{L}}_{\boldsymbol{K}}^{(1)}$ decomposition in Eq. (3.20) and those obtained with the $\bar{\boldsymbol{L}}_{\boldsymbol{K}}^{(2)}$ matrix

$$\bar{\boldsymbol{L}}_{\boldsymbol{K}}^{(2)} = \begin{pmatrix} \boldsymbol{I} & \boldsymbol{0} & \boldsymbol{0} \\ \boldsymbol{0} & \boldsymbol{I} & \boldsymbol{0} \\ \boldsymbol{0} & \boldsymbol{K}_{23}^{T} - \boldsymbol{R}^{T} & \boldsymbol{I} \end{pmatrix} \tag{B.11}$$

where the introduction of the identity matrix along the diagonal is consistent with the maximum entropy discussion of Appendix C.

A second option to address the near singularity of the matrix $\boldsymbol{K}_B$ is to recognize that the components of this matrix associated with the near zero eigenvalues do not introduce uncertainty in $\boldsymbol{K}_B$ within the nonparametric framework (see Wang et al 2018 for related discussion). Accordingly, it is sufficient to randomize solely the block $\boldsymbol{K}_{11}$ of this matrix. In this perspective, the randomization of the matrix $\boldsymbol{K}_C$ can be reduced to that of

$$\hat{\boldsymbol{K}}_C = \begin{bmatrix} \boldsymbol{K}_{11} & \boldsymbol{K}_{13} \\ \boldsymbol{K}_{13}^{T} & \boldsymbol{K}^{(\boldsymbol{tt})} \end{bmatrix}. \tag{B.12}$$

of which the Cholesky decomposition is taken as (see also section 3.3.3)

$$\bar{\boldsymbol{L}}_{\boldsymbol{K}}^{(1)} = \begin{pmatrix} \bar{\boldsymbol{L}}_{11} & \boldsymbol{0} \\ \bar{\boldsymbol{L}}_{31} & \boldsymbol{I} \end{pmatrix}. \tag{B.13}$$

The above approach is appropriate when the effects of the block $\bar{\boldsymbol{K}}_{23}$ on the mean response of the structure is small. Otherwise, this matrix must also be randomized as suggested in Eq. (B.11) leading to

$$\boldsymbol{K}_{23} = \left(\overline{\boldsymbol{K}}_{23} + \boldsymbol{H}_{T2}\right) \boldsymbol{H}_{S2} \boldsymbol{H}_{S2}{}^{T} \tag{B.14}$$

where $\boldsymbol{H}_{S2}$ is $q \times q$ and $\boldsymbol{H}_{T2}$ is $p \times q$ when $\boldsymbol{K}_{23}$ is $p \times q$,

APPENDIX C

MAXIMUM ENTROPY UNCERTAINTY MODLEING OF A MATRIX WITH UNKNOWN LOWER RIGHT CORNER

This appendix focuses on the determination of the deterministic matrix $\bar{\boldsymbol{L}}_{TT}$ yielding a maximum entropy of the random matrices $\boldsymbol{K}_C$ as defined by

$$S_{\boldsymbol{K}} = -\int_{\Omega} p_{\boldsymbol{K}_C}(\boldsymbol{k}) \ln\, p_{\boldsymbol{K}_C}(\boldsymbol{k})\, d\boldsymbol{k}\,. \tag{C.1}$$

To this end, rewrite first Eq. (3.20) as

$$\boldsymbol{K}_C = \bar{\boldsymbol{L}}_{\boldsymbol{K}}\, \boldsymbol{G}\, \bar{\boldsymbol{L}}_{\boldsymbol{K}}^T \quad \text{where} \quad \boldsymbol{G} = \boldsymbol{H}_{\boldsymbol{K}}\, \boldsymbol{H}_{\boldsymbol{K}}^T \tag{C.2),(C.3}$$

and note that Eq. (C.2) can be viewed as a linear transformation of the random elements of the matrix $\boldsymbol{G}$ into the random components of $\boldsymbol{K}_C$. Accordingly, the joint probability density functions of the elements of these two matrices are related by the equation

$$p_{\boldsymbol{K}_C}(\boldsymbol{k}) = p_{\boldsymbol{G}}(\boldsymbol{g}) / \left|\det(\boldsymbol{J})\right| \quad \text{and} \quad d\boldsymbol{k} = \left|\det(\boldsymbol{J})\right| d\boldsymbol{g} \tag{C.4),(C.5}$$

where $\boldsymbol{J}$ is the Jacobian of the transformation. To evaluate this matrix from Eq. (C.2), it is convenient to rewrite it first stacking the columns of the matrix $\boldsymbol{K}_C$ below each other and proceeding similarly with the matrix $\boldsymbol{G}$ consistently with the **vec** operation. Then, one obtains

$$\boldsymbol{vec}(\boldsymbol{K}_C) = \boldsymbol{vec}\left(\bar{\boldsymbol{L}}_{\boldsymbol{K}}\, \boldsymbol{G}\, \bar{\boldsymbol{L}}_{\boldsymbol{K}}^T\right) = \left(\bar{\boldsymbol{L}}_{\boldsymbol{K}} \otimes \bar{\boldsymbol{L}}_{\boldsymbol{K}}\right) \boldsymbol{vec}(\boldsymbol{G}) \tag{C.6}$$

where $\otimes$ denotes the Kronecker product owing to the property

$$\boldsymbol{vec}(\boldsymbol{A}\,\boldsymbol{B}\,\boldsymbol{C}) = \left(\boldsymbol{C}^T \otimes \boldsymbol{A}\right) \boldsymbol{vec}(\boldsymbol{B}) \tag{C.7}$$

for any matrices $\boldsymbol{A}$, $\boldsymbol{B}$, and $\boldsymbol{C}$ with consistent dimensions.

From Eq. (C.6), it is found that

$$\boldsymbol{J} = \bar{\boldsymbol{L}}_{\boldsymbol{K}} \otimes \bar{\boldsymbol{L}}_{\boldsymbol{K}} \quad \text{so that} \quad \det(\boldsymbol{J}) = \det\left(\bar{\boldsymbol{L}}_{\boldsymbol{K}}\right)^2 = \prod_i \bar{L}_{K,ii}^2 \qquad \text{(C.8), (C.9)}$$

where the last equality holds owing to the triangular structure of $\bar{\boldsymbol{L}}_{\boldsymbol{K}}$.

Next, combining Eq. (C.1), (C.4), and (C.5), it is found that

$$S_{\boldsymbol{K}} = -\int_{\Omega_{\boldsymbol{G}}} p_{\boldsymbol{G}}(\boldsymbol{g}) \ln\left[p_{\boldsymbol{G}}(\boldsymbol{g}) / \left|\det(\boldsymbol{J})\right|\right] d\boldsymbol{g} \qquad \text{(C.10)}$$

where $\Omega_{\boldsymbol{G}}$ is the appropriate domain of variations of the matrices $\boldsymbol{g}$. Since $\boldsymbol{J}$ is a constant matrix (independent of $\boldsymbol{g}$), Eq. (C.10) reduces to

$$S_{\boldsymbol{K}} = \ln\left[\left|\det(\boldsymbol{J})\right|\right] \int_{\Omega_{\boldsymbol{G}}} p_{\boldsymbol{G}}(\boldsymbol{g})\, d\boldsymbol{g} - \int_{\Omega_{\boldsymbol{G}}} p_{\boldsymbol{G}}(\boldsymbol{g}) \ln\left[p_{\boldsymbol{G}}(\boldsymbol{g})\right] d\boldsymbol{g} = \ln\left[\left|\det(\boldsymbol{J})\right|\right] + S_{\boldsymbol{G}}$$

(C.11)

where $S_{\boldsymbol{G}}$ is the entropy of the matrices $\boldsymbol{G}$ and is independent of $\bar{\boldsymbol{L}}_{\boldsymbol{K}}$. Recognizing that

$$\det(\boldsymbol{J}) = \left[\det\left(\bar{\boldsymbol{L}}_{\boldsymbol{K}}\right)\right]^2 = \left[\det\left(\bar{\boldsymbol{L}}_{SS}^{(1)}\right)\det\left(\bar{\boldsymbol{L}}_{SS}^{(3)}\right)\det\left(\bar{\boldsymbol{L}}_{TT}\right)\right]^2 \qquad \text{(C.12)}$$

it is concluded that maximizing the entropy $S_{\boldsymbol{K}}$ is achieved when the determinant of $\bar{\boldsymbol{L}}_{TT}$ is as large as possible, unless some constraint is added to the problem.

In this regard, consider the effect of $\bar{\boldsymbol{L}}_{TT}$ on the simulated reduced order model coefficients. This matrix affects only the random coefficients $K_{ijl}^{(th)}$ and $F_{il}^{(th)}$ through the products $\bar{\boldsymbol{L}}_{TT}\, \boldsymbol{H}_{TS}^{(1)}$ and $\bar{\boldsymbol{L}}_{TT}\, \boldsymbol{H}_{TS}^{(2)}$, i.e., $\bar{\boldsymbol{L}}_{TT}$ provides a scaling of the effects of $\boldsymbol{H}_T$ which are all proportional to the standard deviation σ. So, increasing uniformly $\bar{\boldsymbol{L}}_{TT}$

is equivalent to increasing σ. Accordingly, it is not possible to specify or identify both a uniform scaling of $\bar{\boldsymbol{L}}_{TT}$ and the standard deviation σ. The approach chosen here is then to constraint the uniform scaling so that σ can be a true parameter of the model. Thus, to the maximization of the entropy is now added the scaling constraint

$$\left\|\bar{\boldsymbol{L}}_{TT}\right\|_F = \sqrt{\mu} \tag{C.13}$$

The lower triangular matrix $\bar{\boldsymbol{L}}_{TT}$ sought leads to a maximum value of its determinant while satisfying Eq. (C.13). Proceeding with a Lagrange multiplier, it is desired to find the elements $\bar{L}_{ij}$, $i \geq j$, of $\bar{\boldsymbol{L}}_{TT}$ such that $\bar{L}_{ii} > 0$ and

$$\Upsilon = \prod_{i=1}^{\mu} \bar{L}_{ii} + \gamma \left[\sum_{i=1}^{\mu} \sum_{j \leq i} \bar{L}_{ij}^2 - \mu \right] \tag{C.14}$$

is maximum where γ is the Lagrange multiplier. Differentiating Eq. (C.14) with respect to $\bar{L}_{ij}$ $i \neq j$ demonstrates first that these components must all be zero and thus the matrix $\bar{\boldsymbol{L}}_{TT}$ is diagonal. Then, differentiating Eq. (C.14) with respect to $\bar{L}_{jj}$ yields

$$\prod_{i=1, i \neq j}^{\mu} \bar{L}_{ii} + 2\gamma \bar{L}_{jj} = 0 \quad \text{or} \quad \prod_{i=1}^{\mu} \bar{L}_{ii} + 2\gamma \bar{L}_{jj}^2 = 0 \tag{C.15),(C.16}$$

where Eq. (C.16) results from (C.15) by multiplication by $\bar{L}_{jj} \neq 0$. Since the product term in Eq. (C.16) is independent of $\bar{L}_{jj}$, it is concluded that $\bar{L}_{jj}^2$ is independent of the index *j* and thus, from Eq. (C.13), $\bar{L}_{jj}^2 = 1$. Since the diagonal terms $\bar{L}_{jj}$ must be

positive, one obtains $\bar{L}_{jj} = 1$ for all j and thus the lower triangular matrix $\bar{\boldsymbol{L}}_{TT}$ sought equals the identity matrix.

APPENDIX D

PERMISSION TO USE PUBLISHED OR PUBLISHABLE WORK

Chapter 2 contains a published work by Pengchao Song and Marc P. Mignolet in 2018, “Reduced order model-based uncertainty modeling of structures with localized response”, *Probabilistic Engineering Mechanics* Vol. 51:42-55.

Chapter 3 contains a publishable work by Pengchao Song, X.Q. Wang, Andrew K. Matney, Raghavendra Murthy, and Marc P. Mignolet, “Nonlinear geometric thermoelastic response of structures with uncertain thermal and structural properties”, *AIAA Journal*.

Chapter 4 contains a publishable work by Pengchao Song and Marc P. Mignolet, “Maximum entropy-based uncertainty modeling at the elemental level in linear structural and thermal problems”, *Computational Mechanics.*

All the co-authors have granted their permissions to use their works in this document.